

Entanglement Barrier and its Symmetry Resolution: Theory and Experimental Observation

Aniket Rath^{1,†}, Vittorio Vitale^{2,3,*†}, Sara Murciano^{2,4,†}, Matteo Votto¹, Jérôme Dubail⁵,
Richard Kueng⁶, Cyril Branciard⁷, Pasquale Calabrese^{2,3,4} and Benoît Vermersch^{1,8,9}

¹ *Université Grenoble Alpes, CNRS, Laboratoire de Physique et Modélisation des Milieux Condensés (LPMMC), Grenoble 38000, France*

² *Scuola Internazionale Superiore di Studi Avanzati (SISSA), via Bonomea 265, Trieste 34136, Italy*

³ *International Centre for Theoretical Physics (ICTP), Strada Costiera 11, Trieste 34151, Italy*

⁴ *National Institute for Nuclear Physics (INFN), via Bonomea 265, Trieste 34136, Italy*

⁵ *Université de Lorraine, CNRS, Laboratoire de Physique et Chimie Théoriques (LPCT), Nancy F-54000, France*

⁶ *Institute for Integrated Circuits, Johannes Kepler University Linz, Altenbergerstrasse 69, Linz 4040, Republic of Austria*

⁷ *Université Grenoble Alpes, CNRS, Institute of Engineering Université Grenoble Alpes, Institut Néel, Grenoble 38000, France*

⁸ *Institute for Theoretical Physics, University of Innsbruck, Innsbruck, Republic of Austria*

⁹ *Institute for Quantum Optics and Quantum Information of the Austrian Academy of Sciences, Innsbruck A-6020, Republic of Austria*



(Received 19 September 2022; accepted 30 January 2023; published 21 February 2023)

The operator entanglement (OE) is a key quantifier of the complexity of a reduced density matrix. In out-of-equilibrium situations, e.g., after a quantum quench of a product state, it is expected to exhibit an *entanglement barrier*. The OE of a reduced density matrix initially grows linearly as entanglement builds up between the local degrees of freedom; it then reaches a maximum and ultimately decays to a small finite value as the reduced density matrix converges to a simple stationary state through standard thermalization mechanisms. Here, by performing a new data analysis of the published experimental results of Brydges *et al.* [Science **364**, 260 (2019)], we obtain the first experimental estimation of the OE of a subsystem reduced density matrix in a quantum many-body system. We employ the randomized-measurements toolbox and we introduce and develop a new efficient method to postprocess experimental data in order to extract higher-order density-matrix functionals and access the OE. The OE thus obtained displays the expected *barrier* as long as the experimental system is large enough. For smaller systems, we observe a barrier with a double-peak structure, the origin of which can be interpreted in terms of pairs of quasiparticles being reflected at the boundary of the qubit chain. As $U(1)$ symmetry plays a key role in our analysis, we introduce the notion of symmetry-resolved operator entanglement (SROE), in addition to the total OE. To gain further insights into the SROE, we provide a thorough theoretical analysis of this new quantity in chains of noninteracting fermions, which, in spite of their simplicity, capture most of the main features of OE and SROE. In particular, we uncover three main physical effects: the presence of a barrier in any charge sector, a time delay for the onset of the growth of SROE, and an effective equipartition between charge sectors.

DOI: [10.1103/PRXQuantum.4.010318](https://doi.org/10.1103/PRXQuantum.4.010318)

I. INTRODUCTION

The investigation of the nonequilibrium dynamics of isolated many-body quantum systems is a major challenge

*vvitale@sissa.it

†These authors contributed equally.

Published by the American Physical Society under the terms of the [Creative Commons Attribution 4.0 International](https://creativecommons.org/licenses/by/4.0/) license. Further distribution of this work must maintain attribution to the author(s) and the published article's title, journal citation, and DOI.

of modern physics. Owing to the highly tunable modern experimental settings for analog simulations [1–4], it has become possible to engineer the Hamiltonian dynamics of isolated quantum systems, ranging from integrable to chaotic systems, and measure nontrivial physical properties such as the entanglement growth following a quantum quench [5–9] and out-of-time ordered correlators [10–14]. Unfortunately, the absence of numerical algorithms to effectively simulate these systems on a classical computer for large times is the main obstacle toward the complete understanding of quantum relaxation and thermalization. In this respect, the most effective and

versatile algorithms are surely those based on matrix-product-state (MPS) and tensor-network methods [15–19]. However, the linear growth of the entanglement entropy [20,21] requires an exponential complexity (in bond dimension) of the MPS approximating the physical state, which severely limits the largest simulable times [22].

Typically, these systems relax to statistical ensembles with little or no entanglement. How is this compatible with the growth in complexity of the MPS approximation? The solution of such a conundrum is simple: relaxation happens locally [23–25]; hence it is enough to focus solely on the reduced density matrix ρ of a subsystem S , rather than on the entire pure state containing physically irrelevant correlations. Indeed, rather than an MPS, the subsystem density matrix is approximated by a matrix product operator (MPO) with small bond dimension D [26–32]. What, then, is the quantity that correctly assesses the validity of this approximation? It is the *operator entanglement* (OE) of the reduced density matrix, which is the main subject of this paper.

To introduce this quantity, it is useful to note that every bipartite density matrix ρ_{AB} can be decomposed as follows:

$$\frac{\rho_{AB}}{\sqrt{\text{Tr}(\rho_{AB}^2)}} = \sum_i \lambda_i O_{A,i} \otimes O_{B,i}, \quad (1)$$

where all expansion coefficients λ_i are real and positive and the associated operators $O_{A,i}$ and $O_{B,i}$ are orthonormal with respect to the Hilbert-Schmidt inner product ($\text{Tr}(O_{A,i}^\dagger O_{A,j}) = \text{Tr}(O_{B,i}^\dagger O_{B,j}) = \delta_{ij}$, where δ_{ij} is the Kronecker delta) (see, e.g., Ref. [33]). Such a decomposition is called an *operator Schmidt decomposition* of ρ_{AB} and has the property that the set of *Schmidt coefficients* λ_i is unique (although the whole decomposition is not). The number of such nonzero coefficients is called the *operator Schmidt rank* of ρ_{AB} . Our choice of normalization on the left-hand side of Eq. (1) ensures that the Schmidt coefficients thus introduced obey $\sum_i \lambda_i^2 = 1$, i.e., the set $\{\lambda_i^2\}$ forms a probability distribution of (squared) Schmidt values. In a MPO algorithm, the density matrix ρ_{AB} is “compressed” by truncating the full sum to only the D largest contributions, for some reasonably low value of D . Typically, the approximation is accurate provided that the distribution $\{\lambda_i^2\}$ of squared Schmidt values in Eq. (1) has small Shannon entropy, i.e., $S(\rho_{AB}) = S(\{\lambda_i^2\}) = -\sum_i \lambda_i^2 \log(\lambda_i^2)$ is small enough. This quantity is called the *operator entanglement* [26,27,34,35] of the bipartite density matrix ρ_{AB} . In this paper we focus on the OE of a reduced density matrix. Its main physical feature is the presence of an *entanglement barrier* [29,36,37]: after a quantum quench from a low-entangled state, the OE of a subsystem density matrix initially grows linearly and then decays at longer times, thus displaying a barrier-shaped curve. The initial linear growth is a consequence of the generic linear

growth of the (state) entanglement entropy after a quench [20,21], while the decay at later times reflects the convergence of the reduced density matrix toward a simple stationary state [29], through the mechanism of thermalization [23,24,38–43] (or relaxation to a generalized Gibbs ensemble [44–47]).

The emergence of the entanglement barrier for the OE of a reduced density matrix in ergodic dynamics can be linked straightforwardly to the distribution of squared Schmidt values $\{\lambda_i^2\}$ from Eq. (1). At early times, the evolution starts from a pure product state, when only a single Schmidt value is different from zero. The building up of entanglement is reflected in the increasing number of nonzero Schmidt coefficients λ_i . For long times, the system eventually locally approaches a Gibbs or generalized Gibbs ensemble, which obeys the operator area law [29], i.e., it is constant in the subsystem size, and again only few Schmidt values give a sizable contribution to the OE. For example, in the infinite-temperature limit, since the density matrix is proportional to the identity, $\rho \propto \mathbb{I} = (\mathbb{I}_A \otimes \mathbb{I}_B)$, only a single Schmidt value is different from zero and the OE vanishes.

Inspired by the relevance of the *entanglement barrier*, our goal is to observe it in an experimental quantum many-body system, using the randomized-measurement data of the trapped-ion experiment of Ref. [7]. The randomized-measurement toolbox [48] has enabled state-agnostic measurement of the properties of the underlying quantum state, such as the purity and the Rényi entanglement entropies [7,9,48–50], negativities [51–53], and state fidelities [49,54,55]. In contrast to tomography methods based on assumptions on the quantum state [45,56–59], randomized measurements remain “state agnostic,” while having a lower measurement cost compared to full quantum state tomography [56,60–63]. One particularly fruitful development is the formalism of classical shadows [49,64], which provides estimations of additional nonlinear functionals of the density matrix, such as the OE [65]. However, measuring OE using the current randomized-measurement toolbox requires a prohibitively expensive postprocessing method. To overcome this limitation and observe OE for a reasonable system size, in this work we introduce the *batch-shadows estimator*. This new estimator, which should be of independent interest for the randomized-measurement toolbox as a whole, provides a fast postprocessing technique for estimating multicopy expectation values as functions of the density matrix. Importantly, this method offers, up to factors of order one in the experimentally relevant scenario, the same performance guarantees as classical shadows in terms of the required number of measurements to overcome statistical errors. This enables us to estimate the OE and, in turn, witness the entanglement barrier. Here, we would like to emphasize that we do not perform a new experiment to achieve this observation but that we realize, instead, a new postprocessing of the

data of Ref. [7], in the spirit—measure first, ask questions later—of the randomized-measurements toolbox [48].

As a second important result, the experimental data of Ref. [7] provide us with an opportunity to study how the OE content is structured due to the presence of a symmetry which, here, is a $U(1)$ symmetry associated with the number of spin excitations. In the case of pure-state entanglement, the fruitful notion of symmetry-resolved entropies [66–68] has been introduced recently, computed theoretically [69–78], and experimentally observed [52,53,79]. Here, we generalize this to the case of OE. Based on suitable supercharge operators (throughout this paper, we refer to the operators in the space of operators as superoperators and to the corresponding charges as supercharges), we introduce a notion of *symmetry-resolved operator entanglement (SROE)*, for which we also provide tractable estimation protocols. Using SROE, we can theoretically study and observe, from the data of Ref. [7], a symmetry-resolved entanglement barrier. This is relevant for understanding thermalization in $U(1)$ symmetric nonequilibrium quantum systems and also for numerical simulations, because symmetries can be incorporated in MPO algorithms.

II. SUMMARY OF RESULTS

Here, we provide a bird’s eye view of the results in this paper. The remainder of the paper is organized as follows. In Sec. III, we formally introduce the operator entanglement (OE) and its symmetry resolution (SROE). In Sec. IV, we demonstrate and describe the details of the randomized-measurement protocol used to measure the OE and SROE of the experiment performed in Ref. [7]. In Sec. V, we study analytically the SROE of the reduced density matrix of a subsystem of critical free-fermion chains after a quantum quench. Finally, we draw our conclusions in Sec. VI. We include five appendixes with more details about the analytical and numerical computations. In Appendix A, we provide entanglement conditions for mixed states using quantities introduced for the OE. Appendix B follows up by detailing the proof of the symmetry resolution of the operator Schmidt decomposition from Eq. (1). In Appendix C, we develop an analytical framework for the statistical-error analysis of general batch-shadows estimators and we then describe the setup of the experiment that we consider in this paper in Appendix D. Further details on the treatment of experimental data using batch shadows are provided in Appendix E.

Therefore, let us start by providing a short summary of the results in this paper—the main points are also illustrated in Fig. 1:

- (1) For the first time, we provide a general definition of the symmetry resolution of the OE in the presence

of a global $U(1)$ symmetry. This is done formally in Sec. III and Appendix B.

- (2) We introduce a new method of analysis method that allows us to measure the OE and SROE of the density matrix of a subsystem in a many-body quantum system from the published experimental data of Brydges *et al.* [7], presenting a $U(1)$ conserved charge. Namely, we employ the *randomized-measurement toolbox* [48] and propose a new efficient method to postprocess experimental data in order to extract arbitrary higher-order density-matrix functionals of the form $\text{Tr}(O^{(n)}\rho^{\otimes n})$, expressed in terms of an n -copy operator $O^{(n)}$. A schematic of this procedure is shown in Fig. 1(a) and its details are elaborated in Sec. IV, as well as Appendixes C–E. This tool is employed to extract the experimental results presented in Figs. 1(b) and 1(c). Here, we show the measured OE and SROE, as in Eq. (4), which are supported by tensor-network simulations modeling the full experiment, i.e., the open dynamics of a long-range XY model starting from the Néel state, with conserved magnetization along the z axis. Our main observations of Sec. IV are summarized here:

- (a) We witness experimentally the entanglement barrier of the OE and the SROE in the charge sector $q = 0$ [Fig. 1(b)], for a bipartite subsystem $A \cup B$ comprised of 4 out of $N = 20$ ions. These barriers present bump structures due to finite-size effects. For a smaller system with $N = 10$, we observe a second growth of OE after the first peak, as shown in Fig. 1(c). This can be interpreted as an effect of quasiparticles reflected at the boundary of the chain, as described in Sec. IV D.
- (b) We observe a qualitative agreement of the SROE with the numerical results for charge sectors $q = \pm 1$ at early times. The sizable deviation between theory and experiment for $N = 20$ [Fig. 1(b)] is caused by the small populations in the corresponding charge sectors and by the low measurement statistics available from the experiment.
- (3) To gain insights into SROE and its own entanglement barrier, we provide a thorough theoretical analysis in chains of noninteracting fermions, which despite their simplicity, capture the main physical features of the OE and SROE. This is already visible for small system sizes N , by comparing Figs. 1(b) and 1(c) with Figs. 1(d) and 1(e), respectively. Moreover, for these free models, we obtain the general formula in Eq. (46), which governs the evolution of the SROE. This formula allows

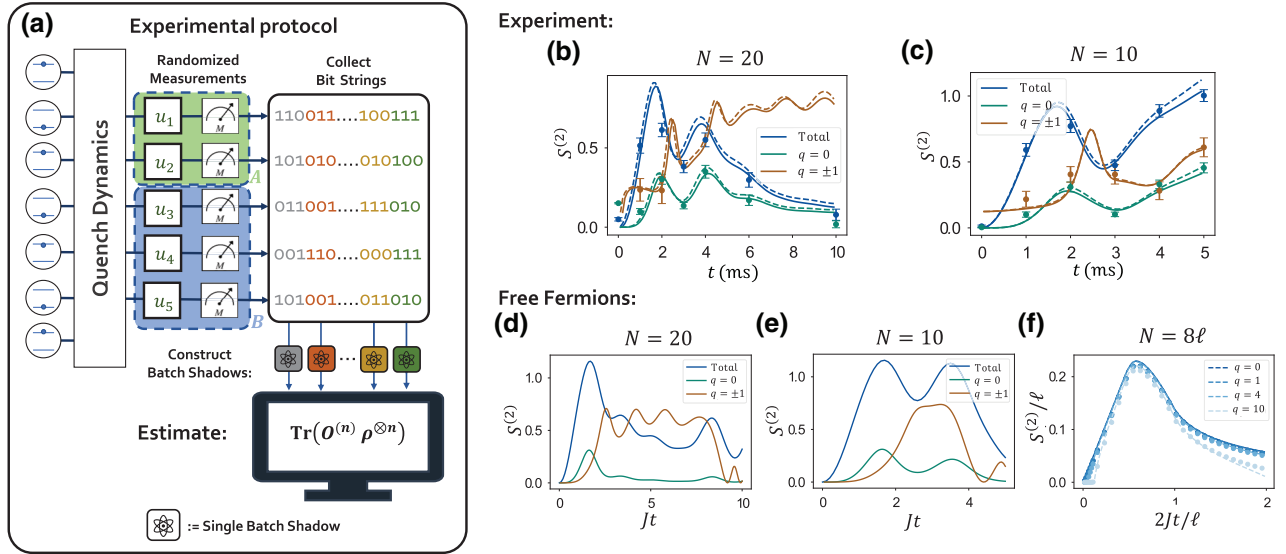


FIG. 1. An overview of the results. (a) A schematic of the method to postprocess the experimental data. After the quench dynamics, randomized measurements are performed. The collected bit strings are grouped to construct *batch shadows* that provide estimates of OE and SROE. (b),(c) Experimental results for the Rényi 2-OE [Eq. (4)] and its symmetry resolution [Eq. (14)] of a reduced density matrix formed from a partition of (b) 4 ions out of 20 and (c) 10 ions from the data of Ref. [7] after the global quantum quench. The points correspond to the experimental data, while the curves are numerical results obtained via tensor-network algorithms with (solid) or without (dashed) dissipation considered. The entanglement barrier is visible for the total OE and the symmetry sector $q = 0$ with $N = 20$. (d)–(f) Symmetry resolution of the OE of the reduced density matrix after a global quantum quench in a free-fermion chain under unitary evolution. (d),(e) Symmetry resolution of the OE of the reduced density matrix after a global quantum quench, for a 4 out of 20 (out of 10) sites chain. Comparing with the experimental results in (b) and (c), respectively, we can spot several qualitative features of OE even though the model is short ranged and there is no dissipation. (f) Numerical data (circles) with subsystem length $\ell = 256$, $\ell_A = \ell - \ell_B = 120$ compared with the quasiparticle prediction of Eq. (46) (continuous lines). This plot shows the three main features of SROE in the thermodynamic limit, i.e., the barrier in each sector q , the time delay, and the equipartition for small q . In the free-fermion plots, J is the hopping term and we consider, for the sake of simplicity, $\hbar = 1$ and lattice constant $a = 1$.

us to uncover three main physical effects, which we expect to appear more generically in chains of qubits, beyond the simple noninteracting fermion ones:

- The appearance of a barrier for SROE in *any* charge sector, which resembles the behavior of the total OE
- A time delay for the onset of the SROE that grows linearly with the charge sector of the subsystem
- The effective equipartition in the scaling limit of large time and subsystem size for small charges [see Eq. (47)], where by equipartition we mean that the SROE is equally distributed among the different symmetry sectors

These effects are visible in Fig. 1(f). There, we plot the OE and SROE of the reduced density matrix, for a bipartition $A \cup B$, where the numerical results are obtained for a quench in the tight-binding model from the Néel state, while the solid lines correspond to Eq. (46).

III. OPERATOR ENTANGLEMENT AND SYMMETRY RESOLUTION

In this section, we formally introduce the OE definition, emphasize its connection to mixed-state entanglement, and also define symmetry-resolved OE in the presence of an additive global conserved charge.

A. Definition of operator entanglement

The OE can be defined for arbitrary operators acting on a bipartite quantum system $A \cup B$. However, for the sake of simplicity and clarity, we present and discuss it here solely for bipartite density operators ρ_{AB} .

Recall from Eq. (1) that every ρ_{AB} admits an *operator Schmidt decomposition*

$$\frac{\rho_{AB}}{\sqrt{\text{Tr}(\rho_{AB}^2)}} = \sum_{i=1}^R \lambda_i O_{A,i} \otimes O_{B,i}, \quad (2)$$

where $R = \text{srnk}(\rho_{AB})$ is the (operator) Schmidt rank, $\lambda_1, \dots, \lambda_R > 0$ are the Schmidt coefficients, and $O_{A,i}$, as

well as $O_{B,i}$, denote orthonormal operator families on subsystems A and B , respectively. In general, for a Hermitian density operator ρ_{AB} , these operators $O_{A,j}$ and $O_{B,j}$ can be taken to be Hermitian themselves [33], although this is not necessarily imposed.

In a similar way to the more widely known pure-state case [80], the Schmidt values capture some form of entanglement that is present in the system. In fact, there is an intimate connection between the two. The operator Schmidt decomposition in Eq. (2) arises from first vectorizing the renormalized operator $\varrho_{AB} = \rho_{AB}/\sqrt{\text{Tr}(\rho_{AB}^2)}$ (using the Choi-Jamiołkowski isomorphism [81,82]),

$$\varrho_{AB} = \sum_{ij} (\varrho_{AB})_{ij} |i\rangle \langle j| \mapsto |\varrho_{AB}\rangle = \sum_{ij} (\varrho_{AB})_{ij} |i\rangle |j\rangle, \quad (3)$$

applying the ordinary Schmidt decomposition to the pure ket vector $|\varrho_{AB}\rangle$, and eventually reverting the vectorization to get back to the space of operators. This connection justifies the quantification of OE in terms of the distribution of squared Schmidt values. More precisely, recalling that with our choice of normalization in Eq. (2) the squared Schmidt coefficients $\{\lambda_i^2\}$ define a normalized probability distribution, we define the Rényi α -OE,

$$S^{(\alpha)}(\rho_{AB}) := \frac{1}{1-\alpha} \log \sum_{i=1}^R (\lambda_i^2)^\alpha \quad \text{for } \alpha \neq 1, \quad (4)$$

which in the limit $\alpha \rightarrow 1$ produces the (Shannon) OE,

$$S(\rho_{AB}) := \sum_{i=1}^R -\lambda_i^2 \log \lambda_i^2. \quad (5)$$

It is clear that a state ρ_{AB} has zero OE, $S(\rho_{AB}) = 0$, if and only if it can be written as a product state of the form $\rho_{AB} = \rho_A \otimes \rho_B$. When this is not the case, we call the state “operator entangled.” It is worthwhile emphasizing that an operator-entangled (i.e., nonproduct) state may still be nonentangled according to the standard terminology for mixed-state entanglement [33].

B. Operator entanglement and entanglement criteria

As already pointed out above, there is an intimate connection between OE and the more familiar concept of state entanglement, where one is interested in showing that ρ_{AB} cannot be written as a convex mixture of product states $\rho_{AB} = \sum_k \alpha_k \rho_A^{(k)} \otimes \rho_B^{(k)}$ and $\alpha_k \geq 0$, and $\rho_A^{(k)}$ and $\rho_B^{(k)}$ are subsystem density matrices (i.e., positive semidefinite and unit trace) [33]. Let λ_i be the coefficients of the operator Schmidt decomposition of ρ_{AB} , as introduced above. The realignment or computable cross-norm criterion (CCNR)

[83–85] states that every separable (i.e., nonentangled) state produces operator Schmidt coefficients λ_i that obey

$$\sum_i \lambda_i \leq 1/\sqrt{\text{Tr}[\rho_{AB}^2]}. \quad (6)$$

Conversely, entanglement (across the bipartition A versus B) must be present if this relation is violated. The connection between the CCNR criterion and OE has been recently developed in Ref. [65] where optimal experimentally detectable entanglement criteria have been provided. Here, we introduce a slightly weaker but much more compact entanglement condition. Using the CCNR criterion, we can prove that separability implies that the Rényi 2-OE (Eq. (4) for $\alpha = 2$) and the Rényi 2-entropy $R^{(2)} := -\log \text{Tr}(\rho_{AB}^2)$ must obey

$$S^{(2)}(\rho_{AB}) \leq -\log(\text{Tr}[\rho_{AB}^2]) = R^{(2)}(\rho_{AB}). \quad (7)$$

Conversely, if $S^{(2)}(\rho_{AB}) > R^{(2)}(\rho_{AB})$, i.e., if ρ_{AB} is more “operator mixed” than “state mixed” with respect to Rényi 2-entropies, ρ_{AB} is necessarily entangled. For details, see Appendix A, where we also compare the detection power of this method with other entanglement conditions and present experimental results.

C. Symmetry-resolved operator entanglement

In the presence of a global symmetry, the OE of the operator ρ_{AB} can be split into different charge sectors, similarly to that of the state entanglement [67,68].

This happens in particular for a global $U(1)$ symmetry, where the $U(1)$ charge operator acting on $A \cup B$ is a sum of the two charge operators acting on subsystems A and B , i.e., $Q_{AB} = Q_A + Q_B$. From now on, by $Q_A + Q_B$ we mean $Q_A \otimes \mathbb{I}_B + \mathbb{I}_A \otimes Q_B$. If the density matrix ρ_{AB} commutes with Q_{AB} , that is

$$[Q_A + Q_B, \rho_{AB}] = 0, \quad (8)$$

then it becomes possible to reorganize the terms in the Schmidt decomposition given in Eq. (2) according to their “charge” q :

$$\frac{\rho_{AB}}{\sqrt{\text{Tr}[\rho_{AB}^2]}} = \sum_q \sum_j \lambda_j^{(q)} O_{A,j}^{(q)} \otimes O_{B,j}^{(-q)}, \quad (9)$$

where

$$[Q_A, O_{A,j}^{(q)}] = q O_{A,j}^{(q)}, \quad [Q_B, O_{B,j}^{(-q)}] = -q O_{B,j}^{(-q)} \quad (10)$$

such that $[Q_A + Q_B, O_{A,j}^{(q)} \otimes O_{B,j}^{(-q)}] = 0$. Equations (9) and (10) are proven in Appendix B. In particular, we show that

the ‘‘charge’’ q that appears in these equations can be introduced, through the vectorization technique introduced in Eq. (3), based on the notion of a charge ‘‘superoperator’’:

$$\mathcal{Q}_{AB} = \mathcal{Q}_{AB} \otimes \mathbb{1} - \mathbb{1} \otimes \mathcal{Q}_{AB}^T. \quad (11)$$

Namely, the values q are the eigenvalues of $\mathcal{Q}_A = \mathcal{Q}_A \otimes \mathbb{1} - \mathbb{1} \otimes \mathcal{Q}_A^T$, i.e., the restriction of \mathcal{Q}_{AB} to the subsystem A [67] [or, equivalently, the eigenvalues of the commutator $[\mathcal{Q}_A, \cdot]$, as in Eq. (10)]. As we prove in Appendix B 4, using language analogous to the symmetry resolution for a state [67], the super-reduced density matrix $\text{Tr}_{B \otimes B}(|\rho_{AB}\rangle\langle\rho_{AB}|)$ admits a block decomposition in the eigenspaces corresponding to these charges q , which then leads to Eqs. (9) and (10). We also provide an illustrative example of Eq. (9) in Appendix B 5, starting from a three-qubit system.

Similarly to the non-symmetry-resolved case of Eq. (2), the newly constructed operator families $O_{A_j}^{(q)}$ and $O_{B_j}^{(q)}$ in Eq. (9) are orthonormal with respect to the Hilbert-Schmidt inner product, i.e., $\text{Tr}[(O_{A_{j_1}}^{(q_1)})^\dagger O_{A_{j_2}}^{(q_2)}] = \text{Tr}[(O_{B_{j_1}}^{(q_1)})^\dagger O_{B_{j_2}}^{(q_2)}] = \delta_{q_1, q_2} \delta_{j_1, j_2}$. In contrast to Eq. (2), however, in the symmetry-resolved Schmidt decomposition given in Eq. (9), these operators cannot always be taken to be Hermitian.

By uniqueness of the Schmidt coefficients, the set of all (nonzero) values $\{\lambda_j^{(q)}\}$ altogether must be the same as the set of values $\{\lambda_i\}$ from Eq. (2). We can now define the total weight of the terms at fixed q to be

$$p(q) := \sum_j (\lambda_j^{(q)})^2. \quad (12)$$

These weights satisfy $\sum_q p(q) = 1$ and give a probability distribution over the different charge sectors. In terms of that probability distribution, the (Shannon) OE from Eq. (5) becomes

$$S(\rho_{AB}) = \sum_q p(q) S_q(\rho_{AB}) + \sum_q -p(q) \log p(q), \quad (13)$$

where the *symmetry-resolved operator entanglement* (SROE) of ρ_{AB} in the charge sector q is

$$S_q(\rho_{AB}) := - \sum_j \left(\frac{(\lambda_j^{(q)})^2}{p(q)} \right) \log \left(\frac{(\lambda_j^{(q)})^2}{p(q)} \right). \quad (14)$$

Similarly, for $\alpha \neq 1$, we define the *Rényi α -SROE* to be

$$S_q^{(\alpha)}(\rho_{AB}) := \frac{1}{1-\alpha} \log \left(\sum_j \left(\frac{(\lambda_j^{(q)})^2}{p(q)} \right)^\alpha \right). \quad (15)$$

Note, however, that a formula analogous to Eq. (13) for a Rényi index $\alpha \neq 1$, in terms of $p(q)$, cannot be written.

Here, let us explain the meaning of Eq. (13). In an extended system in which the number of particles is conserved, there are two sources of entanglement: number entanglement (related to the particle-number fluctuations between the parts of the system) and configurational entanglement (correlations due to the different arrangements of the particles in the system), which in Eq. (13) are the two terms on the right-hand side. This decomposition of OE helps us to understand the OE of the density matrix of one-dimensional many-body models undergoing dissipative evolution [32], in the same way that standard state-entanglement decomposition is often used to explain the nonequilibrium dynamics of disordered systems and localization phenomena [11].

Another important remark is that in this paper, we focus on a density matrix on a bipartite subsystem $A \cup B$ that results from tracing out an additional system C . Let us observe that ρ_{AB} commutes with \mathcal{Q}_{AB} as soon as the full system $A \cup B \cup C$ is in a pure state, which is also an eigenstate of the total $U(1)$ charge operator $\mathcal{Q}_A + \mathcal{Q}_B + \mathcal{Q}_C$. Then, tracing out the degrees of freedom in C automatically yields a reduced density matrix ρ_{AB} , which is block diagonal in \mathcal{Q}_{AB} . This, in turn, ensures that the SROE is well defined. This reasoning also extends to mixed states that are block diagonal with respect to the charge operator: if the density matrix of the full system, ρ_{ABC} , commutes with $\mathcal{Q}_A + \mathcal{Q}_B + \mathcal{Q}_C$, then $\rho_{AB} = \text{Tr}_C(\rho_{ABC})$ commutes with \mathcal{Q}_{AB} and the above discussion also applies. This is because $[\mathcal{Q}_{AB}, \rho_{AB}] = \text{Tr}_C([\mathcal{Q}_{AB}, \rho_{ABC}]) = \text{Tr}_C([\mathcal{Q}_A + \mathcal{Q}_B + \mathcal{Q}_C, \rho_{ABC}]) - \text{Tr}_C([\mathcal{Q}_C, \rho_{ABC}]) = -\text{Tr}_C([\mathcal{Q}_C, \rho_{ABC}])$ and it vanishes due to the cyclicity of the partial trace over C . In this paper, we always deal with full-system density matrices ρ_{ABC} that commute with $\mathcal{Q}_A + \mathcal{Q}_B + \mathcal{Q}_C$.

IV. OPERATOR ENTANGLEMENT IN THE QUENCH DYNAMICS OF TRAPPED IONS

Let us now come to one of the main results of the paper: the development of tractable methods to extract Rényi α -OE in an experiment and the corresponding experimental observations of the entanglement barriers with Rényi 2-OE and its symmetry resolution.

In Sec. IV A we detail the experimental protocol of classical shadows and, in Sec. IV B, the associated efficient method for the postprocessing of the measurement data, dubbed the *batch-shadows estimator*. We discuss the experimental results in Secs. IV C and IV D.

A. Rényi OE from randomized measurements

In the previous sections, we have expressed OE as a function of the Schmidt spectrum $\{\lambda_i\}$. In order to express estimators of these quantities based on experimental data, one needs to rewrite them into a functional of the density matrix ρ_{AB} . In particular, the Rényi 2-OE is a fourth-order

function of ρ_{AB} that is explicitly written as follows [29,65]:

$$S^{(2)} = -\log \frac{\text{Tr}(\mathcal{S} \rho_{AB}^{\otimes 4})}{\text{Tr}(\rho_{AB}^2)^2} = \tilde{S}^{(2)}(\rho_{AB}) - 2R^{(2)}(\rho_{AB}), \quad (16)$$

where $\mathcal{S} = \mathbb{S}_{1,4}^{(A)} \otimes \mathbb{S}_{2,3}^{(A)} \otimes \mathbb{S}_{1,2}^{(B)} \otimes \mathbb{S}_{3,4}^{(B)}$ is defined in terms of the swap operators $\mathbb{S}_{k,l}^{(X)}$ that swap the k th and l th copies of system X (see Appendix A). We also define the unnormalized Rényi 2-OE $\tilde{S}^{(2)}(\rho_{AB}) = -\log(\text{Tr}(\mathcal{S} \rho_{AB}^{\otimes 4}))$ and we note that $R^{(2)}(\rho_{AB})$ can also be written in a similar form, as $R^{(2)}(\rho_{AB}) = -\log(\text{Tr}(\mathbb{S}_{1,2}^{(AB)} \rho_{AB}^{\otimes 2}))$. We present similar expressions for the SROE in Appendix E.

Such functionals on N -qubit density matrices can be accessed in qubit experiments via randomized measurements [48,49,65], as shown in Fig. 1(a). We start with the preparation of our N -qubit state in the experiment. We apply local random unitaries u_i ($i = 1, \dots, N$), sampled from the circular unitary ensemble (CUE) or a unitary 2-design, to each qubit separately and subsequently measure them in the z basis. The measurement outcomes are recorded as a bit string $s = s_1, \dots, s_N$. We repeat this procedure for a set of N_u distinct unitaries $u^{(r)}$ (of the form $u_1 \otimes \dots \otimes u_N$) and collect, for each thus applied unitary, N_M bit strings $s^{(r,m)} = s_1^{(r,m)}, \dots, s_N^{(r,m)}$ with $r = 1, \dots, N_u$ and $m = 1, \dots, N_M$. These recorded data can then be used to construct operators:

$$\hat{\rho}^{(r,m)} = \bigotimes_{i=1}^N \left[3(u_i^{(r)})^\dagger \left| s_i^{(r,m)} \right\rangle \left\langle s_i^{(r,m)} \right| (u_i^{(r)} - \mathbb{I}_2) \right]. \quad (17)$$

These operators are called *classical shadows* [49] and constitute independent unbiased estimators of the underlying quantum state, in the sense that $\mathbb{E}[\hat{\rho}^{(r,m)}] = \rho$, where the expectation value is taken over the applied unitaries and measurement outcomes (see also Appendix C). One can also perform appropriate robust estimations in the presence of an unknown noise channel by constructing robust versions of these classical shadows [86–88].

In order to measure functions $X_n = \text{Tr}(O^{(n)} \rho^{\otimes n})$ that are expectation values of a n -copy observable $O^{(n)}$ [here, in particular, we are interested in $O^{(4)} = \mathcal{S}$ on four copies; see Eq. (16)], one can define a U-statistics estimator \hat{X}_n , given by

$$\hat{X}_n = \frac{1}{n!} \binom{N_u}{n}^{-1} \sum_{r_1 \neq \dots \neq r_n} \text{Tr} \left[O^{(n)} \bigotimes_{i=1}^n \hat{\rho}^{(r_i)} \right], \quad (18)$$

where we introduce the classical shadow $\hat{\rho}^{(r)} = \mathbb{E}_{N_M}[\hat{\rho}^{(r,m)}]$ constructed by averaging over all measured bit strings for an applied unitary $u^{(r)}$. The estimator \hat{X}_n is unbiased, i.e., $\mathbb{E}[\hat{X}_n] = X_n$ [49].

This estimator has been used to access experimentally properties involving observables on up to $n = 3$ copies [8,52,53]. However, the underlying procedure quickly becomes computationally unfeasible and impractical, as it requires summing over all possible combinations of n distinct shadows $\hat{\rho}^{(r_1)}, \dots, \hat{\rho}^{(r_n)}$ for $r_i \in [1, \dots, N_u]$. Furthermore, its run time scales with the number of terms involved in the above sum: $\mathcal{O}(N_u^n)$, a number that grows exponentially with the polynomial degree n . In practice, this scaling prevents us from extracting the Rényi 2-OE from the experimental data of Ref. [7] (as $n > 3$). Thus we are in dire need of an alternative method with a substantially reduced run time.

B. Fast estimation of high-order functionals using randomized measurements data via batch shadows

In order to improve the postprocessing run time of classical shadows, we propose to form $b = 1, \dots, n' \geq n$ “batch shadows,” each of which is an average of N_u/n' shadows (assuming, for simplicity, that N_u/n' is an integer): $\tilde{\rho}^{(b)} = (n'/N_u) \sum_{r=(b-1)N_u/n'+1}^{bN_u/n'} \hat{\rho}^{(r)}$. This allows us to define an alternative unbiased estimator

$$\tilde{X}_n^{(n')} = \frac{1}{n!} \binom{n'}{n}^{-1} \sum_{b_1 \neq \dots \neq b_n} \text{Tr} \left[O^{(n)} \bigotimes_{i=1}^n \tilde{\rho}^{(b_i)} \right], \quad (19)$$

which is different from Eq. (18) and easier to compute. The first step involves the construction of the n' batch shadows $\tilde{\rho}^{(b)}$, which obey $\mathbb{E}[\tilde{\rho}^{(b)}] = \rho$ for all batches $b = 1, \dots, n'$. This is achieved by summing up all classical shadows that belong to a respective batch—a subroutine that requires $\mathcal{O}(N_u)$ arithmetic operations (provided that the sample complexity N_u exceeds the total number of degrees of freedom in the reduced density matrix). These individual summation steps can obviously be parallelized on n' cores. Note also that, in contrast to the bare classical shadows $\hat{\rho}^{(r,m)}$, the batch shadows $\tilde{\rho}^{(b)}$ are stored in memory as dense $2^N \times 2^N$ matrices. For typical memory available on current hardware, this limits our fast estimation methods to system sizes of up to $N \approx 15$ qubits. In principle, for $N > 15$, such memory requirements can be reduced by, for instance, compressing the batch shadows with matrix-product operators [89] (at the cost of approximating the underlying quantum state with a finite OE entropy).

The second step requires the evaluation of $\tilde{X}_n^{(n')}$ from the constructed batch shadows, which scales as $\mathcal{O}(n'^n)$. Thus by choosing $n' = n$ and assuming that $N_u \gg n^n$, we obtain the fastest estimator with an evaluation time $\mathcal{O}(N_u)$. This is a drastic run-time improvement compared to the original U-statistics estimator in Eq. (18): $\mathcal{O}(N_u)$ steps (new) versus $\mathcal{O}(N_u^n)$ steps (old). As we increase n' , one starts to incorporate more terms with distinct combinations of n different shadows that were not previously considered. This progression terminates in an eventual convergence to the

original U-statistics estimator, i.e., $\tilde{X}_n^{(N_u)} = \hat{X}_n$, as well as in an increase in the postprocessing run time. In order to gauge the performance of the estimator $\hat{X}_n^{(n')}$, we study its statistical-error behavior.

The *statistical errors* in randomized measurements arise due to applying a finite number of random unitaries N_u and performing a finite number of readout measurements N_M . The statistical errors of any estimator \hat{X} are governed by its variance $\text{Var}[\hat{X}]$. One can provide rigorous performance guarantees to estimate X_n with an accuracy ϵ from our protocol by bounding this variance and subsequently applying Chebyshev's inequality: $\text{Pr}[|\hat{X}_n^{(n')} - X_n| \geq \epsilon] \leq \text{Var}[\hat{X}_n^{(n')}] / \epsilon^2$. In Appendix C, we provide a general framework that can be applied to calculate variance bounds on the batch-shadow estimator for arbitrary multicopy operators. We can then provide rigorous performance guarantees for our estimation formulas, which we can also compare with the results for classical shadows presented in Ref. [90].

From this study, in the limit of $N_M = 1$, as elaborated in Appendix C 2, we note that $\text{Var}[\hat{X}_n^{(n')}]$ and $\text{Var}[\hat{X}_n]$ have the same scaling behavior in the high-accuracy regime of $\epsilon \rightarrow 0$: that is, at first order in $1/N_u$, they both scale $\propto n^2/N_u$ with the same proportionality constant. Moreover, for $n' = n$, at second order in $1/N_u$, $\text{Var}[\tilde{X}_n^{(n)}]$ exceeds $\text{Var}[\hat{X}_n]$ by only a small factor of $n/(n-1)$. This shows that the required number of measurements to achieve a given accuracy ϵ is essentially the same for the fast batch-shadow estimator [Eq. (19)] and the standard shadow estimator [Eq. (18)].

Of course, we can apply our general variance bound formalism to the quantities of interest for this work— $O^{(2)} = \mathbb{S}_{1,2}^{(AB)}$ and $O^{(4)} = \mathcal{S}$ —that give access to $R^{(2)}(\rho_{AB})$ and $\tilde{S}^{(2)}(\rho_{AB})$, respectively. In the case of Clifford shadows (i.e., each random unitary is chosen uniformly from the single-qubit Clifford group) and $n' = n$, we find that in order to estimate them with a confidence interval of δ , i.e., to make sure that $\text{Pr}[|\tilde{X}_n^{(n)} - X_n| \geq \epsilon] \leq \delta$, we require a number of measurements that scale as $N_u \propto 3^N / \epsilon^2$ with N (for further details, see Appendixes C 3 and C 4). Hence, in the worst-case scenario, our measurement bound of the batch-shadow estimator of $\tilde{X}_n^{(n)}$ scales as 3^N irrespective of the order $n = 2, 4$. For evaluating $\tilde{S}^{(2)}(\rho_{AB})$, in particular, this measurement bound is a polynomial improvement over the best previously obtained bounds, which only achieve 4^N [65]. We conjecture that this desirable scaling persists when we increase α to evaluate higher-order Rényi α -OE. We also complement these rigorous bounds with small-scale numerical simulations in Appendix C 5.

C. Experimental results using batch shadows

The batch-shadow formalism allows us to extract experimentally the Rényi 2-OE along with its symmetry

resolution. We perform our set of observations by reprocessing batch shadows from the randomized-measurement data of two sets of experiments, where a global quench with a long-range XY model has been realized on a string of 10 and 20 qubits (ions), respectively [7]. The initial state was a Néel state, $|\psi\rangle = |01\rangle^{\otimes N/2}$, with vanishing operator (and state) entanglement entropy. The global quench was followed by the implementation of randomized-measurement protocol involving a total of $N_u = 500$ Haar-random unitaries. For each of the applied unitaries, $N_M = 150$ bit-string measurements were carried out. Details on the modeling of quench dynamics with tensor-network algorithms and the protocol are discussed in Appendix D.

We consider two bipartite reduced density matrices ρ_{AB} defined on the subsystems $A = [2, 3]$ and $B = [4, 5]$ and $A = [8, 9]$ and $B = [10, 11]$ for a total chain of 10 and 20 ions, respectively, where we label the ions along the chain from 1 to N . Our observations remain unchanged for other partitions. Figures 1(b) and 1(c) and Fig. 2 show the experimental results with corresponding numerical simulations both with and without decoherence of the experiment. Figures 2(a) and 2(b) highlight the extracted Rényi 2-OE with the simplest batch-shadow estimator ($n' = 4$).

We first observe the entanglement barrier for the considered partition of the 20-ion system in Figs. 1(b) and 2(a). We observe a barrier composed of a growth phase from $t = 0$ to $t \approx 3$ ms and a decay phase from $t \approx 3$ ms to the last data point at $t = 10$ ms. The peak at $t \approx 3$ ms actually looks more like a double peak with maxima at $t \approx 1.8$ ms and $t \approx 3.8$ ms. We interpret this as oscillations on top of the main barrier caused by the small size of subsystems A and B . This interpretation is supported by the fact that similar finite-size effects are found in our free-fermion model, as shown in Fig. 2(d) (see also Sec. V). The growth phase at early times signals the creation of correlations between the two subsystems A and B , while the decay phase reflects the fact that ρ_{AB} goes toward a thermal-like density matrix with small OE. Since the system is finite, we also expect revivals of the OE at longer times; however, such revivals are not yet visible in the available time window. The barrier can also be understood as a competition between the terms $\tilde{S}^{(2)}(\rho_{AB})$ and $R^{(2)}(\rho_{AB})$ in the respective regimes, as shown in Fig. 2(c) [36]. In the growth phase, the unnormalized Rényi 2-OE $\tilde{S}^{(2)}(\rho_{AB})$ grows at a faster rate compared to the state entropy $2R^{(2)}(\rho_{AB})$. In the decay phase, this behavior is inverted. These general features are consistent with the theoretical predictions of different models shown in Refs. [29,36,91].

Comparing Figs. 2(a) and 2(b), we see, however, that in the smaller system of 10 ions, no similar barrier is found. In particular, we do not observe the decay phase. We discuss this case in more detail in Sec. IV D.

Overall, Figs. 2(b) and 2(d) show excellent agreement of the experimental data with the numerically modeled results

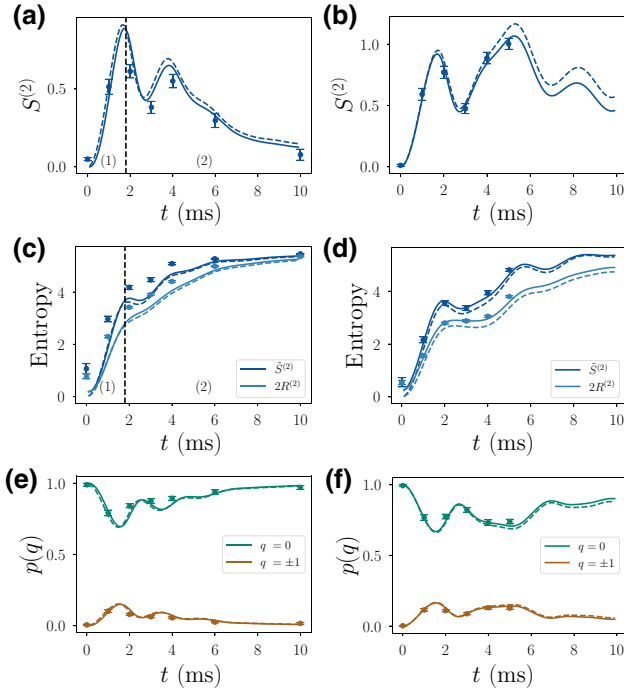


FIG. 2. Additional experimental observations: (a),(b) the measured Rényi 2-OE and, correspondingly, (c),(d) the measured values of $\tilde{S}^{(2)}(\rho_{AB})$ and $R^{(2)}(\rho_{AB})$ relating to Rényi 2-OE as in Eq. (16) for a reduced density matrix of four ions from a total system consisting of $N = 20$ (left panels) and $N = 10$ (right panels). We observe the two phases of the entanglement barrier, which are separated by a black vertical dashed line for (a) and (c), given by: (1) the growth phase followed by (2) the decay phase. (e),(f) The corresponding populations $p(q)$ for symmetry sectors $q = 0, \pm 1$, on a reduced density matrix of four ions taken from their respective total systems of $N = 20$ and $N = 10$. The points show experimental results with the error bars calculated using jackknife resampling. The lines correspond to numerical simulations of the unitary dynamics (dashed) and including dissipation (solid).

for the 10-ion experiment. On the other hand, it is quite surprising to see that even though the individual estimations of $\tilde{S}^{(2)}(\rho_{AB})$ and $R^{(2)}(\rho_{AB})$ from the 20-ion experiment as shown in Fig. 2(c) have systematic shifts of the experimentally measured values, likely caused due to an imperfect modeling of decoherence during the experiment and the measurement protocol, the corresponding measured Rényi 2-OE shows quite good agreement with the theoretical model, as in Fig. 2(a). This suggests a robustness feature of the Rényi 2-OE where errors in estimations of the two terms compensate each other. We also remark that the measured values of Rényi 2-OE are lower, as shown in Figs. 2(a) and 2(b) from the numerical simulations of the experiment.

For the present model, the conserved quantity is the magnetization, i.e., $Q_{AB} = \sum_{i \in AB} \sigma_i^z$, where σ_i^z is the z -Pauli matrix acting on the ion qubit i (cf. Appendix D).

The corresponding symmetry resolutions for the considered bipartitions of $N = 20$ and $N = 10$ ions are shown in Figs. 1(b) and 1(c). Their respective populations in a given symmetry sector q are given by $p(q) = \text{Tr}(\Pi_q \text{Tr}_B(|\rho_{AB}\rangle \langle \rho_{AB}|)) / \text{Tr}(\rho_{AB}^2)$, where Π_q is the projector onto the eigenspace of the charge sector q for system A ($q = 0$ being the sector initially populated). This is highlighted in Figs. 2(e) and 2(f), respectively. At $t = 0$, we see that the $q = 0$ sector is substantially populated, while the other sectors with $q = \pm 1$ increase in population as a function of time. In particular, for the 20-ion system, as shown in Fig. 2(e), we observe very low population for the section $q = \pm 1$, as it decays as a function of time. This and the finite-measurement statistics available from the experiment prevent us from resolving the experimental points for the symmetry-resolution sector of $q = \pm 1$ for later times. In general, we also observe, from Figs. 1(b) and 1(c), that the sector $q = 0$ follows the features of the Rényi 2-OE. This translates, as shown in Fig. 1(b), to an entanglement barrier for the $q = 0$ sector for the 20-ion system. One can also note the absence of the barrier for the $q = 0$ sector from the symmetry resolution of the 10-ion system.

D. Interpretation in the quasiparticle picture

Interestingly, our experimental results can also be interpreted based on free-fermion calculations detailed in Sec. V, with which we can qualitatively reproduce the behavior of the OE and the SROE for systems of 10 and 20 qubits. The analogy between the experimental setup and our free-fermion model originates in the fact that the breaking of integrability in the experiment is weak [92,93]. Therefore, the short-time dynamics are comparable to those of an integrable system, where entanglement generation can be qualitatively understood in terms of entangled pairs of quasiparticles propagating freely through the system [21]. Deviations from integrable dynamics become relevant only on longer time scales, which are not accessible with the available data. As pointed out above, comparing Figs. 1(b) and 1(d) for 20 qubits and 20 fermionic sites, respectively, we observe the same barrier shape for the OE, with oscillations due to the small subsystem size. The same barrier is found for the SROE for $q = 0$, while for $q = \pm 1$, there is no apparent decay of the OE at long times.

We now come back to the fact that we do not observe a single-peaked barrier for 10 ions [see Figs. 1(c) and 2(b)]. Importantly, this feature is also noticeable in our free-fermion simulations with 10 sites [see Fig. 1(e)]. Instead of a single barrier, the free-fermion OE displays a double-peaked shape. The second peak can be understood from a quasiparticle picture as a consequence of the subsystem A being particularly close to the boundary, as we now explain.

Recall that $A = [2, 3]$ and $B = [4, 5]$ for the chain of 10 ions, with ions labeled from 1 to 10. Importantly, part C

then consists of two asymmetric pieces, $C = \{1\} \cup [6, 10]$, with a very short domain on the left and a longer one on the right. The first growth phase of the OE is interpreted as originating from pairs of quasiparticles, initially located at the same position, that travel through the system in opposite directions and generate entanglement when one member of the pair is in A and the other is in B . This interpretation of entanglement growth is usually given for the standard entanglement entropy [20] but also carries over to the OE. After the OE reaches its first maximum, it decreases, because some quasiparticles that formerly belonged to pairs shared between A and B arrive in C and therefore stop contributing to the OE of ρ_{AB} . If subsystems A and B were far away from the boundaries, then the OE would ultimately go to zero, as the number of pairs shared between A and B would eventually vanish. This does not happen here, because the particles that escape from A to C (i.e., go from site 2 to site 1 in the chain) are soon reflected against the left boundary of the system. Consequently, they come back and are reinjected into A . As a result, the OE grows again, which explains the second peak in Fig. 1(e). The decay of that second peak occurs because, after the reflection, both members of a pair travel to the right, so that they ultimately escape to the right half system [6, 10].

The decay of the second peak is not visible in the experiment [see Fig. 1(c)]. Based on our numerical simulations of the experiment, as shown in Fig. 2(b), we observe a decay occurring at a later time, which is not accessible within the time window of the 10-ion experiment.

It should be possible to adapt the quasiparticle picture to describe both the experimental data and our free-fermion results more quantitatively, following what is done for the time evolution of the entanglement entropy in nearly integrable dynamics; see, e.g., Ref. [94], which implements previous ideas for local observables [95]. This, however, is far beyond the scope of this paper.

V. SYMMETRY-RESOLVED OPERATOR ENTANGLEMENT IN FREE-FERMION CHAINS

So far, we have presented results for finite-size systems, in direct connection with the experimental setup. We show in Fig. 1 that the qualitative features of the trapped-ion experimental setup can also be observed in free-fermion chains under unitary evolution, despite the fact that these free-fermion models are short ranged and have no dissipation.

This raises the question as to whether one can understand more about the OE and the SROE of the reduced density matrix by studying free-fermion chains in the thermodynamic limit. In this section, we show that the thermodynamic limit can be tackled analytically, unveiling some interesting properties of the SROE, such as the time delay of the charge sectors or the equipartition.

A direct analytical calculation of the SROE from the definition given in Eq. (14) is difficult but we can apply a trick similar to what has been done for the standard entanglement resolution [67,68,76,96], consisting in computing instead the charged moments of the reduced density matrix. Using the vectorization of the operator ρ_{AB} , $|\rho_{AB}\rangle$, the object that we want to compute is

$$\mathcal{Z}_\alpha(q) = \sum_j (\lambda_j^{(q)})^{2\alpha} = \frac{\text{Tr}[\Pi_q (\text{Tr}_{B \otimes B}(|\rho_{AB}\rangle \langle \rho_{AB}|))^\alpha]}{(\text{Tr}[\rho_{AB}^2])^\alpha}, \quad (20)$$

where q labels the (integer) eigenvalues of \mathcal{Q}_A and Π_q is the projector on the corresponding eigenspace of \mathcal{Q}_A , as already mentioned above. To do so, we use the Fourier representation of Π_q ,

$$\Pi_q = \int_{-\pi}^{\pi} \frac{d\theta}{2\pi} e^{-iq\theta} e^{i\theta \mathcal{Q}_A}. \quad (21)$$

Plugging Eq. (21) into Eq. (20), we obtain

$$\mathcal{Z}_\alpha(q) = \int_{-\pi}^{\pi} \frac{d\theta}{2\pi} e^{-iq\theta} Z_\alpha(\theta), \quad (22)$$

where the charged moment $Z_\alpha(\theta)$ is defined as

$$Z_\alpha(\theta) = \frac{1}{(\text{Tr}[\rho_{AB}^2])^\alpha} \text{Tr}[(\text{Tr}_{B \otimes B}(|\rho_{AB}\rangle \langle \rho_{AB}|))^\alpha e^{i\theta \mathcal{Q}_A}]. \quad (23)$$

The charged moment is the main object that we need to evaluate; we explain how to do so in Sec. V A. In terms of Eq. (20), the SROE reads

$$S_q^{(\alpha)}(\rho_{AB}) = \frac{1}{1-\alpha} \log \frac{\mathcal{Z}_\alpha(q)}{[\mathcal{Z}_1(q)]^\alpha}, \quad (24)$$

while in terms of Eq. (23) the total OE is

$$S^{(\alpha)}(\rho_{AB}) = \frac{1}{1-\alpha} \log Z_\alpha(0). \quad (25)$$

A. Free-fermion techniques for the OE

For the eigenstates of quadratic lattice Hamiltonians, it is possible to compute the entanglement entropies in terms of the eigenvalues of the correlation matrix of the subsystem [97,98]. This trick can also be applied for the computation of the OE and, more generally, of the charged moments in Eq. (23).

Let us take a free-fermion chain of length N with $U(1)$ symmetry, described by the Hamiltonian

$$H = -\frac{J}{2} \sum_{i=1}^N (c_{i+1}^\dagger c_i + \text{h.c.}), \quad (26)$$

where c_i^\dagger (c_i) is the creation (annihilation) operator such that the anticommutator obeys $\{c_i, c_j^\dagger\} = \delta_{ij}$ and also $c_{N+1} = c_1, c_{N+1}^\dagger = c_1^\dagger$, i.e., we impose periodic boundary conditions. For the sake of simplicity, we set $J = 1$ from now on and remind the reader that we do the same for the reduced Planck constant ($\hbar = 1$) and the lattice constant $a = 1$. The reduced density matrix ρ_{AB} for a subsystem $A \cup B$, where $A \cup B = [1, \ell_A] \cup [\ell_A + 1, \ell_A + \ell_B]$, consisting of two adjacent intervals, can be put in a diagonal form as

$$\rho_{AB} = \bigotimes_{k=1}^{\ell_A + \ell_B} \frac{e^{-\lambda_k d_k^\dagger d_k}}{1 + e^{-\lambda_k}}, \quad (27)$$

where $e^{-\lambda_k} = n_k / (1 - n_k)$, with n_k being the occupation number at a given wave vector k and the d_k defined as fermionic operators satisfying $\{d_k, d_{k'}^\dagger\} = \delta_{kk'}$. It is more convenient to write Eq. (27) as

$$\begin{aligned} \rho_{AB} &= \bigotimes_{k=1}^{\ell_A + \ell_B} \frac{|0\rangle_k \langle 0|_k + e^{-\lambda_k} |1\rangle_k \langle 1|_k}{1 + e^{-\lambda_k}} \\ &= \bigotimes_{k=1}^{\ell_A + \ell_B} [(1 - n_k) |0\rangle_k \langle 0|_k + n_k |1\rangle_k \langle 1|_k], \end{aligned} \quad (28)$$

so that by applying the vectorization trick in Eq. (3) for ρ_{AB} , we obtain

$$\begin{aligned} \frac{|\rho_{AB}\rangle}{\sqrt{\text{Tr}[\rho_{AB}^2]}} &= \bigotimes_{k=1}^{\ell_A + \ell_B} \frac{[(1 - n_k) |0\rangle_k |0\rangle_{\bar{k}} + n_k |1\rangle_k |1\rangle_{\bar{k}}]}{\sqrt{n_k^2 + (1 - n_k)^2}} \\ &= \bigotimes_{k=1}^{\ell_A + \ell_B} \frac{[1 - n_k + n_k d_k^\dagger \tilde{d}_k^\dagger] |0\rangle}{\sqrt{n_k^2 + (1 - n_k)^2}}, \end{aligned} \quad (29)$$

where the \tilde{d}_k operators are copies of the d_k operators introduced in the vectorization process and $|0\rangle$ is the state annihilated by all the d_k and \tilde{d}_k operators. This is the starting pure-ket vector from which we can build the (super-)reduced density matrix $\text{Tr}_{B \otimes B}(|\rho_{AB}\rangle \langle \rho_{AB}|)$. The

correlation matrix of the state $|\rho_{AB}\rangle$ reads

$$\begin{aligned} C_{kk'} &= \langle \rho_{AB} | \begin{pmatrix} d_k^\dagger \\ \tilde{d}_k \end{pmatrix} \begin{pmatrix} d_{k'} \\ \tilde{d}_{k'}^\dagger \end{pmatrix} | \rho_{AB} \rangle \\ &= \frac{\delta_{kk'}}{n_k^2 + (1 - n_k)^2} \begin{pmatrix} n_k^2 & n_k(1 - n_k) \\ n_k(1 - n_k) & (1 - n_k)^2 \end{pmatrix}. \end{aligned} \quad (30)$$

In the basis of d_k and \tilde{d}_k operators, the supercharge operator takes the form

$$\mathcal{Q} = \left(\sum_k d_k^\dagger d_k \right) \otimes \mathbb{1} - \mathbb{1} \otimes \left(\sum_k \tilde{d}_k^\dagger \tilde{d}_k \right)^T. \quad (31)$$

We can collect the operators into the vector $\mathbf{f} = (d_1, \dots, d_{\ell_A + \ell_B}, \tilde{d}_1^\dagger, \dots, \tilde{d}_{\ell_A + \ell_B}^\dagger)^T$ (making the identity operators in Eq. (31) implicit, for simplicity, and noting we can ignore the transpose) such that \mathcal{Q} reads $\mathcal{Q} = \mathbf{f}^\dagger \mathbf{f} - (\ell_A + \ell_B)$, where $\ell_A + \ell_B$ just acts as an additive constant here.

At this point, we can compute the $2(\ell_A + \ell_B) \times 2(\ell_A + \ell_B)$ correlation matrix as

$$C_{AB} = \bigoplus_{k=1}^{\ell_A + \ell_B} C_{kk}, \quad (32)$$

and by doing a Fourier transform, we can write C_{AB} in the spatial basis. To evaluate the charged moments in Eq. (23), we just have to focus on subsystem A , i.e., we can restrict the supercharge operator to \mathcal{Q}_A and the Fourier transform of the correlation matrix in Eq. (32) to the subspace corresponding to subsystem A . Diagonalizing the latter matrix, we obtain $2\ell_A$ real eigenvalues ξ_i between 0 and 1.

Therefore, one can compute the charged moments of the reduced density matrix built from $|\rho_{AB}\rangle$ in terms of the eigenvalues ξ_i as

$$Z_\alpha(\theta) = e^{-i\theta(\ell_A + \ell_B)} \prod_{a=1}^{2\ell_A} (\xi_a^\alpha e^{i\theta} + (1 - \xi_a)^\alpha). \quad (33)$$

Using Eqs. (22) and (24), we can compute exactly the SROE for the reduced density matrix of a free-fermion chain. The same trick also allows the computation of the total Rényi α -OE, as

$$S^{(\alpha)}(\rho_{AB}) = \frac{1}{1 - \alpha} \sum_{a=1}^{2\ell_A} \log[\xi_a^\alpha + (1 - \xi_a)^\alpha]. \quad (34)$$

B. Charged moments: A quasiparticle picture

Let us now consider a global quantum quench from an initial conformal invariant state with an evolution Hamiltonian given by the continuum limit of Eq. (26) [99]. The

emerging quasiparticles move with a single velocity and, in the space-time scaling limit $t, \ell_A, \ell_B \gg \tau_0$ (with τ_0 an ultraviolet cutoff), we can introduce the function (assuming, without loss of generality, $\ell_A \leq \ell_B$)

$$f_{\ell_A, \ell_B}(t) = \begin{cases} t, & \text{for } 0 \leq 2t \leq \ell_A, \\ \ell_A/2, & \text{for } \ell_A \leq 2t \leq \ell_B, \\ (\ell_A + \ell_B)/2 - t, & \text{for } \ell_B \leq 2t \leq (\ell_A + \ell_B), \\ 0, & \text{for } (\ell_A + \ell_B) \leq 2t, \end{cases} \quad (35)$$

so that the charged moments read

$$\log Z_\alpha(\theta) = \frac{\pi \Delta_\alpha^\theta}{\tau_0} f_{\ell_A, \ell_B}(t), \quad (36)$$

where [67]

$$\Delta_\alpha^\theta = \frac{1}{12} \left(\alpha - \frac{1}{\alpha} \right) + \frac{1}{\alpha} \left(\frac{\theta}{2\pi} \right)^2. \quad (37)$$

From this result, which is valid for a conformal field theory (CFT), one can formulate a quasiparticle picture for the charged moments of free-fermion models with global conserved $U(1)$ charge, the quench dynamics of which start from initial states that are also invariant under $U(1)$ symmetry. This is obtained from the CFT result in Eq. (36) by first replacing $t \rightarrow |v(k)|t$, with $|v(k)|$ being the velocity of quasiparticles, which for conformal invariant systems is fixed to be $v(k) = 1$. Then, we should integrate over the quasiparticles with quasimomentum k but properly accounting for the density (in momentum space) of the thermodynamic charged moments $z_\alpha(k, \theta)$ in the stationary state [21,100,101]. The latter can be inferred from the results for charged moments of state entanglement [69,70] and the final result is the replacement $\pi \Delta_\alpha^\theta / \tau_0 \rightarrow 2z_\alpha(k, \theta)$:

$$\log Z_\alpha(\theta) = \int_{-\pi}^{\pi} \frac{dk}{2\pi} 2z_\alpha(k, \theta) f_{\ell_A, \ell_B}(|v(k)|t). \quad (38)$$

In order to have a predictive formula, one has to fix the function $z_\alpha(k, \theta)$ in Eq. (38). Here, we focus on out-of-equilibrium protocols for free-fermion models, the time evolution of which is given by the Hamiltonian in Eq. (26). In this case, $z_\alpha(k, \theta)$ is determined from the population of the modes n_k of the postquench Hamiltonian in the stationary state [101,102] and it reads

$$z_\alpha(k, \theta) = \log[e^{i\theta} n_k^\alpha + (1 - n_k)^\alpha] - i\theta/2. \quad (39)$$

For concreteness, from now on we restrict to a quench from the Néel state, for which $n_k = 1/2$ for all k [70], so that the

charged moment [in Eq. (38)] becomes

$$\log Z_\alpha(\theta) = [2(1 - \alpha) \log 2 + 2 \log(\cos(\theta/2))] \mathcal{J}(t) \quad (40)$$

where $\mathcal{J}(t)$ is defined as

$$\mathcal{J}(t) = \int_{-\pi}^{\pi} \frac{dk}{2\pi} f_{\ell_A, \ell_B}(|v(k)|t) \quad (41)$$

and $|v(k)| = |\sin(k)|$. The function $\mathcal{J}(t)$ displays the same qualitative features of Eq. (36), where $|v(k)| = 1$: $\mathcal{J}(t)$ grows until $t < \ell_A/2$, then presents a plateau barrier in the range $\ell_A/2 < t < \ell_B/2$, then decays again for $\ell_B/2 < t < (\ell_A + \ell_B)/2$, and, eventually, saturates to 0 for $t > (\ell_A + \ell_B)/2$. In other words, $\mathcal{J}(t)$ behaves as a barrier, a characteristic that we also find for the SROE. For the sake of completeness, we report explicitly the result for the total OE using Eq. (25), which reads

$$S^\alpha(\rho_{AB}) = 2 \log 2 \mathcal{J}(t). \quad (42)$$

We observe that the result does not depend on α , which suggests that, in the scaling limit in which we are interested, the spectrum of the super-reduced density matrix becomes flat. We plot this result against the exact lattice calculations in Fig. 1(f).

C. Time delay, barrier, and equipartition

From the computation of the charged moments done above, the symmetry-resolved moments read

$$\mathcal{Z}_\alpha(q) = 2^{2(1-\alpha)\mathcal{J}(t)} \int_{-\pi}^{\pi} \frac{d\theta}{2\pi} e^{-i\theta q} \left(\cos \frac{\theta}{2} \right)^{2\mathcal{J}(t)}. \quad (43)$$

As already pointed out for the usual symmetry-resolved entropies in Ref. [69,70], this expression formally assumes negative values for $\mathcal{J}(t) < |q|$, so it means that we have to replace it with $\mathcal{Z}_\alpha(q) = 0$. This allows us to identify a *delay time* t_D such that the SROE in a given charge sector starts only after t_D . The equation $\mathcal{J}(t_D) = |q|$ reads [as long as $v_M t_D < \frac{1}{2} \text{Min}(\ell_A, \ell_B)$ self-consistently and $v_M \equiv \max(v(k)) = 1$]

$$\int_{-\pi}^{\pi} \frac{dk}{2\pi} |\sin(k)| t_D = |q| \quad (44)$$

and we can conclude that $t_D = \pi|q|/2$ for $|q| < \text{Min}(\ell_A, \ell_B)/\pi$. Therefore, and after simplification, we find that the SROE is given by

$$S_q^{(\alpha)}(\rho_{AB}) = \begin{cases} 0, & (t \leq t_D), \\ 2\mathcal{J}(t) \log 2 + \log \mathcal{Z}_1(q), & (t > t_D). \end{cases} \quad (45)$$

We remark that this expression does not depend on the Rényi index α , such as the total OE in Eq. (25). This

implies that the spectrum of the super-reduced density matrix is flat in each charge sector, similarly to what happens for standard symmetry-resolved entropies (see Ref. [70]). Note that for large $\mathcal{J}(t)$, i.e., in the scaling limit $\mathcal{J}(t) > |q| \gg 1$, the integral in Eq. (43) can be computed by saddle-point approximation, obtaining (for more details, see Ref. [70], where the same integral appears)

$$S_q^{(\alpha)}(\rho_{AB}) = 2\mathcal{J}(t)h\left(\frac{1+q/\mathcal{J}(t)}{2}\right), \quad (46)$$

where $h(x) = -x \log x - (1-x) \log(1-x)$ is the well-known binary entropy function. The comparison between this formula and the numerical results in the tight-binding model chain is displayed in the top-right panel of Fig. 1(f). The solid lines correspond to Eq. (46) for $t > t_D$, obtained from the saddle-point approximation of Eq. (43). The agreement is good and we can also observe that there are some charge sectors with zero entanglement for $t < t_D$. However, for $t > (\ell_A + \ell_B)/2$, the discrepancy between the numerics and the analytical prediction in Eq. (46) is larger. One explanation could be that at finite ℓ_A and t , the data exhibit some small corrections and our prediction is recovered only in the scaling limit $t, \ell_A, \ell_B \rightarrow \infty$, with their ratio fixed.

For $|q| \ll \mathcal{J}(t)$, we find from Eq. (46) that

$$S_q^{(\alpha)}(\rho_{AB}) = \mathcal{J}(t) \left(2 \log 2 - \frac{q^2}{\mathcal{J}(t)^2} \right). \quad (47)$$

This result states that for small $|q|$, there is an effective equipartition of the OE with violations of order $q^2/\mathcal{J}(t)$. This is also visible from Fig. 1(f), where we observe that, for small q , the total OE and the SROE are almost indistinguishable. We compare the exact result for the SROE in the scaling limit reported in Eq. (45) (solid lines), with its asymptotic expansions in Fig. 3. We note that as $\ell = \ell_A + \ell_B$ increases (here, $\ell_A = \ell_B$), the approximation in Eq. (46) (long-dashed lines) improves, since $\mathcal{J}(t)$ also increases. The short-dashed lines represent the further approximation in Eq. (47), which also improves as $\mathcal{J}(t)$ increases for the small charge value ($q = 4$) that we plot. We observe that the SROE is small both at short and at large times and that it blows up linearly in the transient regime $t \leq (\ell_A + \ell_B)/2$, as for the total OE [29].

We conclude by commenting on Figs. 1(d) and 1(e), obtained through the free-fermion techniques described in Sec. V A. We show that the dynamics of the SROE in the different charge sectors are affected by the finite size of the system. In particular, for $N = 20$, one can observe the entanglement barrier only in the sector $q = 0$, while for $q = 1$, the absence of the decay is consistent with the experimental results of Fig. 1(b). Moreover, for this system size, the total OE presents a single peak, while for $N = 10$, we note the presence of two peaks in the total OE, which

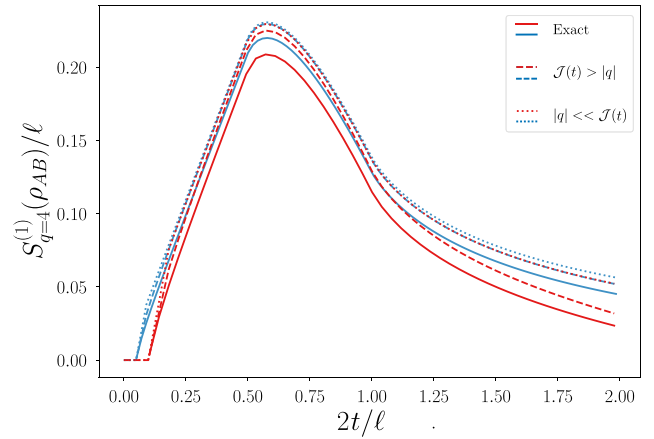


FIG. 3. The SROE in the scaling limit: a comparison between the analytical expression in Eq. (45) (solid line) and its asymptotic approximation in Eqs. (46) (long-dashed line) and (47) (short-dashed line). Here, $q = 4$ and $\ell = \ell_A + \ell_B$ with $\ell_A = \ell_B$; the blue line corresponds to $\ell = 256$, while the red ones to $\ell = 128$.

can be justified by the quasiparticle picture explained at the end of Sec. IV C.

VI. CONCLUSIONS

This paper is devoted to a thorough analysis regarding the OE of a reduced density matrix after a global quantum quench, as well as its symmetry resolution. These quantities first grow linearly in time, before they decrease again and eventually saturate to a finite value. The presence of such an entanglement barrier is strongly affected by the finite size of the system, as we demonstrate here, based on experimental data. This feature is also visible for free-fermion systems evolving under a unitary evolution.

The experimental results, also supported by tensor-network simulations, are obtained by a novel postprocessing method of randomized-measurement data, dubbed the batch-shadow estimator, that has practical applications to the probing of the nonlinear properties of quantum many-body systems. This method provides a faster and more efficient data-treatment technique with respect to the already known ones [48] and enables us to actually estimate the OE from existing experimental data [7].

We observe the presence of the entanglement barrier of the reduced density matrix of a partition of four ions out of $N = 20$, both for the total OE and its symmetry-resolved counterpart (SROE) in the charge sector $q = 0$. However, finite-size effects prevent the experimental observation of such a barrier in the charge sectors $q = \pm 1$ and for $q = 0$ in the case of $N = 10$. For $N = 20$, in the charge sectors $q = \pm 1$, the available measurement statistics only allow us to explore the early-time behavior of the SROE.

For small system sizes N , the phenomenology discussed in the previous paragraph can be also observed in

free-fermion systems without dissipation. Therefore, guided by conformal field theory and free-fermion techniques, we show that the semiclassical picture of moving quasiparticles [20,21] can be adapted to this context. This leads to a general conjecture for the charged OEs, the Fourier transform of which gives the desired SROE. Beyond the barrier, we observe a time delay proportional to the charge sector and an effective equipartition for small q .

Because of this phenomenology, we expect our main physical findings to show up for rather generic quench protocols. However, it would be very interesting to engineer situations in which some of them are absent, e.g., with the entanglement barrier appearing only in certain charge sectors, breaking equipartition.

It is worthwhile pointing out that the time evolution of the total OE is closely related to other entanglement measures such as the reflected entropy [103,104] (which is the OE of $\sqrt{\rho_{AB}}$), negativity [105–108], and temporal entanglement [109–111]: in these latter cases, the connection is merely technical but the fact that they can be computed in a similar way leads to analogous results, such as the entanglement barrier of the logarithmic negativity after a quench [112]. Our work naturally paves the way for their symmetry resolution and for an understanding of whether their connection can be understood sector by sector.

To conclude, we remark that the OEs of operators different from the reduced density matrix are known to capture important universal properties of the dynamics [26–29, 32,36,91,113–115]. For instance, the OE of the evolution operator $U(t) = e^{-iHt}$ grows linearly in ergodic phases [29, 113] but only logarithmically in localized phases [28,29]. Another example is the OE of a local operator O evolving

in the Heisenberg picture, i.e., $O(t) = e^{iHt} O e^{-iHt}$. There, the OE grows linearly in systems with chaotic dynamics [113] but only logarithmically for integrable dynamics [91,114,115]. It is then natural to wonder what happens to their symmetry-resolved (SR) version, which certainly deserves future investigation.

ACKNOWLEDGMENTS

V.V. is grateful to A. Santini for useful discussions on related topics. We thank A. Elben for helping us to reprocess the experimental data of Ref. [7]. P.C. and S.M. acknowledge support from the European Research Council (ERC) under Consolidator Grant No. 771536 [“New states of Entangled Matter Out of equilibrium” (NEMO)]. A.R. is grateful for the support by Laboratoire d’excellence Laboratoire d’Alliances Nanoscience-Energies du Futur (LANEF) in Grenoble (ANR-10-LABX-51-01) and from the Grenoble Nanoscience Foundation. B.V. and M.V. acknowledge funding from the French National Research Agency (ANR) [ANR-20-CE47-0005, Young Researchers (JCJC) project QRand] and from the Austrian Science Foundation (FWF, P 32597 N). The work of V.V. was partly supported by the ERC under Grant No. 758329 “Atomic Gauge and Entanglement Theories” (AGEnTh), and by the Ministero dell’Istruzione e del Merito (MIUR) Program “Framework per L’Attrazione e il Rafforzamento delle Eccellenze per la Ricerca in Italia” (FARE) (MEPH). J.D. acknowledges support from the ANR (ANR-20-CE30-0017-02, project QuaDy) and from the CNRS International Emerging Actions (IEA) (project QuDOD). For our numerical simulations, we used the quantum toolbox QuTiP [116].

APPENDIX A: ENTANGLEMENT CONDITIONS

In this appendix, we derive our rigorous conditions to detect OE in bipartite mixed states ρ_{AB} . The starting point is the operator Schmidt decomposition

$$\frac{\rho_{AB}}{\sqrt{\text{Tr}[\rho_{AB}^2]}} = \sum_{i=1}^R \lambda_i O_{A,i} \otimes O_{B,i} \quad (\text{A1})$$

[see also Eq. (1)]. Here, $R \geq 1$ denotes the operator Schmidt rank and the Schmidt values $\lambda_1, \dots, \lambda_R$ are non-negative ($\lambda_i \geq 0$) and obey $\sum_{i=1}^R \lambda_i^2 = 1$. A seminal result in entanglement theory states that the Schmidt values of any separable state ρ_{AB} must obey

$$\sum_{i=1}^R \lambda_i \leq 1/\sqrt{\text{Tr}(\rho_{AB}^2)} \quad (\text{A2})$$

[see, e.g., Ref. [33, Theorem 6] and also Eq. (6)]. Conversely, if Eq. (A2) is violated, then ρ_{AB} must be entangled (across the bipartition into subsystems A and B). This entanglement criterion is called the computable cross-norm or realignment (CCNR) condition and applies to any type of bipartite state. Also, other conditions based on realignment moments have been introduced in Ref. [117]. The main drawback of the CCNR criterion is that it seems to rely on the explicit availability of an operator Schmidt decomposition in Eq. (A1). Obtaining such a decomposition requires full state tomography of the density matrix ρ_{AB} . This apparent drawback has recently been overcome in Ref. [65]. There, the authors point out that sums of higher powers of Schmidt values can be reformulated in terms of linear observables in tensor products of the original density matrix ρ_{AB} . This can be achieved by concatenating subsystem swap operators. Let $\mathbb{S}_{k,l}^{(X)}$ be the operator that swaps the k th and l th copies of system X ($X = A, B$, or AB below). Namely, it acts as $\mathbb{S}_{k,l}^{(X)}(|i\rangle^{X_k} \otimes |j\rangle^{X_l}) = |j\rangle^{X_k} \otimes |i\rangle^{X_l}$ on any pair of basis states for systems X_k and X_l (as indicated by the superscripts) and as the identity on all other systems. Then, the following relation holds:

$$\sum_{i=1}^R \lambda_i^4 = \frac{\text{Tr}(\mathcal{S}\rho_{AB}^{\otimes 4})}{\text{Tr}(\rho_{AB}^2)^2} \quad \text{where} \quad \mathcal{S} = \mathbb{S}_{1,4}^{(A)} \otimes \mathbb{S}_{2,3}^{(A)} \otimes \mathbb{S}_{1,2}^{(B)} \otimes \mathbb{S}_{3,4}^{(B)}. \quad (\text{A3})$$

The denominator $\text{Tr}(\rho_{AB}^2)^2$ is a consequence of the normalization in the left-hand side of Eq. (A1) and validity of the overall expression readily follows from inserting the operator Schmidt decomposition into the right-hand side of Eq. (A3) and from using the fact that the operators $O_{A,i}$ and $O_{B,i}$ are all orthonormal, i.e., $\text{Tr}(O_{A,i}O_{A,j}) = \text{Tr}(O_{B,i}O_{B,j}) = \delta_{ij}$. It is also worth pointing out that the purity can also be reformulated as a linear observable on tensor products:

$$\text{Tr}(\rho_{AB}^2) = \text{Tr}\left(\mathbb{S}_{1,2}^{(AB)}\rho_{AB}^{\otimes 2}\right). \quad (\text{A4})$$

This is relevant because trace polynomials of the form $\text{Tr}(O^{(n)}\rho_{AB}^{\otimes n})$ can be measured directly in actual experiments by employing techniques from the randomized-measurement toolbox [48]. This is the content of Appendix B. For now, it is enough to recall that we know how to directly estimate the left-hand side of Eq. (A3), while we are not aware of a direct estimation protocol for the left-hand side of Eq. (A2).

So, how do we overcome this discrepancy between what can be measured [Eq. (A3)] and what is required to detect entanglement [violation of Eq. (A2)]? We collect the positive Schmidt values into an R -dimensional vector $l = (\lambda_1, \dots, \lambda_R)$ and use fundamental ℓ_p -norm relations to obtain a relation between $\|v\|_{\ell_1} = \sum_{i=1}^R |\lambda_i| = \sum_{i=1}^R \lambda_i$ (the last equation uses the fact that all Schmidt values are non-negative) and $\|v\|_{\ell_4}^4 = \sum_{i=1}^R \lambda_i^4$. To achieve such a conversion, we can also use the fact that Schmidt values are normalized, i.e., $\|v\|_{\ell_2}^2 = \sum_{i=1}^R \lambda_i^2 = 1$. We can use the Berger inequality [118], which relates the ℓ_1 , ℓ_2 , and ℓ_4 norms of any vector. This inequality then ensures that

$$\sum_{i=1}^R \lambda_i = \|v\|_{\ell_1} \geq \frac{\|v\|_{\ell_2}^3}{\|v\|_{\ell_4}^2} = \frac{1}{\left(\sum_{i=1}^R \lambda_i^4\right)^{1/2}}. \quad (\text{A5})$$

This relation is a simple consequence of Hölder's inequality and we refer to Ref. [119, Proof of Lemma 12] for a quick derivation.

We now have all the ingredients in place to derive our experimentally accessible entanglement condition. A combination of Eqs. (A2), (A5), and (A3) implies that *every* separable state ρ_{AB} must obey

$$\frac{1}{\text{Tr}(\rho_{AB}^2)} \geq \left(\sum_{i=1}^R \lambda_i\right)^2 \geq \frac{1}{\sum_{i=1}^R \lambda_i^4} = \frac{\text{Tr}(\rho_{AB}^2)^2}{\text{Tr}(\mathcal{S}\rho_{AB}^{\otimes 4})} \quad (\text{A6})$$

or, equivalently,

$$\text{Tr}\left(\mathbb{S}_{1,4}^{(A)} \otimes \mathbb{S}_{2,3}^{(A)} \otimes \mathbb{S}_{1,2}^{(B)} \otimes \mathbb{S}_{3,4}^{(B)}\rho_{AB}^{\otimes 4}\right) = \text{Tr}(\mathcal{S}\rho_{AB}^{\otimes 4}) \geq \text{Tr}(\rho_{AB}^2)^3 = \text{Tr}\left(\mathbb{S}_{1,2}^{(AB)}\rho_{AB}^{\otimes 2}\right)^3. \quad (\text{A7})$$

If this relation is violated, then we can be sure that the state ρ_{AB} must be entangled. From Eq. (A6), we can also take logarithms and negate the sign to obtain an equivalent statement in terms of Rényi entropies. We now formally propose our entanglement condition, which—in stark contrast to the original CCNR condition—is directly accessible in an experiment.

Proposition 1 (Entanglement condition): Let ρ_{AB} be a bipartite quantum state with Rényi 2-OE $S^{(2)}(\rho_{AB}) = -\log(\sum_i \lambda_i^4)$ and Rényi 2-entropy $R^{(2)}(\rho_{AB}) = -\log(\text{Tr}(\rho_{AB}^2))$. Then, the relation

$$S^{(2)}(\rho_{AB}) > R^{(2)}(\rho_{AB}) \quad (\text{A8})$$

implies that ρ_{AB} must be entangled (across the bipartition A vs B).

As our criterion here is derived from the CCNR criterion of Eq. (6), we note that if Eq. (7) is violated, then Eq. (6) is also necessarily violated (and both violations then certify entanglement in the state ρ_{AB}). Conversely, Eq. (7) can be satisfied while the CCNR criterion in Eq. (6) is violated (so that only the latter can certify entanglement). In this case, detection of such entangled states is missed by our derived criterion.

Finally, we point out that a centering operation on the level of density matrices can substantially enhance the ability to detect entanglement. The key idea is to shift the original density matrix by

$$\rho_{AB} \mapsto \rho_{AB} - \rho_A \otimes \rho_B = X_{AB}, \quad (\text{A9})$$

where $\rho_A = \text{Tr}_B(\rho_{AB})$ and $\rho_B = \text{Tr}_A(\rho_{AB})$ are the reduced density matrices of ρ_{AB} . Note that this centered density matrix X_{AB} is not physical, because it has negative eigenvalues and a vanishing trace. The Schmidt coefficients $(\chi_1, \dots, \chi_{R'})$ of this shifted density matrix are known to obey the *enhanced realignment and computable cross-norm condition* [120,121]:

$$\sum_{i=1}^{R'} \chi_i \leq \frac{\sqrt{1 - \text{Tr}(\rho_A^2)} \sqrt{1 - \text{Tr}(\rho_B^2)}}{\sqrt{\text{Tr}([X_{AB}]^2)}} \quad (\text{A10})$$

(see, e.g., Ref. [65]). We can now adjust the arguments from before to obtain the following relation, which must hold for every shifted version X_{AB} of a separable state ρ_{AB} :

$$\text{Tr}(S X_{AB}^{\otimes 4}) \geq \frac{\text{Tr}(X_{AB}^2)^3}{(1 - \text{Tr}(\rho_A^2))(1 - \text{Tr}(\rho_B^2))}. \quad (\text{A11})$$

If this condition is violated, the underlying state must be entangled. Although it requires some additional work, the expressions on both sides of this equation can be reexpressed in terms of linear observables in tensor products of ρ_{AB} , which makes them experimentally accessible.

Moreover, entanglement conditions based on realignment moments have been introduced in Ref. [117]. Finally, let us point out that the idea of using linear observables in tensor products—which are also known as index permutation matrices in this context—to detect entanglement is not new. Specifically connected to this work, optimal entanglement detection criteria have already been found in this framework [65]. Here, we provide additional criteria that are perhaps less powerful but simpler to state, simpler to estimate, and that follow from a simpler proof argument. In Fig. 4, with the batch-shadow estimators, we illustrate an example of mixed-state-entanglement detection from the experimental data of Ref. [7] using Proposition 1 and the optimal condition in Eq. (7) of Ref. [65], where we clearly observe an enhanced detection capability of the optimal condition. We additionally note that with the finite-measurement statistics available from the experiment of Ref. [7], we are unable to extract experimentally the enhanced condition derived in Eq. (A11) and its corresponding optimal condition [65, Eq. (8)], due to large error bars on the experimental data arising from the finite available measurement statistics.

APPENDIX B: SYMMETRY RESOLUTION OF OPERATOR SCHMIDT DECOMPOSITION

In this appendix, we provide a proof of Eqs. (9)–(10). We start by showing the symmetry resolution of the Schmidt decomposition for a pure state $|\psi\rangle \in \mathcal{H} = \mathcal{H}_A \otimes \mathcal{H}_B$, which is an eigenstate of an additive charge $Q = Q_A + Q_B$ in Appendix B 1. This is equivalent to showing that the reduced density matrix $\rho_A = \text{Tr}_B|\psi\rangle\langle\psi|$ admits a block-diagonal structure with respect to the eigensubspaces of Q_A [67], which we prove in Appendix B 2. In Appendixes B 3 and B 4, we repeat the same arguments for a generic operator O , showing that the decomposition in Eq. (9) is possible. In Appendix B 5, we give a simple example of symmetry resolution of an operator for the density matrix of a three-qubit system.

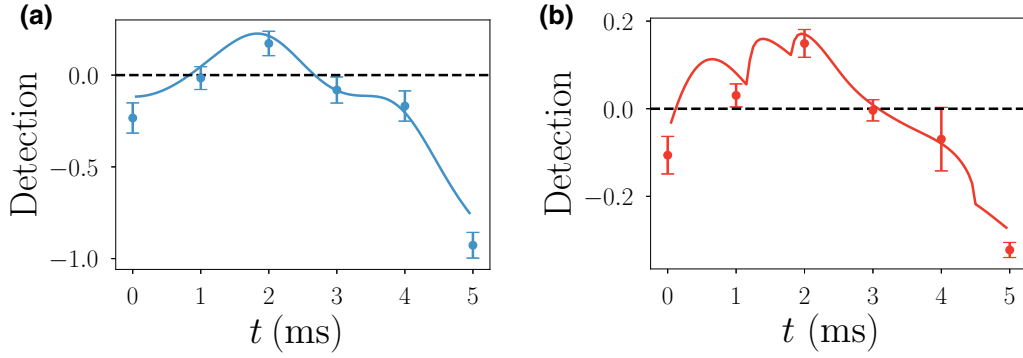


FIG. 4. Entanglement detection. We consider a reduced density matrix ρ_{AB} defined on the subsystem $A = [1, 2]$ and $B = [3, 4]$ for the 10-ion experiment of Ref. [7]. In (a), we plot as detection on the vertical axis, the condition given in Proposition 1, $(S^{(2)}(\rho_{AB}) - R^{(2)}(\rho_{AB}))$ and, similarly, in (b) we use the optimal condition in Eq. (7) of Ref. [65] $(E_{2n}^\pi(\rho_{AB}) - 1)$. We detect entanglement between the partitions A and B for various times t during the quench dynamics when we observe values greater than 0. The points show experimental results with the error bars calculated using jackknife resampling. The solid lines correspond to numerical simulations of the unitary dynamics, including dissipation.

1. Symmetry-resolved Schmidt decomposition of a pure state

Let $|\psi\rangle \in \mathcal{H} = \mathcal{H}_A \otimes \mathcal{H}_B$ be a state that satisfies

$$(Q_A + Q_B)|\psi\rangle = 0, \quad (\text{B1})$$

for Hermitian operators Q_A and Q_B acting on $\mathcal{H}_A, \mathcal{H}_B$.

Proposition 2: *There exists a symmetry-resolved Schmidt decomposition*

$$|\psi\rangle = \sum_q \sum_j \lambda_j^{(q)} |\psi_{A_j}^{(q)}\rangle |\psi_{B_j}^{(-q)}\rangle, \quad (\text{B2})$$

with $\langle \psi_{A_j}^{(q)} | \psi_{A_{j'}}^{(q')} \rangle = \delta_{q,q'} \delta_{j,j'}$, $\langle \psi_{B_j}^{(q)} | \psi_{B_{j'}}^{(q')} \rangle = \delta_{q,q'} \delta_{j,j'}$, and

$$Q_A |\psi_{A_j}^{(q)}\rangle = q |\psi_{A_j}^{(q)}\rangle, \quad Q_B |\psi_{B_j}^{(q)}\rangle = q |\psi_{B_j}^{(q)}\rangle. \quad (\text{B3})$$

Proof. \mathcal{H}_A can be decomposed into eigenspaces of Q_A : $\mathcal{H}_A = \bigoplus_q \mathcal{H}_A^{(q)}$, where the q values are the eigenvalues of Q_A . We pick an orthonormal basis for each $\mathcal{H}_A^{(q)}$: $\{|e_{A,1}^{(q)}\rangle, |e_{A,2}^{(q)}\rangle, \dots\rangle$. Note that if $q \neq q'$, then $\langle e_{A,i}^{(q)} | e_{A,j}^{(q')} \rangle = 0$. This is because Q_A is Hermitian, so $q \langle e_{A,i}^{(q)} | e_{A,j}^{(q')} \rangle = \langle e_{A,i}^{(q)} | Q | e_{A,j}^{(q')} \rangle = q' \langle e_{A,i}^{(q)} | e_{A,j}^{(q')} \rangle$. Thus, the basis vectors of different eigenspaces are orthogonal and we can use all of them together as an orthonormal basis that spans the total space \mathcal{H}_A . Similarly, one can pick a basis for \mathcal{H}_B such that every basis vector is an eigenstate of Q_B .

Any state $|\psi\rangle \in \mathcal{H} = \mathcal{H}_A \otimes \mathcal{H}_B$ can be written in the form

$$|\psi\rangle = \sum_q \sum_j \sum_{q'} \sum_{j'} M_{j,j'}^{(q,q')} |e_{A_j}^{(q)}\rangle \otimes |e_{B_{j'}}^{(q')}\rangle, \quad (\text{B4})$$

with some components $M_{j,j'}^{(q,q')}$. If $|\psi\rangle$ satisfies Eq. (B1), then

$$0 = (Q_A + Q_B)|\psi\rangle = \sum_q \sum_j \sum_{q'} \sum_{j'} (q + q') M_{j,j'}^{(q,q')} |e_{A_j}^{(q)}\rangle \otimes |e_{B_{j'}}^{(q')}\rangle \quad (\text{B5})$$

and linear independence of the basis vectors implies

$$M_{j,j'}^{(q,q')} = 0 \quad \text{if} \quad q + q' \neq 0. \quad (\text{B6})$$

Thus, for a state $|\psi\rangle$ that satisfies Eq. (B1),

$$|\psi\rangle = \sum_q \sum_j \sum_{j'} M_{jj'}^{(q,-q)} |e_{Aj}^{(q)}\rangle \otimes |e_{Bj'}^{(-q)}\rangle. \quad (\text{B7})$$

Then, we can treat the different q blocks separately. For every q , we take a Schmidt decomposition of the state

$$\sum_j \sum_{j'} M_{jj'}^{(q,-q)} |e_{Aj}^{(q)}\rangle \otimes |e_{Bj'}^{(-q)}\rangle = \sum_j \lambda_j^{(q)} |\psi_{Aj}^{(q)}\rangle \otimes |\psi_{Bj}^{(-q)}\rangle \quad (\text{B8})$$

and putting all these together, we obtain the *symmetry-resolved Schmidt decomposition* in Eq. (B2). \blacksquare

2. Block-diagonal form of the reduced density matrix

We now prove the block-diagonal structure of the reduced density matrix, which is equivalent to the symmetry-resolved Schmidt decomposition for the evaluation of the entanglement in the charge sectors [67]. As before, let $|\psi\rangle \in \mathcal{H} = \mathcal{H}_A \otimes \mathcal{H}_B$ be a state that satisfies

$$(Q_A + Q_B) |\psi\rangle = 0, \quad (\text{B9})$$

for Hermitian operators Q_A and Q_B acting on $\mathcal{H}_A, \mathcal{H}_B$.

Proposition 3: *The reduced density matrix $\rho_A = \text{Tr}_B |\psi\rangle\langle\psi|$ commutes with Q_A .*

Proof. We note that

$$\begin{aligned} [Q_A, \text{Tr}_B |\psi\rangle\langle\psi|] &= \text{Tr}_B ([Q_A, |\psi\rangle\langle\psi|]) \\ &= \text{Tr}_B ([Q_A + Q_B, |\psi\rangle\langle\psi|] - [Q_B, |\psi\rangle\langle\psi|]) \\ &= -\text{Tr}_B (Q_B |\psi\rangle\langle\psi|) + \text{Tr}_B (|\psi\rangle\langle\psi| Q_B) \end{aligned} \quad (\text{B10})$$

and this vanishes because of the cyclicity of the trace. \blacksquare

We can thus write an eigenvalue decomposition for the reduced density matrix with blocks labeled by the charges q of Q_A . This leads to the same Schmidt decomposition as in Eq. (B2).

3. Symmetry-resolved operator Schmidt decomposition

What has been done so far for the state $|\psi\rangle$ can be generalized to operators. In particular, let $O \in \text{End}(\mathcal{H}) = \text{End}(\mathcal{H}_A) \otimes \text{End}(\mathcal{H}_B)$ be an operator that satisfies

$$[Q_A + Q_B, O] = 0, \quad (\text{B11})$$

for Hermitian operators Q_A and Q_B .

Proposition 4: *There exists a symmetry-resolved operator Schmidt decomposition*

$$\frac{O}{\sqrt{\text{Tr}(O^\dagger O)}} = \sum_q \sum_j \lambda_j^{(q)} O_{Aj}^{(q)} \otimes O_{Bj}^{(-q)}, \quad (\text{B12})$$

with $\text{Tr}(O_{Aj}^{(q)\dagger} O_{Aj'}^{(q')}) = \delta_{q,q'} \delta_{j,j'}$, $\text{Tr}(O_{Bj}^{(q)\dagger} O_{Bj'}^{(q')}) = \delta_{q,q'} \delta_{j,j'}$, and

$$[Q_A, O_{Aj}^{(q)}] = q O_{Aj}^{(q)}, \quad [Q_B, O_{Bj}^{(q)}] = q O_{Bj}^{(q)}. \quad (\text{B13})$$

Proof. This is exactly the same statement as above, with \mathcal{H}_A replaced by $\text{End}(\mathcal{H}_A)$ equipped with the Hilbert-Schmidt inner product. To be more explicit, $\text{End}(\mathcal{H}_A)$ can be decomposed into eigenspaces of the commutator $[Q_A, \cdot]$: $\text{End}(\mathcal{H}_A) = \bigoplus_q \text{End}(\mathcal{H}_A^{(q)})$, where the q values are the eigenvalues of $[Q_A, \cdot]$. We pick an orthonormal basis of $\text{End}(\mathcal{H}_A^{(q)})$: $\{E_{A,1}^{(q)}, E_{A,2}^{(q)}, \dots\}$. As above, we can combine all these basis vectors with different q values into a basis for the total Hilbert space $\text{End}(\mathcal{H}_A)$. We do the same for part B .

The operator $O \in \text{End}(\mathcal{H})$ can then be written in that basis, with some components $M_{j,j'}^{(q,q')}$,

$$\frac{O}{\sqrt{\text{Tr}(O^\dagger O)}} = \sum_q \sum_j \sum_{q'} \sum_{j'} M_{j,j'}^{(q,q')} E_{A,j}^{(q)} \otimes E_{B,j'}^{(q')}, \quad (\text{B14})$$

where, by definition,

$$[Q_A, E_{A,j}^{(q)}] = q E_{A,j}^{(q)}, \quad [Q_B, E_{B,j'}^{(q')}] = q' E_{B,j'}^{(q')}. \quad (\text{B15})$$

If O satisfies Eq. (B11), then

$$M_{j,j'}^{(q,q')} = 0 \quad \text{if} \quad q + q' \neq 0, \quad (\text{B16})$$

for the same reason as above. Again, the q blocks can be separately Schmidt decomposed and this leads to Eq. (B12). ■

4. Block-diagonal form of the super-reduced density matrix

Let $O \in \text{End}(\mathcal{H}) = \text{End}(\mathcal{H}_A) \otimes \text{End}(\mathcal{H}_B)$ be an operator that satisfies

$$[Q_A + Q_B, O] = 0, \quad (\text{B17})$$

for Hermitian operators Q_A and Q_B .

Proposition 5: *The super-reduced density matrix $\text{Tr}_{B \otimes B}(|O\rangle\langle O|)$ commutes with the supercharge $Q_A = Q_A \otimes 1 - 1 \otimes Q_A^T$.*

Proof. We note that

$$\begin{aligned} [Q_A, \text{Tr}_{B \otimes B} |O\rangle\langle O|] &= \text{Tr}_{B \otimes B}([Q_A, |O\rangle\langle O|]) \\ &= \text{Tr}_{B \otimes B}([Q_A + Q_B, |O\rangle\langle O|] - [Q_B, |O\rangle\langle O|]) \\ &= -\text{Tr}_{B \otimes B}(Q_B |O\rangle\langle O|) + \text{Tr}_{B \otimes B}(|O\rangle\langle O| Q_B) \end{aligned} \quad (\text{B18})$$

and this vanishes because of the cyclicity of the trace. ■

We can thus write an eigenvalue decomposition for the super-reduced density matrix with blocks labeled by the charges q of Q_A . This leads to the same Schmidt decomposition as in Eq. (B12).

5. Three-qubit example

To get familiar with the symmetry resolution of an operator, let us look at a minimal illustrative example: a three-qubit system, the qubits of which are labeled A , B , and C , in a state of the form ($|\alpha|^2 + |\beta|^2 + |\gamma|^2 = 1$)

$$|\psi\rangle_{ABC} = \alpha |100\rangle + \beta |010\rangle + \gamma |001\rangle. \quad (\text{B19})$$

This is an eigenstate of the total charge operator $Q_{ABC} = \sum_{j=A,B,C} Q_j$ with $Q_j = |1\rangle\langle 1|$. The reduced density matrix of the subsystem AB is

$$\rho_{AB} = (\alpha |10\rangle + \beta |01\rangle) (\alpha^* \langle 10| + \beta^* \langle 01|) + |\gamma|^2 |00\rangle\langle 00|, \quad (\text{B20})$$

which commutes with $Q_A + Q_B$. Therefore the definitions introduced in the main text can be used and it makes sense to study the SROE of the reduced density matrix ρ_{AB} in this minimal example.

Let us proceed by vectorizing the reduced density matrix ρ_{AB} :

$$|\rho_{AB}\rangle = |\gamma|^2 |00\rangle_A |00\rangle_B + |\beta|^2 |00\rangle_A |11\rangle_B + |\alpha|^2 |11\rangle_A |00\rangle_B + \alpha^* \beta |01\rangle_A |10\rangle_B + \alpha \beta^* |10\rangle_A |01\rangle_B. \quad (\text{B21})$$

From this, we can build the object $|\rho_{AB}\rangle \langle \rho_{AB}|$ and take the trace over the subsystem B . This gives

$$\begin{aligned} \text{Tr}_B |\rho_{AB}\rangle \langle \rho_{AB}| &= |\beta|^4 |00\rangle \langle 00| + |\alpha|^2 |\beta|^2 (|01\rangle \langle 01| + |10\rangle \langle 10|) \\ &\quad + (|\gamma|^2 |00\rangle + |\alpha|^2 |11\rangle)(|\gamma|^2 \langle 00| + |\alpha|^2 \langle 11|). \end{aligned} \quad (\text{B22})$$

By reshuffling the elements of the basis, we find that the matrix has a block-diagonal decomposition as

$$\text{Tr}_B |\rho_{AB}\rangle \langle \rho_{AB}| = (|\alpha|^2 |\beta|^2)_{q=1} \oplus (|\alpha|^2 |\beta|^2)_{q=-1} \oplus \begin{pmatrix} |\beta|^4 + |\gamma|^4 & |\alpha|^2 |\gamma|^2 \\ |\alpha|^2 |\gamma|^2 & |\alpha|^4 \end{pmatrix}_{q=0}, \quad (\text{B23})$$

where each block lives in the eigensubspace of the supercharge operator $\mathcal{Q}_A = \mathcal{Q}_A \otimes \mathbb{1} - \mathbb{1} \otimes \mathcal{Q}_A^T$ (with the corresponding eigenvalues indicated as subscripts).

From this, we can treat each block separately, as in the proofs of Propositions 2 or 4 above. We thus obtain the following ‘‘symmetry-resolved operator Schmidt decomposition’’:

$$\frac{\rho_{AB}}{\sqrt{\text{Tr}[\rho_{AB}^2]}} = \lambda^{(1)} O_A^{(1)} \otimes O_B^{(-1)} + \lambda^{(-1)} O_A^{(-1)} \otimes O_B^{(1)} + \sum_{j=1,2} \lambda_j^{(0)} O_{A,j}^{(0)} \otimes O_{B,j}^{(0)}, \quad (\text{B24})$$

where the Schmidt coefficients $\lambda_j^{(q)}$ are given by

$$\lambda^{(1)} = \lambda^{(-1)} = \frac{1}{2} \sqrt{\chi}, \quad \lambda_j^{(0)} = \frac{1}{2} (1 \pm \sqrt{1 - \chi}) \quad (\text{B25})$$

with $\chi = (4|\alpha|^2 |\beta|^2) / (\text{Tr}[\rho_{AB}^2])$, $\text{Tr}[\rho_{AB}^2] = (|\alpha|^2 + |\beta|^2)^2 + |\gamma|^4$, and the operators $O_{A,j}^{(q)}$ and $O_{B,j}^{(q)}$, which form orthonormal sets, read

$$\begin{aligned} O_A^{(1)} &= |1\rangle \langle 0|_A, & O_B^{(-1)} &= |0\rangle \langle 1|_B, \\ O_A^{(-1)} &= |0\rangle \langle 1|_A, & O_B^{(1)} &= |1\rangle \langle 0|_B, \\ O_{A,1}^{(0)} &= a_+ |0\rangle \langle 0|_A + a_- |1\rangle \langle 1|_A, & O_{B,1}^{(0)} &= b_+ |0\rangle \langle 0|_B + b_- |1\rangle \langle 1|_B, \\ O_{A,2}^{(0)} &= a_- |0\rangle \langle 0|_A - a_+ |1\rangle \langle 1|_A, & O_{B,2}^{(0)} &= -b_- |0\rangle \langle 0|_B + b_+ |1\rangle \langle 1|_B, \end{aligned} \quad (\text{B26})$$

for some real parameters a_{\pm} and b_{\pm} that are functions of $|\alpha|$, $|\beta|$, and $|\gamma|$ (which can be obtained explicitly but are rather tedious to write).

As a more specific example, if we fix the parameters in Eq. (B19) as, for instance, $\alpha = \sqrt{5/12}$, $\beta = 1/2$, $\gamma = 1/\sqrt{3}$, then the coefficients $\lambda_j^{(q)}$, a_{\pm} , and b_{\pm} introduced above are found to be

$$\begin{aligned} \lambda^{(1)} = \lambda^{(-1)} &= \frac{\sqrt{3}}{4}, & \lambda_1^{(0)} &= \frac{3}{4}, & \lambda_2^{(0)} &= \frac{1}{4}, \\ a_+ = a_- &= \frac{1}{\sqrt{2}}, & b_+ &= \frac{3}{\sqrt{10}}, & b_- &= \frac{1}{\sqrt{10}}. \end{aligned} \quad (\text{B27})$$

From Eq. (B27), we then obtain the following expressions for the OE,

$$S(\rho_{AB}) = 4 \log 2 - \frac{3}{2} \log 3, \quad (\text{B28})$$

and the SROE,

$$S_{\pm 1}(\rho_{AB}) = 0, \quad S_0(\rho_{AB}) = \log 10 - \frac{9}{5} \log 3, \quad (\text{B29})$$

and we can check that Eq. (13) is indeed satisfied.

To finish with this example, let us comment on the non-Hermiticity of the operators $O_{A/B}^{(\pm 1)}$ introduced in Eq. (B26). As mentioned in the main text, in general it is always possible to impose that the operators $O_{A/B,i}$ that enter the standard Schmidt decomposition, given in Eqs. (1) or (2), of a Hermitian operator must be Hermitian themselves. However, this can no longer be ensured when imposing the symmetry-resolved form of the Schmidt decomposition, as in Eqs. (9)–(10).

To see this, recall that while the Schmidt coefficients are unique, the operators that are used in the standard (non-symmetry-resolved) decomposition are not: they are only unique—up to some complementary phases (or up to a sign if one wants them to be Hermitian)—when the corresponding Schmidt coefficient has multiplicity one. For instance, in our above example, the operators $O_{A/B,j}^{(0)}$, corresponding to the different Schmidt coefficients $\lambda_j^{(0)}$, are unique (up to a phase or a sign) but there remains some freedom, in a standard Schmidt decomposition, for the choice of operators $O_{A/B}^{(\pm 1)}$ corresponding to the multiplicity-2 Schmidt coefficients $\lambda^{(1)} = \lambda^{(-1)}$.

In fact, one finds that the most general form of the non-symmetry-resolved Schmidt decomposition of ρ_{AB} above would be as in Eq. (B24) but with $O_{A/B}^{(\pm 1)}$ from Eq. (B26) replaced by

$$\begin{aligned} O_A^{(1)} &= \mu |1\rangle \langle 0|_A + \nu |0\rangle \langle 1|_A, & O_B^{(-1)} &= \nu^* |1\rangle \langle 0|_B + \mu^* |0\rangle \langle 1|_B, \\ O_A^{(-1)} &= e^{i\varphi} (-\nu^* |1\rangle \langle 0|_A + \mu^* |0\rangle \langle 1|_A), & O_B^{(1)} &= e^{-i\varphi} (\mu |1\rangle \langle 0|_B - \nu |0\rangle \langle 1|_B), \end{aligned} \quad (\text{B30})$$

for some complex coefficients μ and ν such that $|\mu|^2 + |\nu|^2 = 1$ and some phase φ (and, for full generality, replacing $O_{A,j}^{(0)}$ and $O_{B,j}^{(0)}$ by $e^{i\varphi_j} O_{A,j}^{(0)}$ and $e^{-i\varphi_j} O_{B,j}^{(0)}$, respectively, for some phases φ_j). It is easily seen that these operators can indeed be chosen to be Hermitian, by taking, e.g., $\mu = \nu = 1/\sqrt{2}$ and $\varphi = \pi/2$. However, imposing the condition that the Schmidt decomposition is symmetry resolving, i.e., that the above operators satisfy Eq. (10), turns out to be incompatible with these being Hermitian: e.g., $[Q_A, O_A^{(1)}] = O_A^{(1)}$ requires $|\mu| = 1, \nu = 0$ [as in Eq. (B26)].

One may note, for completeness, that Eq. (10) can actually be satisfied by Hermitian operators $O_{A,j}^{(q)}, O_{A,j}^{(q)}$ only in the case where $q = 0$: indeed, assuming that $O_{A,j}^{(q)} = (O_{A,j}^{(q)})^\dagger$, Eq. (10) then implies (using the cyclicity of the trace) $\text{Tr}([Q_A, O_{A,j}^{(q)}] O_{A,j}^{(q)}) = 0 = q \text{Tr}((O_{A,j}^{(q)})^\dagger O_{A,j}^{(q)}) = q$.

APPENDIX C: THE BATCH-SHADOW RANDOMIZED-MEASUREMENT TOOLBOX

1. Classical shadows with local CUE and Pauli measurements

Given an N -qubit state prepared on a quantum device, we can construct a Haar classical shadow $\hat{\rho}^{(r)}$ (equivalently called a Haar shadow) of the state defined in Eq. (17) (with $N_M = 1$) [49]:

$$\hat{\rho}^{(r)} = \bigotimes_{i=1}^N \left(3(u_i^{(r)})^\dagger |s_i^{(r)}\rangle \langle s_i^{(r)}| u_i^{(r)} - \mathbb{I}_2 \right), \quad (\text{C1})$$

where the applied local random unitary is sampled from the CUE or, equivalently, from the Haar measure (local CUE measurements). Alternatively, we could consider random single-qubit operations that, equivalently, lead to measuring each qubit in one of the random Pauli bases of \mathcal{X}, \mathcal{Y} or \mathcal{Z} (local Pauli measurements). These lead to six possible states that can be succinctly summarized as follows:

$$|\mathcal{B}, s\rangle \quad \text{with} \quad \mathcal{B} \in \{\mathcal{X}, \mathcal{Y}, \mathcal{Z}\}, \quad s \in \{\pm\}. \quad (\text{C2})$$

More precisely, these states correspond to the following six possibilities:

$$|0\rangle = |\mathcal{Z}, +\rangle, \quad |1\rangle = |\mathcal{Z}, -\rangle, \quad |+\rangle = |\mathcal{X}, +\rangle, \quad |-\rangle = |\mathcal{X}, -\rangle, \quad |i+\rangle = |\mathcal{Y}, +\rangle, \quad |i-\rangle = |\mathcal{Y}, -\rangle. \quad (\text{C3})$$

To construct a Pauli shadow $\hat{\rho}$, we choose randomly and uniformly, for each single qubit i , a basis \mathcal{B}_i in \mathcal{X}, \mathcal{Y} or \mathcal{Z} that is subsequently followed by the resulting basis measurement that provides a string of signs $\mathbf{s} = (s_1, \dots, s_N) \in \{\pm\}$. With this information and defining N chosen bases $\mathcal{B} = (\mathcal{B}_1, \dots, \mathcal{B}_N)$, we can provide an unbiased estimator of the density

matrix ρ as [122]:

$$\hat{\rho}(\mathcal{B}, \mathbf{s}) = \bigotimes_{i=1}^N \left(3 |\mathcal{B}_i, s_i\rangle \langle \mathcal{B}_i, s_i| - \mathbb{I}_2 \right) \quad \text{such that} \quad \mathbb{E}[\hat{\rho}(\mathcal{B}, \mathbf{s})] = \rho. \quad (\text{C4})$$

Here, \mathbb{E} denotes the expectation value over the uniformly sampled random bases, as well as the resulting measurement outcomes. Note that the single-qubit Pauli shadows have some interesting properties due to the fact that their chosen measurement bases are mutually unbiased.

For $\mathcal{B} \neq \mathcal{B}'$, we have

$$\text{Tr} \left[(3 |\mathcal{B}, s\rangle \langle \mathcal{B}, s| - \mathbb{I}_2) (3 |\mathcal{B}', s'\rangle \langle \mathcal{B}', s'| - \mathbb{I}_2) \right] = \frac{1}{2} \quad \forall s, s' \in \{\pm\} \quad (\text{C5})$$

and for $\mathcal{B} = \mathcal{B}'$ we have

$$\text{Tr} \left[(3 |\mathcal{B}, s\rangle \langle \mathcal{B}, s| - \mathbb{I}_2) (3 |\mathcal{B}', s'\rangle \langle \mathcal{B}', s'| - \mathbb{I}_2) \right] = \begin{cases} -4, & \text{if } s \neq s', \\ 5, & \text{if } s = s'. \end{cases} \quad (\text{C6})$$

This rich geometric structure allows us to deduce streamlined upper bounds on the trace overlap between different Pauli shadows.

Lemma 1: *Given two N -qubit basis strings $\mathcal{B}, \mathcal{B}' \in \{\mathcal{X}, \mathcal{Y}, \mathcal{Z}\}^{\times N}$, for any sign of the outcome strings $s, s' \in \{\pm\}^{\times N}$, the following two statements hold:*

$$\text{Tr} \left(\hat{\rho}(\mathcal{B}, \mathbf{s}) \hat{\rho}'(\mathcal{B}', \mathbf{s}') \right)^2 \leq \prod_{i=1}^N \left(5^2 \mathbf{I}\{\mathcal{B}_i = \mathcal{B}'_i\} + \left(\frac{1}{2}\right)^2 \mathbf{I}\{\mathcal{B}_i \neq \mathcal{B}'_i\} \right) \quad (\text{C7})$$

and

$$\mathbb{E} \left[\prod_{i=1}^N \left(5^2 \mathbf{I}\{\mathcal{B}_i = \mathcal{B}'_i\} + \left(\frac{1}{2}\right)^2 \mathbf{I}\{\mathcal{B}_i \neq \mathcal{B}'_i\} \right) \right] = 8.5^N, \quad (\text{C8})$$

where $\mathbf{I}\{\mathcal{B}_i = \mathcal{B}'_i\}$ and $\mathbf{I}\{\mathcal{B}_i \neq \mathcal{B}'_i\}$ denote the indicator functions of the advertised events.

The proof strategy for this auxiliary statement is inspired by a recent analysis of classical shadows for single-qubit symmetric informationally complete (SIC) positive operator-valued measures (POVMs) (see Ref. [123, Appendix IX.B]).

Proof. The proof of the first inequality follows from the observation that the single-qubit states $|\mathcal{B}_i, s_i\rangle$ and $|\mathcal{B}'_i, s'_i\rangle$ are mutually unbiased whenever $\mathcal{B}_i \neq \mathcal{B}'_i$. If two bases coincide ($\mathcal{B}_i = \mathcal{B}'_i$), the squared overlap either contributes $(-4)^2$ ($s' \neq s$) or 5^2 ($s = s'$) and can be bounded by choosing the larger term from amongst them. Equation (C7) now follows from applying this single-qubit argument to each contribution in the N -fold tensor product that makes up the two shadows, as the trace inner product of two shadows factorizes into N single-qubit contributions from Eq. (C4).

Second, noting that all random basis choices are independent, we can develop Eq. (C8) as

$$\mathbb{E} \left[\prod_{i=1}^N \left(5^2 \mathbf{I}\{\mathcal{B}_i = \mathcal{B}'_i\} + \left(\frac{1}{2}\right)^2 \mathbf{I}\{\mathcal{B}_i \neq \mathcal{B}'_i\} \right) \right] = \left[\mathbb{E} \left(5^2 \mathbf{I}\{\mathcal{B}_i = \mathcal{B}'_i\} + \left(\frac{1}{2}\right)^2 \mathbf{I}\{\mathcal{B}_i \neq \mathcal{B}'_i\} \right) \right]^N \quad (\text{C9})$$

$$= \left[5^2 \mathbb{E}[\mathbf{I}\{\mathcal{B}_i = \mathcal{B}'_i\}] + \left(\frac{1}{2}\right)^2 \mathbb{E}[\mathbf{I}\{\mathcal{B}_i \neq \mathcal{B}'_i\}] \right]^N = \left[5^2 \times \frac{1}{3} + \left(\frac{1}{2}\right)^2 \times \frac{2}{3} \right]^N = 8.5^N, \quad (\text{C10})$$

where we use the fact that the expectation of an indicator function is the probability of the associated event. More precisely, $\mathbb{E}[\mathbf{I}\{\mathcal{B}_i = \mathcal{B}'_i\}] = \Pr[\mathcal{B}_i = \mathcal{B}'_i] = 1/3$, because there is a total of three basis choices from which to choose. The same argument also ensures that $\mathbb{E}[\mathbf{I}\{\mathcal{B}_i \neq \mathcal{B}'_i\}] = \Pr[\mathcal{B}_i \neq \mathcal{B}'_i] = 1 - \Pr[\mathcal{B}_i = \mathcal{B}'_i] = 1 - 1/3 = 2/3$. ■

We now collect a number of helpful auxiliary statements that enable us to deduce tight bounds on the estimation protocol for OE further down the road. Some statements follow directly from the properties of classical shadows and are therefore valid for both Pauli and CUE shadows. Other results, however, do explicitly use the structure of Pauli-basis measurements and are therefore only valid for Pauli shadows.

Lemma 2: *Given a Pauli or Haar shadow $\hat{\rho}$ that acts on N qubits, let O be an observable on the same dimension. We have*

$$\text{Var}\left[\text{Tr}(O\hat{\rho})\right] \leq \mathbb{E}\left[\text{Tr}(O\hat{\rho})^2\right] \leq \text{Tr}(O^2)2^N. \quad (\text{C11})$$

Proof. The above statement follows from the proof of the original bound on the shadow norm of linear observables in Ref. [49] (proof of Proposition 3). ■

Lemma 3: *Let $\hat{\rho}$ and $\hat{\rho}'$ be two independent Pauli shadows on N qubits. Then, we have*

$$\text{Var}\left[\text{Tr}(\hat{\rho}\hat{\rho}')\right] \leq \mathbb{E}\left[\text{Tr}(\hat{\rho}\hat{\rho}')^2\right] \leq 8.5^N. \quad (\text{C12})$$

Proof. The proofs follow directly from Lemma 1 by taking the expectation value of Eq. (C7). ■

Lemma 4: *Let ρ_{AB} be a bipartite density matrix acting on $N = N_A + N_B$ qubits. Let $\hat{\rho} = \hat{\rho}_A \otimes \hat{\rho}_B$ and $\hat{\rho}' = \hat{\rho}'_A \otimes \hat{\rho}'_B$ be two Pauli or Haar shadows defined on the same space that are sampled independently. Given two observables O_{AB} and $O'_{A'B'}$ with compatible dimension, we have*

$$\text{Var}\left[\text{Tr}(O_{AB}\hat{\rho}_A \otimes \hat{\rho}'_B) \text{Tr}(O'_{A'B'}\hat{\rho}'_A \otimes \hat{\rho}_B)\right] \leq \mathbb{E}\left[\text{Tr}(O_{AB}\hat{\rho}_A \otimes \hat{\rho}'_B) \text{Tr}(O'_{A'B'}\hat{\rho}'_A \otimes \hat{\rho}_B)^2\right] \leq \text{Tr}(O_{AB}^2) \text{Tr}((O'_{A'B'})^2) 2^{2N}. \quad (\text{C13})$$

Proof. We can easily rewrite the product of traces as a larger trace over a tensor product:

$$\text{Tr}\left[(O_{AB} \otimes O'_{A'B'}) (\hat{\rho}_A \otimes \hat{\rho}'_B \otimes \hat{\rho}'_A \otimes \hat{\rho}_B)\right] = \text{Tr}\left[\mathbb{S}_{BB'}(O_{AB} \otimes O'_{A'B'}) \mathbb{S}_{BB'}(\hat{\rho}_A \otimes \hat{\rho}_B \otimes \hat{\rho}'_A \otimes \hat{\rho}'_B)\right] \quad (\text{C14})$$

where $\mathbb{S}_{BB'} \equiv \mathbb{I}_{AA'} \otimes \mathbb{S}_{BB'}$, which implicitly includes the identity operator on the unmarked subsystems A and A' . Writing the shadow $\hat{\rho} \otimes \hat{\rho}' = \hat{\rho}_A \otimes \hat{\rho}_B \otimes \hat{\rho}'_A \otimes \hat{\rho}'_B$ in a 2^{2N} -dimensional Hilbert space and recalling Lemma 2, we obtain

$$\text{Var}\left[\text{Tr}(O_{AB}\hat{\rho}_A \otimes \hat{\rho}'_B) \text{Tr}(O'_{A'B'}\hat{\rho}'_A \otimes \hat{\rho}_B)\right] \leq \text{Tr}\left[(\mathbb{S}_{BB'}(O_{AB} \otimes O'_{A'B'}) \mathbb{S}_{BB'})^2\right] 2^{2N} \leq \text{Tr}(O_{AB}^2) \text{Tr}((O'_{A'B'})^2) 2^{2N}. \quad (\text{C15})$$

■

2. General treatment for batch-shadow estimators

In this section, we introduce the batch-shadow estimator—one of the main technical contributions of this work. We also provide general statements that allow us to bound its variance when estimating trace polynomials $\text{Tr}(O^{(n)}\rho^{\otimes n})$ of arbitrary order n .

For all the subsequent sections, we start by performing randomized measurements to construct classical or Pauli shadows of an N -qubit state ρ . As mentioned in the main text, on each run of the protocol, we sample N single-qubit random unitaries from the CUE or a 2-design and apply them locally on each qubit. This is followed by a single computational-basis measurement on each qubit ($N_M = 1$). This procedure is repeated M times (on fresh copies of the state ρ) and allows us to construct M classical shadows $\hat{\rho}^{(r)}$ of ρ , for $r = 1, \dots, M$ [49] (here, $M \equiv N_u$ as written in the main text). We know that the expectation value of the classical shadows is $\mathbb{E}[\hat{\rho}] = \rho$ [49]. We would like to estimate an n th-order functional $X_n = \text{Tr}(O^{(n)}\rho^{\otimes n})$, defined as a function of an n -copy operator $O^{(n)}$ using classical shadows.

From the classical shadows, we can define X_n U-statistics estimator \hat{X}_n as

$$\hat{X}_n = \frac{(M-n)!}{M!} \sum_{r_1 \neq \dots \neq r_n} \text{Tr} \left[O^{(n)} \bigotimes_{i=1}^n \hat{\rho}^{(r_i)} \right], \quad (\text{C16})$$

where the sum ranges over all possible disjoint shadow indices $(r_1, \dots, r_n) \in \{0, \dots, M\}^{\times n}$ with $r_1 \neq \dots \neq r_n$. The U-statistics estimator is an unbiased estimator, i.e., $\mathbb{E}[\hat{X}_n] = X_n$ [90,124,125], but evaluating it requires a summation over all possible disjoint sets of n indices. While this is doable for $n = 1, 2$, this summation quickly becomes unfeasible as n increases. For the sake of illustration, in order to estimate the U-statistics estimator of the purity ($\text{Tr}(\rho^2)$) with classical shadows, the postprocessing run time scales quadratically, $\mathcal{O}(M^2)$, with the number of measurements M scaling exponentially with respect to the system size N ($M \propto 2^N$) [8,90,125]. On the other hand, a function involving $n = 4$ copies of ρ immediately exposes the bottleneck of the U-statistics estimator. The number of summands to be calculated in Eq. (C16) quickly becomes overburdening even for moderate system sizes, as the run time scales as $\mathcal{O}(M^4)$, with an overhead exponential scaling of the number of measurements M , and requires other alternatives.

To solve this real scaling problem, we propose another unbiased estimator of the same functional X_n by distributing our M shadows into $n' \geq n$ subsets and first averaging the shadows in each subset. Each such defined subset is independent with respect to any other and can independently approximate ρ . More specifically, let us define the b th *batch shadow* (denoted by a tilde rather than a hat) as

$$\tilde{\rho}^{(b)} = \frac{n'}{M} \sum_{t_b \in T_b} \hat{\rho}^{(t_b)} \in \mathbb{C}^{2^N \times 2^N}, \quad \text{where } T_b = \{1 + (b-1)M/n', \dots, bM/n'\} \quad (\text{C17})$$

for batches ranging from $b = 1$ to $b = n'$ (for simplicity, we assume that n' divides M such that each subset contains M/n' original classical shadows). We note, as claimed above, that $\mathbb{E}[\tilde{\rho}^{(b)}] = \rho$ for every b . We then define the alternative unbiased estimator $\tilde{X}_n^{(n')}$ of X_n in a similar fashion to Eq. (C16). However, we now symmetrize over n' batch shadows:

$$\tilde{X}_n^{(n')} = \frac{(n'-n)!}{n'!} \sum_{b_1 \neq \dots \neq b_n} \text{Tr} \left[O^{(n)} \bigotimes_{i=1}^n \tilde{\rho}^{(b_i)} \right] = \frac{(n'-n)!}{n'!} \frac{n^n}{M^n} \sum_{b_1 \neq \dots \neq b_n} \sum_{t_{b_1} \in T_{b_1}, \dots, t_{b_n} \in T_{b_n}} \text{Tr} \left[O^{(n)} \bigotimes_{i=1}^n \hat{\rho}^{(t_{b_i})} \right]. \quad (\text{C18})$$

Again, by construction, $\mathbb{E}[\tilde{X}_n^{(n')}] = X_n$, i.e., the *batch-shadow estimator*, is unbiased. The principal advantage of introducing this data-splitting estimator lies in the fact that, in the limit of $n' \ll M$, one can more efficiently postprocess arbitrary n th-order functionals $\tilde{X}_n^{(n')}$ compared to the basic U-statistics estimators \hat{X}_n . This is because all the batch shadows $\tilde{\rho}^{(b)}$ are independent and can be computed in parallel.

By increasing n' , the performance of $\tilde{X}_n^{(n')}$ is improved in terms of convergence, as more distinct ordered pairings of n different shadows $\hat{\rho}^{(r_1)}, \dots, \hat{\rho}^{(r_n)}$ are incorporated in the batch estimator that were not considered before. In the final limit of $n' = M$, we actually recover the full U-statistics estimator $\tilde{X}_n^{(M)} = \hat{X}_n$, which has already been studied in detail [90]. However, the larger the n' , the more resource intensive is the classical postprocessing. Hence, we analyze the performance of this estimator in regimes where the batch size n' is as small as possible, i.e., $n' = n$ (this is the smallest batch size that still produces an unbiased estimator for $\text{Tr}(O^{(n)} \rho^{\otimes n})$). In this case, the sum over $b_1 \neq \dots \neq b_n$ simply boils down to computing all possible position shuffles in the tensor product of the n independent batch shadows. This can be more formally written as a sum over all the permutation operator π that acts on n copies of the shadows and leads to

$$\tilde{X}_n^{(n)} = \frac{1}{n!} \frac{n^n}{M^n} \sum_{\pi} \sum_{t_1 \in T_1, \dots, t_n \in T_n} \text{Tr} \left[O^{(n)} \pi \bigotimes_{i=1}^n \hat{\rho}^{(t_i)} \pi^\dagger \right], \quad (\text{C19})$$

where π denotes the operator that permutes the n shadows correspondingly: $\pi = \sum_{j_1, \dots, j_n} |j_{\pi(1)}\rangle \langle j_1| \otimes \dots \otimes |j_{\pi(n)}\rangle \langle j_n|$ (where the $|j_i\rangle$ are orthonormal basis states). We can gauge its performance by calculating the required number of measurements M to estimate X_n with an error $|\tilde{X}_n^{(n)} - X_n| \leq \epsilon$ and a certain confidence level. Chebyshev's inequality

yields

$$\Pr[|\tilde{X}_n^{(n)} - X_n| \geq \epsilon] \leq \frac{\text{Var}[\tilde{X}_n^{(n)}]}{\epsilon^2} \quad (\text{C20})$$

and isolates the variance $\text{Var}[\tilde{X}_n^{(n)}]$ of the batch-shadow estimator as the central object to study convergence. Using the decomposition of Eq. (C19), this variance can be rewritten as

$$\text{Var}[\tilde{X}_n^{(n)}] = \left(\frac{1}{n!} \frac{n^n}{M^n}\right)^2 \sum_{\pi, \pi'} \sum_{t_1, t'_1 \in T_1, \dots, t_n, t'_n \in T_n} \text{Cov} \left[\text{Tr} \left[O^{(n)} \pi \bigotimes_{i=1}^n \hat{\rho}^{(t_i)} \pi^\dagger \right], \text{Tr} \left[O^{(n)} \pi' \bigotimes_{i=1}^n \hat{\rho}^{(t'_i)} \pi'^{\dagger} \right] \right]. \quad (\text{C21})$$

Note that all shadows that appear only once in the covariances above (i.e., those with indices $t_i \neq t'_i$) simply average to ρ . The shadows that appear twice (those with indices $t_i = t'_i$), on the other hand, contribute less trivially. Furthermore, because of the averaging over all permutations π, π' , the positions of the shadows appearing twice (i.e., the indices i such that $t_i = t'_i$) do not matter. Hence, we can first sum over the number k of shadows appearing twice: the $\binom{n}{k}$ corresponding terms then contribute with the same values of the covariances. We thus obtain

$$\begin{aligned} \text{Var}[\tilde{X}_n^{(n)}] &= \left(\frac{1}{n!} \frac{n^n}{M^n}\right)^2 \sum_{\pi, \pi'} \sum_{k=0}^n \binom{n}{k} \sum_{\substack{t_1 \in T_1 \\ \vdots \\ t_k \in T_k}} \sum_{\substack{\tau_{k+1} \neq \tau'_{k+1} \in T_{k+1} \\ \vdots \\ \tau_n \neq \tau'_n \in T_n}} \text{Cov} \left[\text{Tr} \left[\pi^\dagger O^{(n)} \pi \left[\bigotimes_{i=1}^k \hat{\rho}^{(t_i)} \bigotimes_{j=k+1}^n \hat{\rho}^{(\tau_j)} \right] \right], \right. \\ &\quad \left. \text{Tr} \left[\pi'^{\dagger} O^{(n)} \pi' \left[\bigotimes_{i=1}^k \hat{\rho}^{(t_i)} \bigotimes_{j=k+1}^n \hat{\rho}^{(\tau'_j)} \right] \right] \right] \\ &= \left(\frac{1}{n!} \frac{n^n}{M^n}\right)^2 \sum_{\pi, \pi'} \sum_{k=0}^n \binom{n}{k} \left(\frac{M}{n}\right)^k \left(\frac{M}{n} \left(\frac{M}{n} - 1\right)\right)^{n-k} \text{Cov} \left[\text{Tr} \left[\pi^\dagger O^{(n)} \pi \left[\bigotimes_{r=1}^k \hat{\rho}^{(r)} \otimes \rho^{\otimes(n-k)} \right] \right], \right. \\ &\quad \left. \text{Tr} \left[\pi'^{\dagger} O^{(n)} \pi' \left[\bigotimes_{r=1}^k \hat{\rho}^{(r)} \otimes \rho^{\otimes(n-k)} \right] \right] \right] \\ &= \sum_{k=0}^n \binom{n}{k} \left(\frac{n}{M}\right)^k \left(1 - \frac{n}{M}\right)^{n-k} \text{Var} \left[\frac{1}{n!} \sum_{\pi} \text{Tr} \left[\pi^\dagger O^{(n)} \pi \left[\bigotimes_{r=1}^k \hat{\rho}^{(r)} \otimes \rho^{\otimes(n-k)} \right] \right] \right], \end{aligned} \quad (\text{C22})$$

where from the first to the second lines (in addition to averaging the shadows $\hat{\rho}^{(\tau_j)}, \hat{\rho}^{(\tau'_j)}$ to ρ ; see above), we note that all different shadows $\hat{\rho}^{(t_i)}$ give the same statistics (and hence the same covariances), so that we could, without loss of generality, replace the k shadows $\hat{\rho}^{(t_i)}$ by any other k shadows $\hat{\rho}^{(r)}$, e.g., those for $r = 1, \dots, k$. All M/n terms from each of the k sums over $t_i \in T_i$, and all $M/n(M/n - 1)$ terms from each of the $n - k$ sums over $\tau_j \neq \tau'_j \in T_j$, then give the same values. For the last line, we just rearrange all prefactors and include the sums over π, π' inside the covariances, noting that the two arguments of the covariances are then the same.

Let us note already that the variance term inside the sum of Eq. (C22) cancels for $k = 0$: the sum can therefore be taken to start from $k = 1$. Defining, for convenience,

$$V_k = \text{Var} \left[\frac{1}{n!} \sum_{\pi} \text{Tr} \left[\pi^\dagger O^{(n)} \pi \left[\bigotimes_{r=1}^k \hat{\rho}^{(r)} \otimes \rho^{\otimes(n-k)} \right] \right] \right], \quad (\text{C23})$$

we obtain

$$\text{Var}[\tilde{X}_n^{(n)}] = \sum_{k=1}^n \binom{n}{k} \left(\frac{n}{M}\right)^k \left(1 - \frac{n}{M}\right)^{n-k} V_k \quad (\text{C24})$$

$$= \sum_{\ell=1}^n \binom{n}{\ell} \left(\frac{n}{M}\right)^\ell \left[\sum_{k=1}^{\ell} \binom{\ell}{k} (-1)^{\ell-k} V_k \right] = \frac{n^2}{M} V_1 + \frac{n^3(n-1)}{2M^2} (V_2 - 2V_1) + \mathcal{O}\left(\frac{1}{M^2}\right). \quad (\text{C25})$$

This analysis of the special case $n' = n$ (the number of batches equals the order of the trace functional) readily extends to general batch sizes n' . Similar calculations produce the following generalization of Eq. (C25):

$$\text{Var}[\tilde{X}_n^{(n')}] = \sum_{j=1}^n \binom{n}{j} \frac{\binom{n'-n}{n-j}}{\binom{n'}{n}} \sum_{k=1}^j \binom{j}{k} \left(\frac{n'}{M}\right)^k \left(1 - \frac{n'}{M}\right)^{j-k} V_k = \sum_{\ell=1}^n \frac{\binom{n}{\ell}^2}{\binom{n'}{\ell}} \left(\frac{n'}{M}\right)^\ell \left[\sum_{k=1}^{\ell} \binom{\ell}{k} (-1)^{\ell-k} V_k \right] \quad (\text{C26})$$

$$= \frac{n^2}{M} V_1 + \frac{n^2(n-1)^2 \frac{n'}{n'-1}}{2M^2} (V_2 - 2V_1) + \mathcal{O}\left(\frac{1}{M^2}\right). \quad (\text{C27})$$

We can provide bounds to all the above variance expressions by using the fact that the variance of an average of random variables is upper bounded by the average of the variances. This can be seen as follows. For K random variables X_i , the Cauchy-Schwarz inequality yields

$$\left(\frac{1}{K} \sum_{i=1}^K X_i - \mathbb{E}\left[\frac{1}{K} \sum_{i=1}^K X_i\right]\right)^2 = \langle \vec{\mathbf{1}}/K, (\vec{X} - \mathbb{E}[\vec{X}]) \rangle^2 \leq \|\vec{\mathbf{1}}/K\|^2 \|\vec{X} - \mathbb{E}[\vec{X}]\|^2 = \frac{1}{K} \sum_{i=1}^K (X_i - \mathbb{E}[X_i])^2 \quad (\text{C28})$$

where $\vec{X} = (X_1, \dots, X_K)$ and $\vec{\mathbf{1}} = (1, \dots, 1)$. Taking the expectation values on both sides gives $\text{Var}[1/K \sum_{i=1}^K X_i] \leq 1/K \sum_{i=1}^K \text{Var}[X_i]$. This provides us with the bound

$$V_k = \text{Var}\left[\frac{1}{n!} \sum_{\pi} \text{Tr}\left[\pi^\dagger \mathcal{O}^{(n)} \pi [\otimes_{r=1}^k \hat{\rho}^{(r)} \otimes \rho^{\otimes(n-k)}]\right]\right] \leq \bar{V}_k = \frac{1}{n!} \sum_{\pi} \text{Var}\left[\text{Tr}\left[\mathcal{O}^{(n)} \pi [\otimes_{r=1}^k \hat{\rho}^{(r)} \otimes \rho^{\otimes(n-k)}]\right] \pi^\dagger\right] \quad (\text{C29})$$

and helps us to formalize the variance bound for an arbitrary batch-shadow estimator.

Proposition 6: *Let $\text{Tr}(\mathcal{O}^{(n)} \rho^{\otimes n})$ be an n th-order trace function and let $\tilde{X}_n^{n'}$ with $n' \geq n$ be the associated batch-shadow estimator as defined in Eq. (C18). Then, the associated variance obeys*

$$\text{Var}[\tilde{X}_n^{(n')}] \leq \sum_{j=1}^n \binom{n}{j} \frac{\binom{n'-n}{n-j}}{\binom{n'}{n}} \sum_{k=1}^j \left(\frac{n'}{M}\right)^k \left(1 - \frac{n'}{M}\right)^{j-k} \bar{V}_k. \quad (\text{C30})$$

For $n' = n$, this bound further simplifies to

$$\text{Var}[\tilde{X}_n^{(n)}] \leq \sum_{k=1}^n \binom{n}{k} \left(\frac{n}{M}\right)^k \left(1 - \frac{n}{M}\right)^{n-k} \bar{V}_k. \quad (\text{C31})$$

One can further bound \bar{V}_k using the formalism introduced in Ref. [90]. Then, using the Chebyshev bound, one can obtain concrete sample-complexity bounds to evaluate arbitrary functions $\tilde{X}_n^{n'}$ using batch shadows. More concretely, for comparison with the U-statistics estimator, Eq. (D7) of Ref. [90], we can rewrite the U-statistics estimator as

$$\text{Var}[\hat{X}_n] = \sum_{k=1}^n \binom{n}{k} \frac{\binom{M-n}{n-k}}{\binom{M}{n}} V_k = \sum_{\ell=1}^n \frac{\binom{n}{\ell}^2}{\binom{M}{\ell}} \left[\sum_{k=1}^{\ell} \binom{\ell}{k} (-1)^{\ell-k} V_k \right]. \quad (\text{C32})$$

To first and second order in $1/M$, by taking $M \gg 1$, we now obtain

$$\text{Var}[\hat{X}_n] \simeq \frac{n^2}{M} V_1 + \frac{n^2(n-1)^2}{2M^2} (V_2 - 2V_1) + \mathcal{O}\left(\frac{1}{M^2}\right). \quad (\text{C33})$$

We note that the behavior for large M depends on how n' relates to M : whether n' is taken to be independent of M (as in the case $n' = n$) or whether it is taken to just be proportional to M (as in the other extreme case, $n' = M$, which reproduces standard U-statistics). One finds that $\text{Var}[\tilde{X}_n^{(n')}]$ and $\text{Var}[\hat{X}_n]$ have the same behavior as $\frac{n^2}{M} V_1$ at first order in $1/M$ for any value of n' . At second order, $\text{Var}[\tilde{X}_n^{(n')}]$ is only slightly (by a factor $n'/(n'-1)$) larger than $\text{Var}[\hat{X}_n]$. Hence, we really do

not lose much in the precision when we use our new batch-shadow technique instead of the standard U-statistics estimator of the classical shadows, while we evidently achieve great improvements in run times of the classical treatment of the measurement data.

With these general statements at hand, we are now in a position to employ them in order to deduce concrete and simple variance bounds for the simplest (and most relevant) batch-shadow estimator ($n' = n$) for the functions of interest in this paper as introduced in the main text: for the purity $X_2 = \text{Tr}(\rho_{\text{AB}}^2) = \text{Tr}(\mathbb{S}_{1,2}^{(\text{AB})} \rho_{\text{AB}} \otimes \rho_{\text{AB}})$ and for the functional where $\mathcal{O}^{(4)} = \mathcal{S}$: $X_4 = \text{Tr}(\mathcal{S} \rho_{\text{AB}}^{\otimes 4}) = \text{Tr}(\mathbb{S}_{1,4}^{(A)} \otimes \mathbb{S}_{2,3}^{(A)} \otimes \mathbb{S}_{1,2}^{(B)} \otimes \mathbb{S}_{3,4}^{(B)} \rho_{\text{AB}}^{\otimes 4})$. We then provide the sample-complexity bounds to evaluate our quantities using properties given in Appendix C 1.

3. Sample complexity to evaluate the purity

This section aims at providing sample-complexity bounds to evaluate the purity using the batch-shadow estimator formed using two batches of Pauli shadows. The purity of a N -qubit quantum state ρ_{AB} can be expressed as

$$X_2 = \text{Tr}(\mathbb{S}_{1,2}^{(\text{AB})} \rho_{\text{AB}} \otimes \rho_{\text{AB}}) = \text{Tr}(\rho_{\text{AB}}^2), \quad (\text{C34})$$

where $\mathbb{S}_{1,2}^{(\text{AB})}$ is the swap operator. Given M Pauli shadows, the corresponding batch-shadow estimator $\tilde{X}_2^{(2)}$ (with $n' = 2$) of the purity can be written as

$$\tilde{X}_2^{(2)} = \frac{1}{2!} \sum_{b_1 \neq b_2} \text{Tr} \left[\mathbb{S}_{1,2}^{(\text{AB})} \bigotimes_{i=1}^2 \tilde{\rho}^{(b_i)} \right], \quad (\text{C35})$$

where each batch shadow $\tilde{\rho}^{(b)}$, for $b = 1, 2$, is written as

$$\tilde{\rho}^{(b)} = \frac{2}{M} \sum_{r=(b-1)M/2+1}^{bM/2} \hat{\rho}^{(r)}. \quad (\text{C36})$$

Our goal is to bound $\text{Var}[\tilde{X}_2^{(2)}]$ for Pauli shadows (this restriction is important, because we need all auxiliary the statements from Appendix C 1). Using Proposition 6, this variance explicitly can be bounded as

$$\text{Var}[\tilde{X}_2^{(2)}] \leq \frac{4}{M} \bar{V}_1 + \frac{4}{M^2} (\bar{V}_2 - 2\bar{V}_1) \leq \frac{4}{M} \bar{V}_1 + \frac{4}{M^2} \bar{V}_2. \quad (\text{C37})$$

The next step consists of obtaining the bounds on the terms \bar{V}_k . From the expression of Eq. (C29), we note that for $n = 2$, only two permutations need to be considered: $\pi = \mathbb{I}$ and $\pi = \mathbb{S}$. In each case, $\pi^\dagger \mathcal{O}^{(2)} \pi = \pi^\dagger \mathbb{S} \pi = \mathbb{S}$. Now recalling Lemmas 2 and 3, we can compute the bounds on \bar{V}_1 and \bar{V}_2 , respectively:

$$\bar{V}_1 = \text{Var} \left[\text{Tr} \left[\mathbb{S}_{1,2}^{(\text{AB})} (\hat{\rho} \otimes \rho_{\text{AB}}) \right] \right] = \text{Var} \left[\text{Tr} [\hat{\rho} \rho_{\text{AB}}] \right] \leq \text{Tr} [\rho_{\text{AB}}^2] 2^N \leq 2^N, \quad (\text{C38})$$

$$\bar{V}_2 = \text{Var} \left[\text{Tr} \left[\mathbb{S}_{1,2}^{(\text{AB})} (\hat{\rho}^{(1)} \otimes \hat{\rho}^{(2)}) \right] \right] = \text{Var} \left[\text{Tr} [\hat{\rho}^{(1)} \hat{\rho}^{(2)}] \right] \leq 8.5^N \leq 3^{2N}. \quad (\text{C39})$$

Then, from Eq. (C37), we obtain the following bound on $\text{Var}[\tilde{X}_2^{(2)}]$:

$$\text{Var}[\tilde{X}_2^{(2)}] \leq \frac{4}{M} \bar{V}_1 + \frac{4}{M^2} \bar{V}_2 \leq \frac{4}{M} 2^N + \frac{4}{M^2} 3^{2N}. \quad (\text{C40})$$

Recalling Chebyshev's inequality mentioned in Eq. (C20), we conclude that

$$\Pr[|\tilde{X}_2^{(2)} - X_2| \geq \epsilon] \leq \frac{\text{Var}[\tilde{X}_2^{(2)}]}{\epsilon^2} \leq \frac{4}{\epsilon^2} \left[\frac{2^N}{M} + \frac{3^{2N}}{M^2} \right]. \quad (\text{C41})$$

This allows us to formulate a concise sample-complexity bound.

Proposition 7: Suppose that we wish to estimate the purity $X_2 = \text{Tr}(\rho_{AB}^2) = \text{Tr}(\mathbb{S}_{1,2}^{(AB)} \rho_B^{\otimes 2})$ of an N -qubit state ρ using the batch-shadow estimator $\tilde{X}_2^{(2)}$ constructed from Pauli shadows. Then, for $\epsilon, \delta \in (0, 1)$, a total of

$$M \geq 2 \frac{3^N}{\epsilon \sqrt{\delta}} \left(\sqrt{1 + a_N^2} + a_N \right) \quad \text{with} \quad a_N = \left(\frac{2}{3} \right)^N / \epsilon \sqrt{\delta} \quad (\text{C42})$$

measurements suffices to ensure $\Pr[|\tilde{X}_2^{(2)} - X_2| \geq \epsilon] \leq \delta$.

The scaling in terms of system size N is dominated by 3^N , which is a strict improvement over general quantum state tomography (which would require at least $4^N/\epsilon^2$ measurements). This kind of scaling for the purity is also observed for SIC-POVM measurements on independent copies, where the sample-complexity bound scales as $M \propto 3^N/\epsilon^2\delta$ [123]. However, when M becomes sufficiently large, the scaling in Eq. (C40) is dominated by the first term ($k = 1$), which is $\propto 2^N/M$. This then produces a measurement complexity that scales as $M \propto 2^N/\epsilon^2\delta$. Similar scaling behavior in this limit $M \rightarrow \infty$ has also been observed in Refs. [8,90] and reproduces an error decay rate proportional to $1/\sqrt{M}$ —the ultimate limit for any Monte Carlo averaging procedure.

4. Sample complexity of X_4

In this section, we derive analytical expressions to compute the sample-complexity bound on the X_4 functional. We use tensor-network graphical language to facilitate the understanding of the subsequent calculations for the reader. Tensor-network diagrams are popular in rendering heavy expressions of calculations in terms of simple graphical representations. For interested readers, we refer to Refs. [126–128] for a thorough introduction. Figure 5 summarizes all the essential graphical tools that are required for our arguments.

The function X_4 defined in terms of the four-copy operator $O^{(4)} = \mathcal{S}$ (as introduced in the main text in Eq. (16) and also in Ref. [65]) for a bipartite ($N = N_A + N_B$)-qubit state can be rewritten as

$$X_4 = \text{Tr}(\mathcal{S} \rho_{AB}^{\otimes 4}) = \text{Tr}(\mathbb{S}_{1,4}^{(A)} \otimes \mathbb{S}_{2,3}^{(A)} \otimes \mathbb{S}_{1,2}^{(B)} \otimes \mathbb{S}_{3,4}^{(B)} \rho_{AB}^{\otimes 4}) \quad (\text{C43})$$

$$= \text{Tr}_{A'ABB'} \left[(\rho_{AB} \mathbb{S}_{AA'} \rho_{AB} \mathbb{S}_{BB'}) (\rho_{AB} \mathbb{S}_{AA'} \rho_{AB} \mathbb{S}_{BB'}) \right], \quad (\text{C44})$$

where $\mathbb{S}_{c,d}^{(\Gamma)}$, with $c, d \in [1, \dots, 4]$ and $\Gamma \in \{A, B\}$, is the swap operator acting on system Γ on the copies c and d of the density matrices ρ_{AB} . In the above expression, we also assume an implicit reordering of the tensor products and identity operators on the unmarked subsystems $\rho_{AB} \equiv \rho_{AB} \otimes \mathbb{I}_{A'B'}$, $\mathbb{S}_{AA'} \equiv \mathbb{S}_{AA'} \otimes \mathbb{I}_{BB'}$ and $\mathbb{S}_{BB'} \equiv \mathbb{I}_{AA'} \otimes \mathbb{S}_{BB'}$. Figure 6 shows an equivalent expression of X_4 as a tensor-network diagram. We consider here the simplest batch-shadow estimator $\tilde{X}_4^{(4)}$ of this function that can be evaluated from M Pauli shadows, as

$$\tilde{X}_4^{(4)} = \frac{1}{4!} \sum_{b_1 \neq \dots \neq b_4} \text{Tr} \left[\mathcal{S} \bigotimes_{i=1}^4 \tilde{\rho}^{(b_i)} \right], \quad (\text{C45})$$

where each batch shadow $\tilde{\rho}^{(b)}$, for $b = 1, \dots, 4$ is an average over $M/4$ Pauli shadows, given as

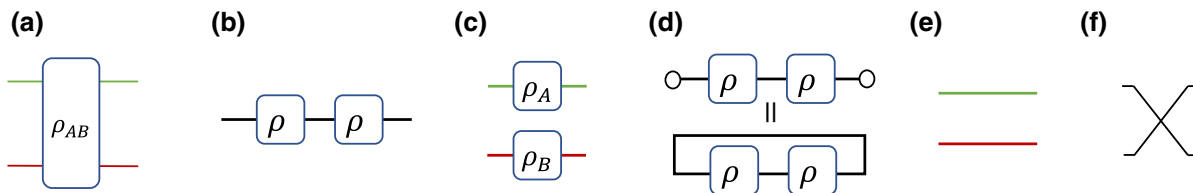


FIG. 5. Important tensor-network diagrams. (a) A bipartite quantum state ρ_{AB} , with the green (or red) legs defining the indices of subsystem A (or B), respectively. (b) By index contraction, we have multiplication of two matrices, giving ρ^2 . (c) $\rho_A \otimes \rho_B$. (d) $\text{Tr}(\rho^2)$, where we replace the standard trace loop by circles at the end points that virtually connect to each other only horizontally at the same level. (e) The identity function of each subsystem, $\mathbb{I}_A \otimes \mathbb{I}_B = \mathbb{I}_{AB}$. (f) The swap operator: $\mathbb{S}_{k,l}(|i_k\rangle \otimes |i_l\rangle) = |i_l\rangle \otimes |i_k\rangle$.

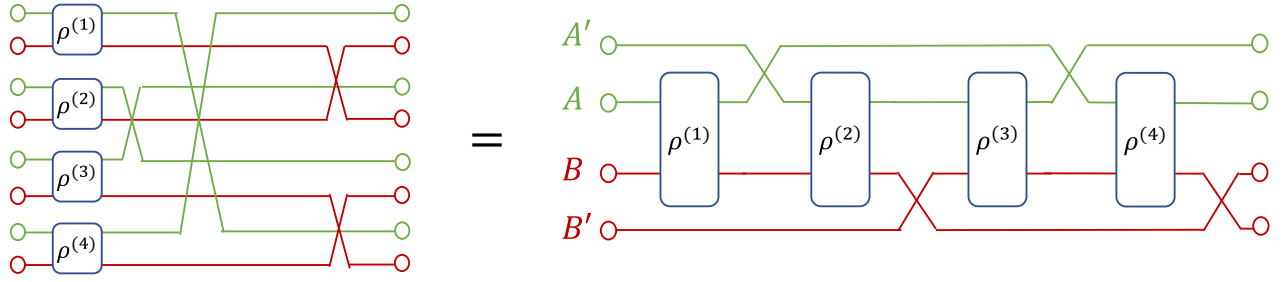


FIG. 6. The graphical expression of X_4 . The expression of $X_4 = \text{Tr}\left(\mathbb{S}_{1,4}^{(A)} \otimes \mathbb{S}_{2,3}^{(A)} \otimes \mathbb{S}_{1,2}^{(B)} \otimes \mathbb{S}_{3,4}^{(B)}\right)(\rho^{(1)} \otimes \rho^{(2)} \otimes \rho^{(3)} \otimes \rho^{(4)}) = \text{Tr}\left[\mathbb{S}_{BB'} \rho^{(4)} \mathbb{S}_{AA'} \rho^{(3)} \mathbb{S}_{BB'} \rho^{(2)} \mathbb{S}_{AA'} \rho^{(1)}\right]$ in terms of the diagrammatic notation introduced earlier.

$$\tilde{\rho}^{(b)} = \frac{4}{M} \sum_{r=(b-1)M/4+1}^{bM/4} \hat{\rho}^{(r)}. \quad (\text{C46})$$

Our task is to bound the variance $\text{Var}[\tilde{X}_4^{(4)}]$. With the help of Proposition 6, we can simply bound the corresponding variance as

$$\text{Var}[\tilde{X}_4^{(4)}] \leq \sum_{k=1}^4 \binom{4}{k} \left(\frac{4}{M}\right)^k \left(1 - \frac{4}{M}\right)^{4-k} \bar{V}_k \leq \sum_{k=1}^4 \binom{4}{k} \left(\frac{4}{M}\right)^k \bar{V}_k, \quad (\text{C47})$$

where each of the \bar{V}_k can be expressed from Eq. (C29) as

$$\bar{V}_k = \frac{1}{4!} \sum_{\pi} \text{Var}\left[\text{Tr}\left[\mathcal{S}\pi\left[\otimes_{r=1}^k \hat{\rho}^{(r)} \otimes \rho_{AB}^{\otimes(4-k)}\right]\pi^\dagger\right]\right]. \quad (\text{C48})$$

Our goal now is to calculate explicitly the bounds on the term \bar{V}_k for each value of $k = 1, \dots, 4$:

- (a) For $k = 1$, the trace terms in \bar{V}_1 contain a single Pauli shadow $\hat{\rho}^{(1)}$ and three density matrices ρ_{AB} . Regardless of π , we always obtain the same expression for the traces in Eq. (C29), which explicitly read as

$$\text{Tr}\left[\mathcal{S}[\hat{\rho}^{(1)} \otimes \rho_{AB}^{\otimes 3}]\right] = \text{Tr}[\tilde{\mathcal{S}}^{(1)} \hat{\rho}^{(1)}], \quad \text{with} \quad \tilde{\mathcal{S}}^{(1)} = \text{Tr}_{A'B'}[\mathbb{S}_{BB'} \rho_{AB} \mathbb{S}_{AA'} \rho_{AB} \mathbb{S}_{BB'} \rho_{AB} \mathbb{S}_{AA'}]; \quad (\text{C49})$$

see also the diagrammatic expression given in Fig. 7 for a visual illustration. We note that $\tilde{\mathcal{S}}^{(1)}$ is a Hermitian operator. Using Lemma 2, we can bound \bar{V}_1 as

$$\bar{V}_1 \leq \text{Var}\left[\text{Tr}\left(\mathcal{S}[\hat{\rho}^{(1)} \otimes \rho_{AB}^{\otimes 3}]\right)\right] = \text{Var}\left[\text{Tr}(\tilde{\mathcal{S}}^{(1)} \hat{\rho}^{(1)})\right] \leq \text{Tr}[(\tilde{\mathcal{S}}^{(1)})^2] 2^N. \quad (\text{C50})$$

From Fig. 7(b), we can further expand the trace term $\text{Tr}[(\tilde{\mathcal{S}}^{(1)})^2]$ by performing the appropriate diagrammatic tensor contractions. We can then explicitly write it as

$$\text{Tr}[(\tilde{\mathcal{S}}^{(1)})^2] = \text{Tr}(\tilde{O}^{(6)} \rho_{AB}^{\otimes 6}), \quad \text{with} \quad \tilde{O}^{(6)} = \mathbb{S}_{1,2}^{(A)} \otimes \mathbb{S}_{3,6}^{(A)} \otimes \mathbb{S}_{4,5}^{(A)} \otimes \mathbb{S}_{1,4}^{(B)} \otimes \mathbb{S}_{2,3}^{(B)} \otimes \mathbb{S}_{5,6}^{(B)}. \quad (\text{C51})$$

We now use Hölder's inequality for matrices ($|\text{Tr}(AB)| \leq \|A\|_1 \|B\|_\infty$, where $\|\cdot\|_1$ and $\|\cdot\|_\infty$ denote the trace and operator norm, and also define, for completeness, for a matrix C , $|C| = \sqrt{C^\dagger C}$ and the Schatten p -norm of C : $\|C\|_p = [\text{Tr}(|C|^p)]^{1/p}$). Now we can relate this upper bound to a product of matrix norms that is easier to parse:

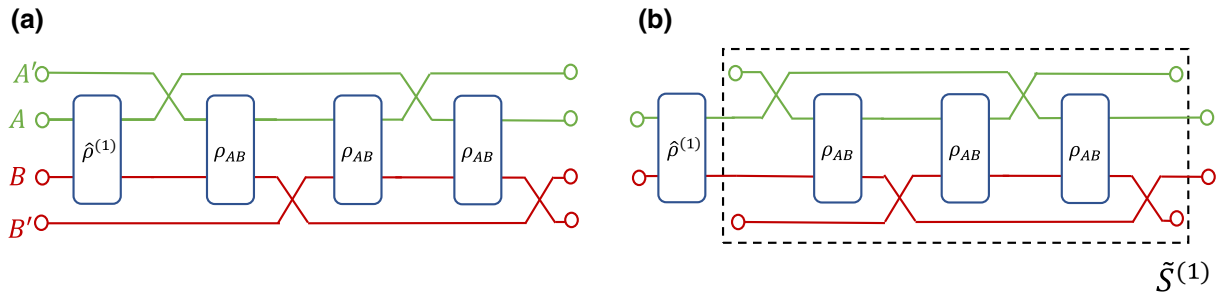


FIG. 7. The graphical representation for the case $k = 1$. (a) A diagrammatic expression of $\text{Tr}(\mathcal{S}[\hat{\rho}^{(1)} \otimes \rho_{AB}^{\otimes 6}])$, from which it is easily seen that the expression is invariant with respect to any position of the shadow $\hat{\rho}^{(1)}$. (b) The operator $\tilde{S}^{(1)}$ in Eq. (C49) (marked in the dashed rectangle) that acts on $\hat{\rho}^{(1)}$.

$$\text{Tr}((\tilde{S}^{(1)})^2) \leq |\text{Tr}(\tilde{O}^{(6)} \rho_{AB}^{\otimes 6})| \leq \|\tilde{O}^{(6)}\|_{\infty} \|\rho_{AB}^{\otimes 6}\|_1 = 1 \times 1 = 1, \quad (\text{C52})$$

because the sixfold tensor product $\rho_{AB}^{\otimes 6}$ of a quantum state is again a quantum state that is normalized in trace norm ($\|\rho_{AB}^{\otimes 6}\|_1 = \|\rho_{AB}\|_1^6 = \text{Tr}(\rho_{AB})^6 = 1^6 = 1$) and $\tilde{O}^{(6)}$ is a tensor product of swap operators and is therefore unitary. The unitary operators U , in particular, obey $\|U\|_{\infty} = 1$. Thus, we obtain the following streamlined bound on \overline{V}_1 :

$$\overline{V}_1 \leq 2^N \leq 3^N. \quad (\text{C53})$$

The final inequality ($2^N \leq 3^N$) is very loose but considerably simplifies the final stage, where we put all our bounds together.

- (b) For $k = 2$, the variance term contains combinations of two distinct Pauli shadows $\hat{\rho}^{(1)} = \hat{\rho}_A^{(1)} \otimes \hat{\rho}_B^{(1)}$ and $\hat{\rho}^{(2)} = \hat{\rho}_A^{(2)} \otimes \hat{\rho}_B^{(2)}$, as well as two density matrices ρ_{AB} . From all possible permutations, we need to consider three families of permutations that give different contributions to Eq. (C29), with each family containing the same number of permutations:

- (1) If $\pi[\hat{\rho}^{(1)} \otimes \hat{\rho}^{(2)} \otimes \rho_{AB} \otimes \rho_{AB}]\pi^{\dagger} = \hat{\rho}^{(1)} \otimes \hat{\rho}^{(2)} \otimes \rho_{AB} \otimes \rho_{AB}$ or $\rho_{AB} \otimes \rho_{AB} \otimes \hat{\rho}^{(1)} \otimes \hat{\rho}^{(2)}$, or with the indices 1 and 2 exchanged on the right-hand sides, then [cf. Fig. 8(a)]

$$\text{Tr}[\mathcal{S} \pi[\hat{\rho}^{(1)} \otimes \hat{\rho}^{(2)} \otimes \rho_{AB} \otimes \rho_{AB}]\pi^{\dagger}] = \text{Tr}[\tilde{\mathcal{S}}_{AA'}^{(2)}(\hat{\rho}_A^{(1)} \otimes \hat{\rho}_{A'}^{(2)})] \text{Tr}[\hat{\rho}_B^{(1)} \hat{\rho}_B^{(2)}], \quad (\text{C54})$$

where $\tilde{\mathcal{S}}_{AA'}^{(2)} = \text{Tr}_B[\mathbb{S}_{AA'} \rho_{AB} \mathbb{S}_{AA'} \rho_{AB}]$. The variance contribution $\overline{V}_2^{(1)}$ given by this set of permutations can be bound as

$$\overline{V}_2^{(1)} \leq \mathbb{E} \left[\text{Tr}[\tilde{\mathcal{S}}_{AA'}^{(2)}(\hat{\rho}_A^{(1)} \otimes \hat{\rho}_{A'}^{(2)})]^2 \text{Tr}[\hat{\rho}_B^{(1)} \hat{\rho}_B^{(2)}]^2 \right]. \quad (\text{C55})$$

To see this, we first use Lemma 1 to bound the original term as

$$\mathbb{E} \left[\text{Tr}[\tilde{\mathcal{S}}_{AA'}^{(2)}(\hat{\rho}_A^{(1)} \otimes \hat{\rho}_{A'}^{(2)})]^2 \text{Tr}[\hat{\rho}_B^{(1)} \hat{\rho}_B^{(2)}]^2 \right] \leq \mathbb{E} \left[\text{Tr}[\tilde{\mathcal{S}}_{AA'}^{(2)}(\hat{\rho}_A^{(1)} \otimes \hat{\rho}_{A'}^{(2)})]^2 \times \prod_{i=1}^{N_B} \left(5^2 \mathbf{1}_{\{\mathcal{B}_i = \mathcal{B}'_i\}} + \left(\frac{1}{2}\right)^2 \mathbf{1}_{\{\mathcal{B}_i \neq \mathcal{B}'_i\}} \right) \right]. \quad (\text{C56})$$

As the Pauli basis chosen for subsystem B is independent with respect to the shadows in subsystem A , we can factorize the expectation value further:

$$\begin{aligned} & \mathbb{E} \left[\text{Tr}[\tilde{\mathcal{S}}_{AA'}^{(2)}(\hat{\rho}_A^{(1)} \otimes \hat{\rho}_{A'}^{(2)})]^2 \right] \times \prod_{i=1}^{N_B} \left(5^2 \mathbf{1}\{\mathcal{B}_i = \mathcal{B}'_i\} + \left(\frac{1}{2}\right)^2 \mathbf{1}\{\mathcal{B}_i \neq \mathcal{B}'_i\} \right) \\ &= \mathbb{E} \left[\text{Tr}[\tilde{\mathcal{S}}_{AA'}^{(2)}(\hat{\rho}_A^{(1)} \otimes \hat{\rho}_{A'}^{(2)})]^2 \right] \times \mathbb{E} \left[\prod_{i=1}^{N_B} \left(5^2 \mathbf{1}\{\mathcal{B}_i = \mathcal{B}'_i\} + \left(\frac{1}{2}\right)^2 \mathbf{1}\{\mathcal{B}_i \neq \mathcal{B}'_i\} \right) \right]. \end{aligned} \quad (\text{C57})$$

Now, the first expectation term can be bound by reinterpreting $\hat{\rho}_A^{(1)} \otimes \hat{\rho}_{A'}^{(2)}$ as a classical shadow in a 2^{2N_A} -dimensional Hilbert space and applying Lemma 2. The second expectation value is bounded directly by Lemma 1. Combining both upper bounds then produces

$$\overline{V_2^{(1)}} \leq \text{Tr}[(\tilde{\mathcal{S}}_{AA'}^{(2)})^2] 2^{2N_A} 8.5^{N_B}. \quad (\text{C58})$$

Noting that the operator $\tilde{\mathcal{S}}_{AA'}^{(2)}$ is Hermitian and rewriting it as $\text{Tr}[(\tilde{\mathcal{S}}_{AA'}^{(2)})^2] = \text{Tr}(\mathcal{S} \rho_{AB}^{\otimes 4})$, where \mathcal{S} is a unitary operator, we can again apply Hölder's inequality for matrices to obtain

$$\text{Tr}[(\tilde{\mathcal{S}}_{AA'}^{(2)})^2] = \text{Tr}(\mathcal{S} \rho_{AB}^{\otimes 4}) \leq \|\mathcal{S}\|_\infty \|\rho_{AB}^{\otimes 4}\|_1 = 1 \times 1 = 1. \quad (\text{C59})$$

Thus, the final bound on $\overline{V_2^{(1)}}$ can be written as

$$\overline{V_2^{(1)}} \leq 2^{2N_A} 8.5^{N_B}. \quad (\text{C60})$$

- (2) If $\pi[\hat{\rho}^{(1)} \otimes \hat{\rho}^{(2)} \otimes \rho_{AB} \otimes \rho_{AB}]\pi^\dagger = \hat{\rho}^{(1)} \otimes \rho_{AB} \otimes \rho_{AB} \otimes \hat{\rho}^{(2)}$ or $\rho_{AB} \otimes \hat{\rho}^{(1)} \otimes \hat{\rho}^{(2)} \otimes \rho_{AB}$, or with the indices 1 and 2 exchanged on the right-hand sides, we obtain [cf. Fig. 8(b)]

$$\text{Tr}[\mathcal{S} \pi[\hat{\rho}^{(1)} \otimes \hat{\rho}^{(2)} \otimes \rho_{AB} \otimes \rho_{AB}]\pi^\dagger] = \text{Tr}[\tilde{\mathcal{S}}_{BB'}^{(2)}(\hat{\rho}_B^{(1)} \otimes \hat{\rho}_{B'}^{(2)})] \text{Tr}[\hat{\rho}_A^{(1)} \hat{\rho}_A^{(2)}], \quad (\text{C61})$$

where $\tilde{\mathcal{S}}_{BB'}^{(2)} = \text{Tr}_A[\mathbb{S}_{BB'} \rho_{AB} \mathbb{S}_{BB'} \rho_{AB}]$. This expression is similar to the previous one, with the roles of A and B exchanged. By following the same thread of arguments as in the previous case, we can express the final bound as

$$\overline{V_2^{(2)}} := \text{Var} \left[\text{Tr}[\mathcal{S} \pi[\hat{\rho}^{(1)} \otimes \hat{\rho}^{(2)} \otimes \rho_{AB} \otimes \rho_{AB}]\pi^\dagger] \right] \leq 2^{2N_B} 8.5^{N_A}. \quad (\text{C62})$$

- (3) If $\pi[\hat{\rho}^{(1)} \otimes \hat{\rho}^{(2)} \otimes \rho_{AB} \otimes \rho_{AB}]\pi^\dagger = \hat{\rho}^{(1)} \otimes \rho_{AB} \otimes \hat{\rho}^{(2)} \otimes \rho_{AB}$ or $\rho_{AB} \otimes \hat{\rho}^{(1)} \otimes \rho_{AB} \otimes \hat{\rho}^{(2)}$, or with the indices 1 and 2 exchanged on the right-hand sides, then [cf. Fig. 8(c)]

$$\text{Tr}[\mathcal{S} \pi[\hat{\rho}^{(1)} \otimes \hat{\rho}^{(2)} \otimes \rho_{AB} \otimes \rho_{AB}]\pi^\dagger] = \text{Tr}[(\hat{\rho}_A^{(1)} \otimes \hat{\rho}_B^{(2)}) \rho_{AB}] \text{Tr}[(\hat{\rho}_A^{(2)} \otimes \hat{\rho}_B^{(1)}) \rho_{AB}]. \quad (\text{C63})$$

Directly using Lemma 4, it then follows in this third case that

$$\overline{V_2^{(3)}} := \text{Var} \left[\text{Tr}[\mathcal{O}^{(4)} \pi[\hat{\rho}^{(1)} \otimes \hat{\rho}^{(2)} \otimes \rho_{AB} \otimes \rho_{AB}]\pi^\dagger] \right] \leq \text{Tr}(\rho_{AB}^2) 2^{2N} \leq 2^{2N}, \quad (\text{C64})$$

because $\text{Tr}(\rho_{AB}^2)$ denotes the purity of ρ_{AB} , which can never exceed 1.

Combining the above three cases and incorporating them into Eq. (C29), we finally obtain

$$\overline{V_2} \leq \frac{1}{3} \left(\overline{V_2^{(1)}} + \overline{V_2^{(2)}} + \overline{V_2^{(3)}} \right) \leq \frac{1}{3} \left(2^{2N_A} 8.5^{N_B} + 2^{2N_B} 8.5^{N_A} + 2^{2N} \right) \leq 8.5^N \leq 3^{2N}. \quad (\text{C65})$$

Again, the last inequality ($8.5^N \leq 3^{2N}$) is rather loose but simplifies putting all the bounds together in the end.

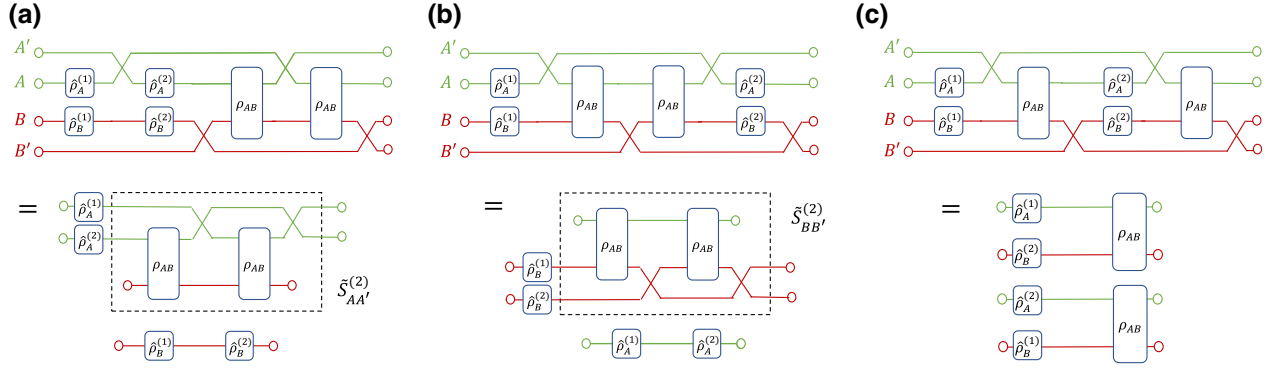


FIG. 8. The diagrammatic expression of the relevant terms for $k=2$: (a) $\text{Tr}[\mathcal{S}(\hat{\rho}^{(1)} \otimes \hat{\rho}^{(2)} \otimes \rho_{AB}^{\otimes 2})] = \text{Tr}[\tilde{\mathcal{S}}_{AA'}^{(2)}(\hat{\rho}_A^{(1)} \otimes \hat{\rho}_A^{(2)})] \text{Tr}[\hat{\rho}_B^{(1)} \hat{\rho}_B^{(2)}]$ as in Eq. (C54), (b) $\text{Tr}[\mathcal{S}(\hat{\rho}^{(1)} \otimes \rho_{AB}^{\otimes 2} \otimes \hat{\rho}^{(2)})] = \text{Tr}[\tilde{\mathcal{S}}_{BB'}^{(2)}(\hat{\rho}_B^{(1)} \otimes \hat{\rho}_B^{(2)})] \text{Tr}[\hat{\rho}_A^{(1)} \hat{\rho}_A^{(2)}]$ as in Eq. (C61), and (c) $\text{Tr}[\mathcal{S}(\hat{\rho}^{(1)} \otimes \rho_{AB} \otimes \hat{\rho}^{(2)} \otimes \rho_{AB})] = \text{Tr}[(\hat{\rho}_A^{(1)} \otimes \hat{\rho}_B^{(2)}) \rho_{AB}] \text{Tr}[(\hat{\rho}_A^{(2)} \otimes \hat{\rho}_B^{(1)}) \rho_{AB}]$ as in Eq. (C63).

(c) For $k=3$, $\overline{\mathcal{V}}_3$ contains 3 distinct shadows $\hat{\rho}^{(1)} = \hat{\rho}_A^{(1)} \otimes \hat{\rho}_B^{(1)}$, $\hat{\rho}^{(2)} = \hat{\rho}_A^{(2)} \otimes \hat{\rho}_B^{(2)}$, $\hat{\rho}^{(3)} = \hat{\rho}_A^{(3)} \otimes \hat{\rho}_B^{(3)}$ and a single density matrix ρ_{AB} . We note that regardless of π , we always obtain the same expression up to permuting the indices of the shadows for the traces in Eq. (C29). Thus, considering the term for $\pi = \mathbb{I}$ in Eq. (C29) is enough. This choice produces

$$\text{Tr}[\mathcal{S}[\hat{\rho}^{(1)} \otimes \hat{\rho}^{(2)} \otimes \hat{\rho}^{(3)} \otimes \rho_{AB}]] = \text{Tr}[\hat{\rho}_A^{(2)} \hat{\rho}_A^{(3)}] \text{Tr}[\hat{\rho}_B^{(1)} \hat{\rho}_B^{(2)}] \text{Tr}[(\hat{\rho}_A^{(1)} \otimes \hat{\rho}_B^{(3)}) \rho_{AB}], \quad (\text{C66})$$

cf. Fig. 9(a). The corresponding variance term can be bounded as

$$\overline{\mathcal{V}}_3 \leq \mathbb{E} \left[\text{Tr}[\hat{\rho}_A^{(2)} \hat{\rho}_A^{(3)}]^2 \text{Tr}[\hat{\rho}_B^{(1)} \hat{\rho}_B^{(2)}]^2 \text{Tr}[(\hat{\rho}_A^{(1)} \otimes \hat{\rho}_B^{(3)}) \rho_{AB}]^2 \right]. \quad (\text{C67})$$

To see this, we first use Lemma 1 twice to write

$$\overline{\mathcal{V}}_3 \leq \mathbb{E} \left[\prod_{i=1}^{N_A} \left(5^2 \mathbf{1}_{\{\mathcal{B}_i = \mathcal{B}'_i\}} + \left(\frac{1}{2}\right)^2 \mathbf{1}_{\{\mathcal{B}_i \neq \mathcal{B}'_i\}} \right) \prod_{i=1}^{N_B} \left(5^2 \mathbf{1}_{\{\mathcal{B}_i = \mathcal{B}'_i\}} + \left(\frac{1}{2}\right)^2 \mathbf{1}_{\{\mathcal{B}_i \neq \mathcal{B}'_i\}} \right) \text{Tr}[(\hat{\rho}_A^{(1)} \otimes \hat{\rho}_B^{(3)}) \rho_{AB}]^2 \right] \quad (\text{C68})$$

As in the previous case of $k=2$, the measurement bases of subsystems A and B are chosen independent from everything else (including each other). We can use this statistical independence to factorize the remaining expectation values and bound $\overline{\mathcal{V}}_3$ by the following expression:

$$\mathbb{E} \left[\prod_{i=1}^{N_A} \left(5^2 \mathbf{1}_{\{\mathcal{B}_i = \mathcal{B}'_i\}} + \left(\frac{1}{2}\right)^2 \mathbf{1}_{\{\mathcal{B}_i \neq \mathcal{B}'_i\}} \right) \right] \mathbb{E} \left[\prod_{j=1}^{N_B} \left(5^2 \mathbf{1}_{\{\mathcal{B}_j = \mathcal{B}'_j\}} + \left(\frac{1}{2}\right)^2 \mathbf{1}_{\{\mathcal{B}_j \neq \mathcal{B}'_j\}} \right) \right] \mathbb{E} \left[\text{Tr}[(\hat{\rho}_A^{(1)} \otimes \hat{\rho}_B^{(3)}) \rho_{AB}]^2 \right]. \quad (\text{C69})$$

Now, with Lemma 1, we bound the first two expectation terms by 8.5^{N_A} and 8.5^{N_B} , respectively. The third term can be controlled using Lemma 2. This finally results in

$$\overline{\mathcal{V}}_3 \leq 8.5^{N_A} 8.5^{N_B} \text{Tr}(\rho_{AB}^2) 2^N \leq 3^{3N}, \quad (\text{C70})$$

where we once more use the fact that the purity obeys $\text{Tr}(\rho_{AB}^2) \leq 1$.

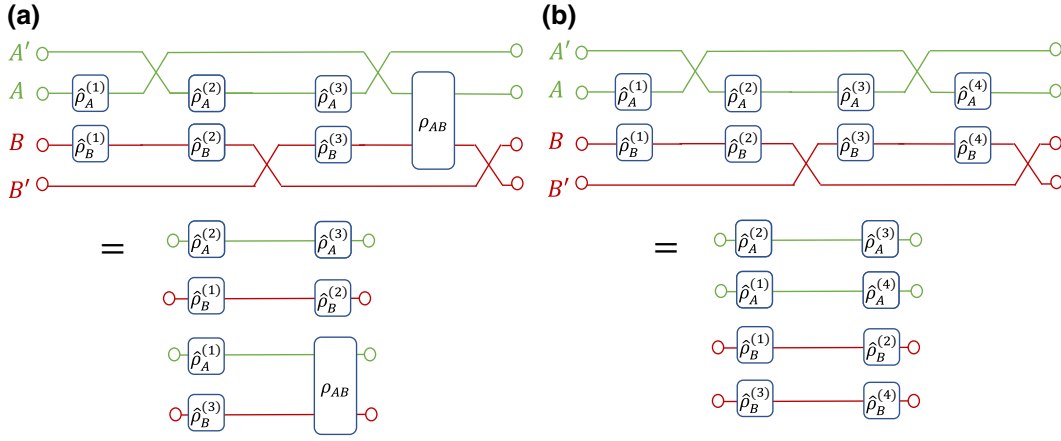


FIG. 9. Tensor diagrams for the case $k = 3$. (a) A graphical representation for the term in Eq. (C66). (b) A representation for the term for $k = 4$ shadows as in Eq. (C71).

- (d) For $k = 4$, the variance term \overline{V}_4 is composed of four distinct shadows $\hat{\rho}^{(1)}$, $\hat{\rho}^{(2)}$, $\hat{\rho}^{(3)}$ and $\hat{\rho}^{(4)}$. Considering the term for $\pi = \mathbb{I}$ in Eq. (C29), we obtain

$$\text{Tr}\left[\mathcal{S}[\hat{\rho}^{(1)} \otimes \hat{\rho}^{(2)} \otimes \hat{\rho}^{(3)} \otimes \hat{\rho}^{(4)}]\right] = \text{Tr}[\hat{\rho}_A^{(2)} \hat{\rho}_A^{(3)}] \text{Tr}[\hat{\rho}_A^{(1)} \hat{\rho}_A^{(4)}] \text{Tr}[\hat{\rho}_B^{(1)} \hat{\rho}_B^{(2)}] \text{Tr}[\hat{\rho}_B^{(3)} \hat{\rho}_B^{(4)}], \quad (\text{C71})$$

cf. Fig. 9(b). For other permutations π , we obtain the same kinds of expressions, up to permuting the indices of the shadows (which does not affect the overall expectation value). We can bound this term by

$$\overline{V}_4 \leq \mathbb{E}\left[\text{Tr}[\hat{\rho}_A^{(2)} \hat{\rho}_A^{(3)}]^2 \text{Tr}[\hat{\rho}_A^{(1)} \hat{\rho}_A^{(4)}]^2 \text{Tr}[\hat{\rho}_B^{(1)} \hat{\rho}_B^{(2)}]^2 \text{Tr}[\hat{\rho}_B^{(3)} \hat{\rho}_B^{(4)}]^2\right]. \quad (\text{C72})$$

Indeed, each trace term in the above expectation can be controlled using Lemma 1. Noting that each measurement basis on subsystem A is sampled independent from the ones in B (and each other) for the four shadows concerned, we can factorize the above expectation value and obtain

$$\overline{V}_4 \leq \mathbb{E}\left[\prod_{i=1}^{N_A} \left(5^2 \mathbf{1}\{\mathcal{B}_i = \mathcal{B}'_i\} + \left(\frac{1}{2}\right)^2 \mathbf{1}\{\mathcal{B}_i \neq \mathcal{B}'_i\}\right)\right]^2 \mathbb{E}\left[\prod_{j=1}^{N_B} \left(5^2 \mathbf{1}\{\mathcal{B}_j = \mathcal{B}'_j\} + \left(\frac{1}{2}\right)^2 \mathbf{1}\{\mathcal{B}_j \neq \mathcal{B}'_j\}\right)\right]^2 \quad (\text{C73})$$

$$\leq 8.5^{2N_A} 8.5^{2N_B} \leq 3^{4N}. \quad (\text{C74})$$

We have now put all the pieces together to combine the results from the above case studies to obtain a compact expression for the variance of $\hat{X}_4^{(4)}$. More precisely, we use the following loose bound for each k : $\overline{V}_k \leq 3^{kN}$. Using Eq. (C47), we obtain

$$\text{Var}[\hat{X}_4^{(4)}] \leq \sum_{k=1}^4 \binom{4}{k} \frac{4^k}{M^k} \overline{V}_k \leq \sum_{k=1}^4 \binom{4}{k} 4^k \frac{3^{kN}}{M^k} = \left(1 + 4 \frac{3^N}{M}\right)^4 - 1. \quad (\text{C75})$$

Chebyshev's inequality in Eq. (C20) helps us to provide a sample complexity for this estimator.

Proposition 8: Let ρ_{AB} be a bipartite quantum state on $N = N_A + N_B$ qubits and suppose that we wish to estimate the non-linear function $X_4 = \text{Tr}(\mathcal{S}\rho_{AB}^{\otimes 4})$, with $\mathcal{S} = \mathbb{S}_{1,4}^{(A)} \otimes \mathbb{S}_{2,3}^{(A)} \otimes \mathbb{S}_{1,2}^{(B)} \otimes \mathbb{S}_{3,4}^{(B)}$, using the batch-shadow estimator $\tilde{X}_4^{(4)}$ constructed from Pauli shadows. Then, for $\epsilon, \delta > 0$, a total of

$$M \geq 4 \frac{3^N}{(1 + \epsilon^2 \delta)^{\frac{1}{4}} - 1} \gtrsim 16 \frac{3^N}{\epsilon^2 \delta} \quad (\text{C76})$$

measurements suffices to ensure that $\Pr[|\tilde{X}_4^{(4)} - X_4| \geq \epsilon] \leq \delta$.

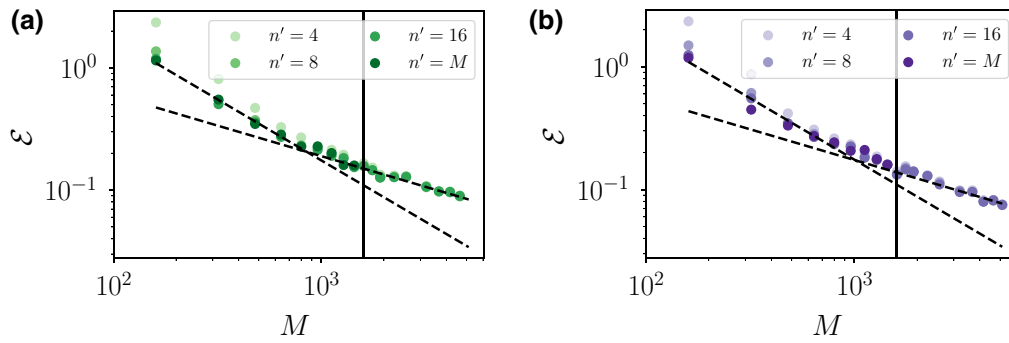


FIG. 10. The error scaling as a function of M , (a) for Pauli shadows and (b) for Haar shadows, showing the scaling of the average statistical error \mathcal{E} as a function of the number of measurements M for the functional $\tilde{X}_4^{(n')}$ calculated on a four-qubit GHZ state for different values of n' . The black line marks the value of M up to which we can simulate $\tilde{X}_4^{(M)}$. The dashed black lines highlight the different error scalings $\propto 1/M$ and $1/\sqrt{M}$.

This measurement cost scales (at worst) as 3^N in system size N and provides a scaling of $M \propto 3^N/\sqrt{\epsilon}$ for any given value of ϵ . Although the above measurement bound is loose, this scaling still offers an exponential improvement over the best-known scaling $\mathcal{O}(4^N/\sqrt{\epsilon})$ for the U-statistics estimate of X_4 in the case of Pauli shadow tomography in Ref. [65]. These improvements on the complexity bounds are achieved by exploiting the rich structure of Pauli-basis measurements to produce powerful auxiliary statements, most notably Lemmas 1 and 3. At the present stage, these auxiliary results are only valid for Pauli shadows and do not yet cover Haar shadows. We leave an extension of these arguments, and by extension Proposition 8, as an interesting topic for future work.

It is interesting to point out that the measurement-complexity bound X_4 is always comparable to the measurement-complexity bound for X_2 (purity). Moving from a second-order function to a fourth-order function does not seem to incur a large penalty in measurement complexity.

We equally note that, in the limit of $M \rightarrow \infty$, the dominant contribution to the variance is given by the linear term ($k = 1$), which scales $\propto 2^N/M$ as given by Eq. (C53). Then, in this limit, it holds that the measurement bound scales as $2^N/\epsilon^2\delta$.

5. Numerical investigations

In this section, we would like to devote ourselves to supporting our analytical findings with numerical simulation of the protocol. We would mainly like to study error scalings and the performance of the batch-shadow estimator $\tilde{X}_4^{n'}$ by using random Pauli and Haar-random shadows in the regime where $M \gg n'$ and compare it to the standard U-statistics estimator \hat{X}_n . We consider a four-qubit Greenberger-Horne-Zeilinger (GHZ) state and numerically simulate the protocol by applying M Haar-random (CUE) unitaries u followed by fixed-basis measurements to construct Haar-random shadows (fixing $N_M = 1$). We also construct numerically M Pauli shadows by choosing N random Pauli bases for each shadow. We calculate the average statistical error $\mathcal{E} = |\overline{\tilde{X}_4^{n'}} - X_4|/X_4$ for different values of n' and M by simulating the randomized-measurement protocol 200 times. This is plotted in Fig. 10 for Pauli and Haar shadows, respectively. We make two important observations:

- (a) The error scaling behavior of Pauli shadows, which involves sampling from a fixed set of three measurement settings, is not very different compared to that of the Haar shadows, which uses infinitely many measurement settings.
- (b) The batch-shadow estimator $\tilde{X}_4^{(n')}$ with $n' \sim 10$ has very close performance to that of the U-statistics estimator. In general, this translates into a huge run-time gain in terms of data treatment ($\mathcal{O}(10^4)$ compared to $\mathcal{O}(M^4)$) and allows us to process the quantities of interest for a larger set of measurement data. We clearly observe a limitation in postprocessing the U-statistics estimator ($n' = M$) for a modest system size of $N = 4$ qubits. This constraint starts to be extremely prominent when the system size N increases. This is due to the fact that M scales exponentially with N , as shown in the previous section.

APPENDIX D: EXPERIMENTAL PLATFORM AND THEORETICAL MODELING

The experimental platform in Ref. [7] is realized with trapped $^{40}\text{Ca}^+$ atoms, each one encoding a single qubit. Coupling all ions off resonantly with a laser beam subjects the ions to realizing the long-range Ising model in the presence of a transverse field, the effective Hamiltonian of which can be written as

$$H = \hbar \sum_{i < j} J_{ij} \sigma_i^x \sigma_j^x + \hbar B \sum_i \sigma_i, \quad (\text{D1})$$

where $i, j = 1, \dots, N$ and N is the total system size. To model the experiment using numerical simulations, we approximate the interaction matrix J_{ij} as a power law $J_{ij} = J_0/|i-j|^\alpha$, where the values of J_0 and α depend on the specifics of each experimental realization. For the experiments conducted with strings of 10 ions, $\alpha = 1.24$ and $J_0 = 420 \text{ s}^{-1}$. For those with 20 ions, $\alpha = 1.01$ and $J_0 = 370 \text{ s}^{-1}$. The effective magnetic field B is considered to be much larger than the interaction term ($B \simeq 22J_0$) such that terms that would break the conservation of the total magnetization, i.e., $\sigma_i^+ \sigma_j^+ + \text{h.c.}$, are energetically suppressed. The effects of decoherence on the system are taken into account considering the time evolution subject to local spin flips and spin-excitation loss. The full-system dynamics are described according to a Gorini-Kossakowski-Sudarshan-Lindblad (GKSL) master equation, the $2N$ local jump operators of which are written as $C_i = \sqrt{\gamma_x} \sigma_i^x$ (spin flip) and $C_{i+L} = \sqrt{\gamma_m} \sigma_i^-$ (excitation loss), $i = 1, \dots, L$, with rates γ_x and γ_m . Furthermore, the experimentally prepared state is not pure. As such, it can be written as the following mixed-product state $\rho_0 = \bigotimes_i (p_i |\uparrow\rangle\langle\uparrow| + (1-p_i) |\downarrow\rangle\langle\downarrow|)$, with $p_i \approx 0.004$ for i even and $p_i \approx 0.995$ for i odd.

In the experiment, local depolarizing noise is acting during the application of the local random unitary. We model it as

$$\rho(\bar{t}) \rightarrow (1 - p_{\text{DP}} N) \rho(\bar{t}) + p_{\text{DP}} \sum_i \text{Tr}_i[\rho(\bar{t})] \otimes \frac{\mathbb{I}_i}{2}, \quad (\text{D2})$$

where $p_{\text{DP}} \approx 0.02$ and \bar{t} denotes the time at which the measurement is performed.

In the case of the 20-ion experiment, the numerical simulations are done using tensor-network algorithms. For the unitary part of the dynamics, we approximate the interaction matrix J_{ij} as a sum of three exponentially decaying terms, which can efficiently be represented as MPOs. To treat the decoherence, we use quantum trajectories [129], applying the quantum jumps C_i to the state approximated as an MPS with bond dimension 128. The latter is evolved according to the time-dependent variational principle (TDVP) [130]. We average our results on 1500 trajectories in total.

APPENDIX E: BATCH SHADOWS TO EXTRACT RÉNYI 2-OE AND ITS SYMMETRY RESOLUTION

We use the batch-shadow estimator to access the Rényi 2-OE and its symmetry resolution from experimental data. The estimator of Rényi 2-OE $\tilde{S}^{(2)}$ constructed using n' batches can be explicitly written following Eq. (16), as

$$\tilde{S}^{(2)} = -\log \frac{\tilde{X}_4^{(n')}}{(\tilde{X}_2^{(n')})^2} = -\log \frac{\frac{1}{4!} \binom{n'}{4}^{-1} \sum_{b_1 \neq \dots \neq b_4} \text{Tr} \left[\mathcal{S} \otimes_{i=1}^4 \tilde{\rho}^{(b_i)} \right]}{\left(\frac{1}{2!} \binom{n'}{2}^{-1} \sum_{b_1 \neq b_2} \text{Tr} \left[\mathbb{S}_{1,2}^{(\text{AB})} \otimes_{i=1}^2 \tilde{\rho}^{(b_i)} \right] \right)^2}. \quad (\text{E1})$$

To estimate the Rényi 2-OE from the experimental data as shown in the main text, we use the simple estimator with $n' = 4$. Alternatively, the symmetry resolution for the Rényi 2-OE can be expressed as

$$S_q^{(2)} = -\log \frac{\text{Tr} \left(\left[\Pi_q \text{Tr}_B(|\rho_{\text{AB}}\rangle\langle\rho_{\text{AB}}|) \Pi_q \right]^2 \right)}{p(q)^2 \text{Tr}(\rho_{\text{AB}}^2)} = -\log \frac{\text{Tr} \left(\left[\Pi_q \text{Tr}_B(|\rho_{\text{AB}}\rangle\langle\rho_{\text{AB}}|) \Pi_q \right]^2 \right)}{\text{Tr}(\Pi_q \text{Tr}_B(|\rho_{\text{AB}}\rangle\langle\rho_{\text{AB}}|))^2}, \quad (\text{E2})$$

where Π_q is the projector onto the eigenspace of the symmetry sector q for system A and $p(q) = \text{Tr}(\Pi_q \text{Tr}_B(|\rho_{\text{AB}}\rangle\langle\rho_{\text{AB}}|)) / \text{Tr}(\rho_{\text{AB}}^2)$ are the probabilities of being in the charge sector q expressed in terms of a fraction of two second-order functions. As $\mathbb{E}[\tilde{\rho}^{(b_i)}] = \rho_{\text{AB}}$ for all batch shadows, we can obtain a batch estimator of the symmetry-resolved Rényi 2-OE by replacing each vectorized density matrix by a distinct batch shadow. First, we can express

the estimator of the populations $\tilde{p}(q)$ as

$$\tilde{p}(q) = \frac{\frac{1}{2!} \binom{n'}{2}^{-1} \sum_{b_1 \neq b_2} \text{Tr}(\Pi_q \text{Tr}_B(|\tilde{\rho}^{(b_1)}\rangle\langle\tilde{\rho}^{(b_2)}|))}{\tilde{X}_2^{(n')}}. \quad (\text{E3})$$

We can now explicitly write the estimator $\tilde{S}_q^{(2)}$ of SR Rényi 2-OE as

$$\tilde{S}_q^{(2)} = -\log \frac{\frac{1}{4!} \binom{n'}{4}^{-1} \sum_{b_1 \neq \dots \neq b_4} \text{Tr}(\Pi_q \text{Tr}_B(|\tilde{\rho}^{(b_1)}\rangle\langle\tilde{\rho}^{(b_2)}|) \Pi_q \text{Tr}_B(|\tilde{\rho}^{(b_3)}\rangle\langle\tilde{\rho}^{(b_4)}|))}{\left(\frac{1}{2!} \binom{n'}{2}^{-1} \sum_{b_1 \neq b_2} \text{Tr}(\Pi_q \text{Tr}_B(|\tilde{\rho}^{(b_1)}\rangle\langle\tilde{\rho}^{(b_2)}|))\right)^2}. \quad (\text{E4})$$

The SR Rényi 2-OE are extracted from the experimental data by taking $n' = 16$.

-
- [1] R. Blatt and C. F. Roos, Quantum simulations with trapped ions, *Nat. Phys.* **8**, 277 (2012).
- [2] C. Monroe, W. C. Campbell, L.-M. Duan, Z.-X. Gong, A. V. Gorshkov, P. Hess, R. Islam, K. Kim, N. M. Linke, G. Pagano, P. Richerme, C. Senko, and N. Y. Yao, Programmable quantum simulations of spin systems with trapped ions, *Rev. Mod. Phys.* **93**, 025001 (2021).
- [3] A. Browaeys and T. Lahaye, Many-body physics with individually controlled Rydberg atoms, *Nat. Phys.* **16**, 132 (2020).
- [4] L. K. Joshi, A. Elben, A. Vikram, B. Vermersch, V. Galitski, and P. Zoller, Probing Many-Body Quantum Chaos with Quantum Simulators, *Phys. Rev. X* **12**, 011018 (2022).
- [5] A. M. Kaufman, M. E. Tai, A. Lukin, M. Rispoli, R. Schittko, P. M. Preiss, and M. Greiner, Quantum thermalization through entanglement in an isolated many-body system, *Science* **353**, 794 (2016).
- [6] J. Vovrosh and J. Knolle, Confinement and entanglement dynamics on a digital quantum computer, *Sci. Rep.* **11**, 1 (2021).
- [7] T. Brydges, A. Elben, P. Jurcevic, B. Vermersch, C. Maier, B. P. Lanyon, P. Zoller, R. Blatt, and C. F. Roos, Probing Rényi entanglement entropy via randomized measurements, *Science* **364**, 260 (2019).
- [8] A. Elben, R. Kueng, H.-Y. R. Huang, R. van Bijnen, C. Kokail, M. Dalmonte, P. Calabrese, B. Kraus, J. Preskill, P. Zoller, and B. Vermersch, Mixed-State Entanglement from Local Randomized Measurements, *Phys. Rev. Lett.* **125**, 200501 (2020).
- [9] K. J. Satzinger, Y. Liu, A. Smith, C. Knapp, M. Newman, C. Jones, Z. Chen, C. Quintana, X. Mi, A. Dunsworth *et al.*, Realizing topologically ordered states on a quantum processor, *Science* **374**, 1237 (2021).
- [10] J. Li, R. Fan, H. Wang, B. Ye, B. Zeng, H. Zhai, X. Peng, and J. Du, Measuring Out-of-Time-Order Correlators on a Nuclear Magnetic Resonance Quantum Simulator, *Phys. Rev. X* **7**, 031011 (2017).
- [11] M. Gärttner, J. G. Bohnet, A. Safavi-Naini, M. L. Wall, J. J. Bollinger, and A. M. Rey, Measuring out-of-time-order correlations and multiple quantum spectra in a trapped-ion quantum magnet, *Nat. Phys.* **13**, 781 (2017).
- [12] K. A. Landsman, C. Figgatt, T. Schuster, N. M. Linke, B. Yoshida, N. Y. Yao, and C. Monroe, Verified quantum information scrambling, *Nature* **567**, 61 (2019).
- [13] M. K. Joshi, A. Elben, B. Vermersch, T. Brydges, C. Maier, P. Zoller, R. Blatt, and C. F. Roos, Quantum Information Scrambling in a Trapped-Ion Quantum Simulator with Tunable Range Interactions, *Phys. Rev. Lett.* **124**, 240505 (2020).
- [14] X. Mi, P. Roushan, C. Quintana, S. Mandra, J. Marshall, C. Neill, F. Arute, K. Arya, J. Atalaya, R. Babbush *et al.*, Information scrambling in quantum circuits, *Science* **374**, 1479 (2021).
- [15] Tensor networks for complex quantum systems, *Nat. Rev. Phys.* **1**, 538 (2019).
- [16] G. Vidal, Efficient Simulation of One-Dimensional Quantum Many-Body Systems, *Phys. Rev. Lett.* **93**, 040502 (2004).
- [17] F. Verstraete, V. Murg, and J. Cirac, Matrix product states, projected entangled pair states, and variational renormalization group methods for quantum spin systems, *Adv. Phys.* **57**, 143 (2008).
- [18] U. Schollwöck, The density-matrix renormalization group in the age of matrix product states, *Ann. Phys.* **326**, 96 (2011).
- [19] S. Paeckel, T. Köhler, A. Swoboda, S. R. Manmana, U. Schollwöck, and C. Hubig, Time-evolution methods for matrix-product states, *Ann. Phys.* **411**, 167998 (2019).
- [20] P. Calabrese and J. Cardy, Evolution of entanglement entropy in one-dimensional systems, *J. Stat. Mech.* **2005**, P04010 (2005).
- [21] V. Alba and P. Calabrese, Entanglement and thermodynamics after a quantum quench in integrable systems, *PNAS* **114**, 7947 (2017).
- [22] N. Schuch, M. M. Wolf, F. Verstraete, and J. I. Cirac, Entropy Scaling and Simulability by Matrix Product States, *Phys. Rev. Lett.* **100**, 030504 (2008).
- [23] T. Barthel and U. Schollwöck, Dephasing and the Steady State in Quantum Many-Particle Systems, *Phys. Rev. Lett.* **100**, 100601 (2008).

- [24] M. Cramer, C. M. Dawson, J. Eisert, and T. J. Osborne, Exact Relaxation in a Class of Nonequilibrium Quantum Lattice Systems, *Phys. Rev. Lett.* **100**, 030602 (2008).
- [25] P. Calabrese, F. H. L. Essler, and M. Fagotti, Quantum Quench in the Transverse-Field Ising Chain, *Phys. Rev. Lett.* **106**, 227203 (2011).
- [26] T. Prosen and I. Pižorn, Operator space entanglement entropy in a transverse Ising chain, *Phys. Rev. A* **76**, 032316 (2007).
- [27] I. Pižorn and T. Prosen, Operator space entanglement entropy in XY spin chains, *Phys. Rev. B* **79**, 184416 (2009).
- [28] T. Zhou and D. J. Luitz, Operator entanglement entropy of the time evolution operator in chaotic systems, *Phys. Rev. B* **95**, 094206 (2017).
- [29] J. Dubail, Entanglement scaling of operators: A conformal field theory approach, with a glimpse of simulability of long-time dynamics in $1 + 1d$, *J. Phys. A* **50**, 234001 (2017).
- [30] K. Noh, L. Jiang, and B. Fefferman, Efficient classical simulation of noisy random quantum circuits in one dimension, *Quantum* **4**, 318 (2020).
- [31] T. Rakovszky, C. von Keyserlingk, and F. Pollmann, Dissipation-assisted operator evolution method for capturing hydrodynamic transport, *Phys. Rev. B* **105**, 075131 (2022).
- [32] D. Wellnitz, G. Preisser, V. Alba, J. Dubail, and J. Schachenmayer, The rise and fall, and slow rise again, of operator entanglement under dephasing, [arXiv:2201.05099](https://arxiv.org/abs/2201.05099) (2022).
- [33] O. Gühne and G. Tóth, Entanglement detection, *Phys. Rep.* **474**, 1 (2009).
- [34] P. Zanardi, C. Zalka, and L. Faoro, Entangling power of quantum evolutions, *Phys. Rev. A* **62**, 030301 (2000).
- [35] P. Zanardi, Entanglement of quantum evolutions, *Phys. Rev. A* **63**, 040304 (2001).
- [36] H. Wang and T. Zhou, Barrier from chaos: Operator entanglement dynamics of the reduced density matrix, *JHEP* **2019**, 20 (2019).
- [37] I. Reid and B. Bertini, Entanglement barriers in dual-unitary circuits, *Phys. Rev. B* **104**, 014301 (2021).
- [38] M. Rigol, V. Dunjko, and M. Olshanii, Thermalization and its mechanism for generic isolated quantum systems, *Nature* **452**, 854 (2008).
- [39] T. Mori, T. N. Ikeda, E. Kaminishi, and M. Ueda, Thermalization and prethermalization in isolated quantum systems: A theoretical overview, *J. Phys. B* **51**, 112001 (2018).
- [40] K. Mallayya, M. Rigol, and W. De Roeck, Prethermalization and Thermalization in Isolated Quantum Systems, *Phys. Rev. X* **9**, 021027 (2019).
- [41] J. M. Deutsch, Quantum statistical mechanics in a closed system, *Phys. Rev. A* **43**, 2046 (1991).
- [42] M. Srednicki, Chaos and quantum thermalization, *Phys. Rev. E* **50**, 888 (1994).
- [43] L. D'Alessio, Y. Kafri, A. Polkovnikov, and M. Rigol, From quantum chaos and eigenstate thermalization to statistical mechanics and thermodynamics, *Adv. Phys.* **65**, 239 (2016).
- [44] M. Rigol, V. Dunjko, V. Yurovsky, and M. Olshanii, Relaxation in a Completely Integrable Many-Body Quantum System: An *Ab Initio* Study of the Dynamics of the Highly Excited States of 1D Lattice Hard-Core Bosons, *Phys. Rev. Lett.* **98**, 050405 (2007).
- [45] M. Cramer and J. Eisert, A quantum central limit theorem for non-equilibrium systems: Exact local relaxation of correlated states, *New J. Phys.* **12**, 055020 (2010).
- [46] L. Vidmar and M. Rigol, Generalized Gibbs ensemble in integrable lattice models, *J. Stat. Mech.* **2016**, 064007 (2016).
- [47] P. Calabrese, F. H. L. Essler, and G. Mussardo, Introduction to quantum integrability in out of equilibrium systems, *J. Stat. Mech.* **2016**, 064001 (2016).
- [48] A. Elben, S. T. Flammia, H.-Y. Huang, R. Kueng, J. Preskill, B. Vermersch, and P. Zoller, The randomized measurement toolbox, [arXiv:2203.11374](https://arxiv.org/abs/2203.11374) (2022).
- [49] H.-Y. Huang, R. Kueng, and J. Preskill, Predicting many properties of a quantum system from very few measurements, *Nat. Phys.* **16**, 1050 (2020).
- [50] A. Rath, R. van Bijnen, A. Elben, P. Zoller, and B. Vermersch, Importance Sampling of Randomized Measurements for Probing Entanglement, *Phys. Rev. Lett.* **127**, 200503 (2021).
- [51] Y. Zhou, P. Zeng, and Z. Liu, Single-Copies Estimation of Entanglement Negativity, *Phys. Rev. Lett.* **125**, 200502 (2020).
- [52] A. Neven, J. Carrasco, V. Vitale, C. Kokail, A. Elben, M. Dalmonte, P. Calabrese, P. Zoller, B. Vermersch, R. Kueng, and B. Kraus, Symmetry-resolved entanglement detection using partial transpose moments, *Npj Quantum Inf.* **7**, 1 (2021).
- [53] V. Vitale, A. Elben, R. Kueng, A. Neven, J. Carrasco, B. Kraus, P. Zoller, P. Calabrese, B. Vermersch, and M. Dalmonte, Symmetry-resolved dynamical purification in synthetic quantum matter, *SciPost Phys.* **12**, 106 (2022).
- [54] A. Elben, B. Vermersch, R. Van Bijnen, C. Kokail, T. Brydges, C. Maier, M. K. Joshi, R. Blatt, C. F. Roos, and P. Zoller, Cross-Platform Verification of Intermediate Scale Quantum Devices, *Phys. Rev. Lett.* **124**, 10504 (2020).
- [55] D. Zhu, Z.-P. Cian, C. Noel, A. Risinger, D. Biswas, L. Egan, Y. Zhu, A. M. Green, C. H. Alderete, N. H. Nguyen, Q. Wang, A. Maksymov, Y. Nam, M. Cetina, N. M. Linke, M. Hafezi, and C. Monroe, Cross-platform comparison of arbitrary quantum computations, [arXiv:2107.11387](https://arxiv.org/abs/2107.11387) (2021).
- [56] D. Gross, Y.-K. Liu, S. T. Flammia, S. Becker, and J. Eisert, Quantum State Tomography via Compressed Sensing, *Phys. Rev. Lett.* **105**, 150401 (2010).
- [57] G. Torlai, G. Mazzola, J. Carrasquilla, M. Troyer, R. Melko, and G. Carleo, Neural-network quantum state tomography, *Nat. Phys.* **14**, 447 (2018).
- [58] G. Torlai, B. Timar, E. P. L. van Nieuwenburg, H. Levine, A. Omran, A. Keesling, H. Bernien, M. Greiner, V. Vuletić, M. D. Lukin, R. G. Melko, and M. Endres, Integrating Neural Networks with a Quantum Simulator for State Reconstruction, *Phys. Rev. Lett.* **123**, 230504 (2019).

- [59] C. Kokail, R. van Bijnen, A. Elben, B. Vermersch, and P. Zoller, Entanglement Hamiltonian tomography in quantum simulation, *Nat. Phys.* **17**, 936 (2021).
- [60] R. Kueng, H. Rauhut, and U. Terstiege, Low rank matrix recovery from rank one measurements, *Appl. Comput. Harmon. Anal.* **42**, 88 (2017).
- [61] R. O'Donnell and J. Wright, in *STOC'16—Proceedings of the 48th Annual ACM SIGACT Symposium on Theory of Computing* (Association for Computing Machinery, New York, 2016), p. 899.
- [62] J. Haah, A. W. Harrow, Z. Ji, X. Wu, and N. Yu, Sample-optimal tomography of quantum states, *IEEE Trans. Inf. Theory* **63**, 5628 (2017).
- [63] M. Guță, J. Kahn, R. Kueng, and J. A. Tropp, Fast state tomography with optimal error bounds, *J. Phys. A* **53**, 204001 (2020).
- [64] M. Paini and A. Kalev, An approximate description of quantum states, arXiv preprint [arXiv:1910.10543](https://arxiv.org/abs/1910.10543) (2019).
- [65] Z. Liu, Y. Tang, H. Dai, P. Liu, S. Chen, and X. Ma, Detecting entanglement in quantum many-body systems via permutation moments, [arXiv:2203.08391](https://arxiv.org/abs/2203.08391) (2022).
- [66] N. Laflorencie and S. Rachel, Spin-resolved entanglement spectroscopy of critical spin chains and Luttinger liquids, *J. Stat. Mech.* **2014**, P11013 (2014).
- [67] M. Goldstein and E. Sela, Symmetry-Resolved Entanglement in Many-Body Systems, *Phys. Rev. Lett.* **120**, 200602 (2018).
- [68] J. C. Xavier, F. C. Alcaraz, and G. Sierra, Equipartition of the entanglement entropy, *Phys. Rev. B* **98**, 041106 (2018).
- [69] G. Perez, R. Bonsignori, and P. Calabrese, Quasiparticle dynamics of symmetry-resolved entanglement after a quench: Examples of conformal field theories and free fermions, *Phys. Rev. B* **103**, L041104 (2021).
- [70] G. Perez, R. Bonsignori, and P. Calabrese, Exact quench dynamics of symmetry resolved entanglement in a free fermion chain, *J. Stat. Mech.* **2021**, 093102 (2021).
- [71] D. Azses, E. G. Dalla Torre, and E. Sela, Observing Floquet topological order by symmetry resolution, *Phys. Rev. B* **104**, L220301 (2021).
- [72] X. Turkeshe, P. Ruggiero, V. Alba, and P. Calabrese, Entanglement equipartition in critical random spin chains, *Phys. Rev. B* **102**, 014455 (2020).
- [73] S. Murciano, G. Di Giulio, and P. Calabrese, Entanglement and symmetry resolution in two dimensional free quantum field theories, *JHEP* **2020**, 1 (2020).
- [74] L. Capizzi and P. Calabrese, Symmetry resolved relative entropies and distances in conformal field theory, *JHEP* **2021**, 1 (2021).
- [75] S. Murciano, P. Ruggiero, and P. Calabrese, Symmetry resolved entanglement in two-dimensional systems via dimensional reduction, *J. Stat. Mech.* **2020**, 083102 (2020).
- [76] S. Murciano, G. D. Giulio, and P. Calabrese, Symmetry resolved entanglement in gapped integrable systems: A corner transfer matrix approach, *SciPost Phys.* **8**, 46 (2020).
- [77] S. Murciano, R. Bonsignori, and P. Calabrese, Symmetry decomposition of negativity of massless free fermions, *SciPost Phys.* **10**, 111 (2021).
- [78] S. Fraenkel and M. Goldstein, Entanglement measures in a nonequilibrium steady state: Exact results in one dimension, *SciPost Phys.* **11**, 85 (2021).
- [79] A. Lukin, M. Rispoli, R. Schittko, M. E. Tai, A. M. Kaufman, S. Choi, V. Khemani, J. Léonard, and M. Greiner, Probing entanglement in a many-body-localized system, *Science* **364**, 256 (2019).
- [80] G. Benenti, G. Casati, D. Rossini, and G. Strini, *Principles of Quantum Computation and Information: A Comprehensive Textbook* (World Scientific, Singapore, 2019).
- [81] A. Jamiolkowski, Linear transformations which preserve trace and positive semidefiniteness of operators, *Rep. Math. Phys.* **3**, 275 (1972).
- [82] M.-D. Choi, Completely positive linear maps on complex matrices, *Linear Algebra Appl.* **10**, 285 (1975).
- [83] O. Rudolph, A separability criterion for density operators, *J. Phys. A* **33**, 3951 (2000).
- [84] K. Chen and L.-A. Wu, A matrix realignment method for recognizing entanglement, *Quantum Inf. Comput.* **3**, 193 (2003).
- [85] O. Rudolph, Further results on the cross norm criterion for separability, *Quantum Inf. Process.* **4**, 219 (2005).
- [86] S. Chen, W. Yu, P. Zeng, and S. T. Flammia, Robust Shadow Estimation, *PRX Quantum* **2**, 030348 (2021).
- [87] D. E. Koh and S. Grewal, Classical shadows with noise, *Quantum* **6**, 776 (2022).
- [88] E. van den Berg, Z. K. Mineev, and K. Temme, Model-free readout-error mitigation for quantum expectation values, *Phys. Rev. A* **105**, 032620 (2022).
- [89] M. Cramer, M. B. Plenio, S. T. Flammia, R. Somma, D. Gross, S. D. Bartlett, O. Landon-Cardinal, D. Poulin, and Y.-K. Liu, Efficient quantum state tomography, *Nat. Commun.* **1**, 149 (2010).
- [90] A. Rath, C. Branciard, A. Minguzzi, and B. Vermersch, Quantum Fisher Information from Randomized Measurements, *Phys. Rev. Lett.* **127**, 260501 (2021).
- [91] B. Bertini, P. Kos, and T. Prosen, Operator entanglement in local quantum circuits I: Chaotic dual-unitary circuits, *SciPost Phys.* **8**, 67 (2020).
- [92] P. Hauke and L. Tagliacozzo, Spread of Correlations in Long-Range Interacting Quantum Systems, *Phys. Rev. Lett.* **111**, 207202 (2013).
- [93] P. Jurcevic, B. P. Lanyon, P. Hauke, C. Hempel, P. Zoller, R. Blatt, and C. F. Roos, Quasiparticle engineering and entanglement propagation in a quantum many-body system, *Nature* **511**, 202 (2014).
- [94] B. Bertini and P. Calabrese, Prethermalization and thermalization in entanglement dynamics, *Phys. Rev. B* **102**, 094303 (2020).
- [95] B. Bertini, F. H. L. Essler, S. Groha, and N. J. Robinson, Prethermalization and Thermalization in Models with Weak Integrability Breaking, *Phys. Rev. Lett.* **115**, 180601 (2015).
- [96] F. Ares, S. Murciano, and P. Calabrese, Entanglement asymmetry as a probe of symmetry breaking, [arXiv:2207.14693](https://arxiv.org/abs/2207.14693) (2022).
- [97] I. P. M. C. Chung, Density-matrix spectra of solvable fermionic systems, *Phys. Rev. B* **64**, 064412 (2001).
- [98] I. Peschel, Calculation of reduced density matrices from correlation functions, *J. Phys. A* **36**, 205 (2003).

- [99] E. Fradkin, *Field Theories of Condensed Matter Physics* (Cambridge University Press, Cambridge, 2013).
- [100] V. Alba and P. Calabrese, Entanglement dynamics after quantum quenches in generic integrable systems, *SciPost Phys.* **4**, 017 (2018).
- [101] P. Calabrese, Entanglement spreading in non-equilibrium integrable systems, *SciPost Phys. Lect. Notes*, **20** (2020).
- [102] P. Calabrese, Entanglement and thermodynamics in non-equilibrium isolated quantum systems, *Phys. A* **504**, 31 (2018).
- [103] S. Dutta and T. Faulkner, A canonical purification for the entanglement wedge cross-section, *JHEP* **3**, 178 (2021).
- [104] P. Bueno and H. Casini, Reflected entropy, symmetries and free fermions, *JHEP* **5**, 103 (2020).
- [105] P. Calabrese, J. Cardy, and E. Tonni, Entanglement Negativity in Quantum Field Theory, *Phys. Rev. Lett.* **109**, 130502 (2012).
- [106] P. Calabrese, J. Cardy, and E. Tonni, Entanglement negativity in extended systems: A field theoretical approach, *J. Stat. Mech.* **2013**, P02008 (2013).
- [107] V. Eisler and Z. Zimborás, On the partial transpose of fermionic Gaussian states, *New J. Phys.* **17**, 053048 (2015).
- [108] H. Shapourian, K. Shiozaki, and S. Ryu, Partial time-reversal transformation and entanglement negativity in fermionic systems, *Phys. Rev. B* **95**, 165101 (2017).
- [109] A. Leroose, M. Sonner, and D. A. Abanin, Influence Matrix Approach to Many-Body Floquet Dynamics, *Phys. Rev. X* **11**, 021040 (2021).
- [110] M. Sonner, A. Leroose, and D. A. Abanin, Influence functional of many-body systems: Temporal entanglement and matrix-product state representation, *Ann. Phys.* **431**, 168552 (2021).
- [111] G. Giudice, G. Giudici, M. Sonner, J. Thoenniss, A. Leroose, D. A. Abanin, and L. Piroli, Temporal Entanglement, Quasiparticles, and the Role of Interactions, *Phys. Rev. Lett.* **128**, 220401 (2022).
- [112] V. Alba and P. Calabrese, Quantum information dynamics in multipartite integrable systems, *EPL* **126**, 60001 (2019).
- [113] C. Jonay, D. A. Huse, and A. Nahum, Coarse-grained dynamics of operator and state entanglement, [arXiv:1803.00089](https://arxiv.org/abs/1803.00089) (2018).
- [114] V. Alba, J. Dubail, and M. Medenjak, Operator Entanglement in Interacting Integrable Quantum Systems: The Case of the Rule 54 Chain, *Phys. Rev. Lett.* **122**, 250603 (2019).
- [115] B. Bertini, P. Kos, and T. Prosen, Operator entanglement in local quantum circuits II: Solitons in chains of qubits, *SciPost Phys.* **8**, 068 (2020).
- [116] J. Johansson, P. Nation, and F. Nori, QuTiP 2: A PYTHON framework for the dynamics of open quantum systems, *Comput. Phys. Commun.* **184**, 1234 (2013).
- [117] T. Zhang, N. Jing, and S.-M. Fei, Quantum separability criteria based on realignment moments, *Quantum Inf. Process.* **21**, 276 (2022).
- [118] B. Berger, The fourth moment method, *SIAM J. Comput.* **26**, 1188 (1997).
- [119] W. Matthews, S. Wehner, and A. Winter, Distinguishability of quantum states under restricted families of measurements with an application to quantum data hiding, *Commun. Math. Phys.* **291**, 813 (2009).
- [120] C.-J. Zhang, Y.-S. Zhang, S. Zhang, and G.-C. Guo, Entanglement detection beyond the computable cross-norm or realignment criterion, *Phys. Rev. A* **77**, 060301 (2008).
- [121] Z. Liu, P. Zeng, Y. Zhou, and M. Gu, Characterizing correlation within multipartite quantum systems via local randomized measurements, *Phys. Rev. A* **105**, 022407 (2022).
- [122] H.-Y. Huang, R. Kueng, G. Torlai, V. V. Albert, and J. Preskill, Provably efficient machine learning for quantum many-body problems, [arXiv:2106.12627](https://arxiv.org/abs/2106.12627) (2021).
- [123] R. Stricker, M. Meth, L. Postler, C. Edmunds, C. Ferrie, R. Blatt, P. Schindler, T. Monz, R. Kueng, and M. Ringbauer, Experimental single-setting quantum state tomography, [arXiv:2206.00019](https://arxiv.org/abs/2206.00019) (2022).
- [124] W. Hoeffding, in *Breakthroughs in Statistics* (Springer, New York, 1992), p. 308.
- [125] L. Y. Hung and G. Wong, Entanglement branes and factorization in conformal field theory, *Phys. Rev. D* **104**, 026012 (2021).
- [126] J. Biamonte and V. Bergholm, Quantum tensor networks in a nutshell, [arXiv:1708.00006.pdf](https://arxiv.org/abs/1708.00006) (2017).
- [127] J. C. Bridgeman and C. T. Chubb, Hand-waving and interpretive dance: An introductory course on tensor networks, *J. Phys. A* **50**, 223001 (2017).
- [128] R. Kueng, Quantum and classical information processes with tensors (lecture notes) (2019), Caltech course notes, available at <https://iic.jku.at/files/eda/kueng-tensors.pdf>.
- [129] A. J. Daley, Quantum trajectories and open many-body quantum systems, *Adv. Phys.* **63**, 77 (2014).
- [130] J. Haegeman, J. I. Cirac, T. J. Osborne, I. Pižorn, H. Verschelde, and F. Verstraete, Time-Dependent Variational Principle for Quantum Lattices, *Phys. Rev. Lett.* **107**, 070601 (2011).